THE TYPE IA SUPERNOVA RATE IN INTERMEDIATE REDSHIFT GALAXY CLUSTERS

By

Eli Kunwiji Kasai

A dissertation submitted in partial fulfillment of the requirements for the MSc degree in the Department of Mathematics and Applied Mathematics, as part of the National Astrophysics and Space Science Programme

UNIVERSITY OF CAPE TOWN

APRIL 2013

Supervisors:

Dr Steve Crawford[1]

Professor Bruce A. Bassett[1,2,3]

[1] South African Astronomical Observatory (SAAO)
[2] University of Cape Town
[3] African Institute for Mathematical Sciences

Abstract

Studies of Type Ia supernovae (SNe Ia) in galaxy clusters can tell us about the metal enrichment of the intra-cluster medium, constrain the star formation history of cluster galaxies, aid us in the investigations of the progenitor systems of SNe Ia, act as tracers of the intra-cluster stellar population and can be used in measuring distances over extragalactic scales, which is relevant to supernova cosmology. However, the value of the cluster Type Ia supernova (SN Ia) rate at intermediate redshifts has not been well constrained and this hampers our ability to derive accurately the parameters needed in addressing the topics listed above. We have performed a search for supernovae and other transients in six galaxy clusters, located in the redshift range $0.3 < z < 0.9$ to derive the cluster Type Ia supernova (SN Ia) rate. The cluster images were taken with the WIYN 3.5 m telescope located on Kitt Peak in Arizona, over a time period of more than years (October 1999 - April 2005). We analyzed the R-band images of the clusters to search for transients and found two supernova (SN) candidates in the clusters MS0451-03 and CL0303+17, which are located at redshifts $z = 0.54$ and $z = 0.42$ respectively. We used the two SN candidates to derive the SN Ia rate for each cluster. Notwithstanding a zero detection of SN candidates in the rest of the clusters, we have also quantified the relevant factors that go into the calculation of SN Ia rates for these clusters and derived statistical confidence limits for all cases. We derive cluster SN Ia rates of $0.39^{+0.91}_{-0.39}$ SNuB for MS0451-03 and $0.21^{+0.48}_{-0.19}$ SNuB for CL0303+17, which are in good agreement with the rates derived by Sharon et al. (2010) and Graham et al. (2008) of $0.35^{+0.17}_{-0.12}$ at a mean redshift of $z = 0.6$ and $0.31^{+0.51}_{-0.16}$ SNuB at a mean redshift of $z = 0.45$ respectively. We have placed upper limits on the number of SN candidates expected from each of the four clusters that we did not detect SN candidates in. Here, the unit SNuB means "SNe per 100 years per 10^{10} $L_{\odot,B}$".

Plagiarism Declaration

I, Eli Kasai, know the meaning of plagiarism and declare that all of the work in this document, save for that which is properly acknowledged, is my own.

.

Eli Kunwiji Kasai

April 2013

Signed : .....

Acknowledgements

First of all, I give thanks to God, who I believe stood by me and kept me going during the tenure of carrying out this research.

I then thank my supervisor Dr Steven M. Crawford for his guidance, advise, direction and assistance from the beginning to the end of my thesis. His supervision has been remarkable and outstanding and I could not have seen this thesis through without his intervention and continuous support for the past year and a half.

I extend gratitude to Professor Bruce A. Bassett for a job well done in his capacity as my co-supervisor. Among other things, he knew how to keep me on track and motivated by constantly talking about how challenging research can be at masters level and higher and how one can get around the challenges to win. His involvement in this thesis contributed greatly to its successful completion.

I gratefully acknowledge assistance and fruitful discussions with a couple of fellow students and friends, the likes of Rajin Rampul, Vinesh Rajpaul, Michelle Knights and Alan Clarke.

A big thank you goes to SKA South Africa for making this endeavour possible for me by funding my MSc programme. I am grateful for the financial support. Also, I extend gratitude to the National Research Fund (NRF) and the National Astrophysics & Space Science Programme (NASSP) management committee for the funding I received at honours level and for my acceptance into the NASSP.

Lastly, I thank the South African Astronomical Observatory for providing work space and computer facilities and services for the duration of my research. I am deeply honoured to have had these opportunities.

Contents

List of Figures

List of Tables

Chapter 1

Introduction

1.1 Overview

In this thesis, we report the rate of SNe Ia events in six galaxy clusters located in the redshift range $0.3 < z < 0.9$. The rate in this redshift range is currently poorly constrained due to low number statistics, directly owing to the lack of sufficient observational data. The data set used for this thesis comprise an average of fifteen to sixteen images per cluster. Each cluster image has a field of view of 9.6' by 9.6'. The images were taken with the WIYN[1] 3.5 m telescope, located on Kitt Peak in Arizona, over a time period of more than five years (October 1999 - April 2005), as part of the WIYN Long Term Variability (WLTV) survey (see Crawford et al. 2006). The main aim of this thesis is to search for transients in the cluster images by performing image subtraction and to locate variable sources in the residual (difference) images, determine the number of SN Ia events from the discovered transients and then calculate the cluster SN Ia rates. In so doing, we aim to contribute to an improved understanding of the currently poorly constrained cluster SN rates, which provide insight into the metal enrichment mechanisms of the intra-cluster medium and excess iron problem in clusters (Maoz & Gal-Yam 2004), progenitors systems of SNe Ia and geometrical studies of the universe in cosmology.

The thesis also discusses our observational methods and data reduction techniques, as well as our two transient detection algorithms: (i) The IRAF[2] Image Subtraction Algorithm and (ii) ISIS Automated Image Subtraction Algorithm (Alard & Lupton 1998; Alard 2000). The search for transients was performed in the R-band images for all clusters. We do not have follow-up spectroscopic data to utilize in the classification of the types of SN candidates we detected. Also, determining the types of SN candidates we found using photometric measurements are beyond the scope of this thesis. We therefore resorted to other means of typing the SN candidates that involves looking at similar

[1] The WIYN consortium consists of the University of Wisconsin-Madison (W), Indiana University (I), Yale University (Y), and the National Optical Astronomy Observatories (N).

[2] The acronym IRAF stands for Image Reduction and Analysis Facility (see Chapter 3 for a detailed description).

studies carried out at similar redshifts and adopt the ratio of SN Ia candidates to the total number SN events discovered in such a study. We then make use of such a ratio as a multiplicative factor to the number of SN candidates discovered for each cluster, to derive their individual counts of SN Ia candidates.

The thesis comprises five Chapters. In Chapter 1, we give an introduction of the thesis topic and an account of the literature review on the subject, including a description of the types of SNe and their subtypes. In Chapter 2, we describe the observational procedure, data reduction techniques and provide a review on the literature knowledge for our cluster sample. In Chapter 3, we discuss the transient detection methods, their advantages and disadvantages and the classification of some of the transients we found. We present the data analysis, our results and how they compare to the literature in Chapter 4 and provide a conclusion and our plans for future work in Chapter 5. We assume in this work a flat cosmology, with parameters $\Omega_\Lambda = 0.7$, $\Omega_m = 0.3$, $H_0 = 70$ km s^{-1} and the Vega-based system for magnitudes, unless stated otherwise.

1.2 Supernovae and their method of detection

Supernova (plural supernovae) is a term used to refer to an exploding star, which marks the end of the existence of a star. Before we speak about supernovae, we briefly discuss how stars are formed and evolve and then end up as supernovae (SNe). For a comprehensive treatment of stellar evolution for low and high mass stars, see Carroll & Ostlie (2006), hereafter CO06, Chapter 13.

1.2.1 Star formation and evolution

Stars that we see in the night sky and including our own sun are formed from clouds of gas and dust that mainly consist of hydrogen. From the time a star is born or formed, a fusion reaction gets started in its core to produce radiative energy that prevents the star from gravitational collapse under its own weight. Overtime, the star uses up all its fuel in generating radiative energy and undergoes gravitational collapse that leads to an explosion referred to as a supernova. Gravitational collapse however only occurs in massive stars (stars that are several times larger than the sun - see discussion in the next section), which give rise to what are known as core-collapse supernovae. For sun-like stars and stars smaller than the sun, the process is slightly different in that when fusion reaction ceases in the core, the star's outer material (the envelope) is lost via a series of intermediate processes (see CO06, Chapter 13 for the discussion) until all that remains is a compact object known as a white or brown dwarf. We do not discuss brown dwarfs further in this thesis. The process of how a white dwarf ends up as a supernova is discussed in section 1.3.

1.2.2 Supernovae

SNe are some of the brightest astrophysical objects in the Universe with brightnesses that often briefly outshines that of their host galaxies. Historically, supernova (SN) events were observed to occur randomly as bright stars that suddenly appeared in the sky as "guest stars" and faded away after a couple of days or weeks. Some of the first historical SN records are Supernova 1006 (SN 1006) observed in A.D. 1006 (CO06). Other records include SN 1054 recorded by the Chinese in A.D 1054 (which has left a signature that is observed today as the Crab supernova remnant), Tycho's supernova (SN 1572) recorded by Tycho Brahe in 1572 and Kepler's supernova (SN 1604) recorded in 1604 by Johannes Kepler (CO06).

1.2.3 Supernova detection

Modern ways of detecting SN events involve taking astronomical images of the same part of the sky repeatedly with an optical telescope over a period of time and then subtract the images. The way this is done is by selecting one image from the total image sample that is then subtracted from each individual image to produce difference images. If SNe are present in some of the images, they reveal themselves in the differenced images. The key steps involved in producing difference images are discussed in Chapter 3. The identified SN candidates from the difference images are sometimes followed up with larger telescopes to obtain their spectra (singular spectrum). A SN spectrum tells us whether or not a SN candidate found in the difference image is indeed a SN. The spectrum also tells us whether we have found a type I (SN I) or a type 2 (SN II) supernova and what type of SN I or SN II we have found (see the next section for a discussion of the SN subtypes).

The number of SNe discovered to date has increased by an order of magnitude compared to a decade ago, which has enabled further studies into the progenitor systems of these objects, especially SNe Ia whose progenitor physics is to this day not well understood (see sub-section 1.3.1 for a further discussion). The increased numbers have also improved the estimation of cosmological parameters in supernova cosmology by alleviating the burden of small number statistics.

1.3 Supernova types and properties

Supernovae come in different forms, depending on what the mass of the parent star was. The various forms are classified into two types distinguished from each other by the presence of hydrogen in their spectra. Type I supernovae (SNe I) have no hydrogen in their spectra whereas Type II supernovae (SNe II) have. The two types are further divided into subtypes: (i) SNe I comprise the subtypes Ia, Ib and Ic; whereas (ii) SNe

II have the subtypes IIL, IIP, IIn and IIb (Filippenko 1997, hereafter FP97; Chevalier & Soderberg 2010). Figure 1.1 shows a flow chart of the spectral features of SN subtypes, Figure 1.2 shows their light curves and Table 1.1 displays their relative brightnesses in the R-band, anticipated progenitors and the environments they are likely to be located.

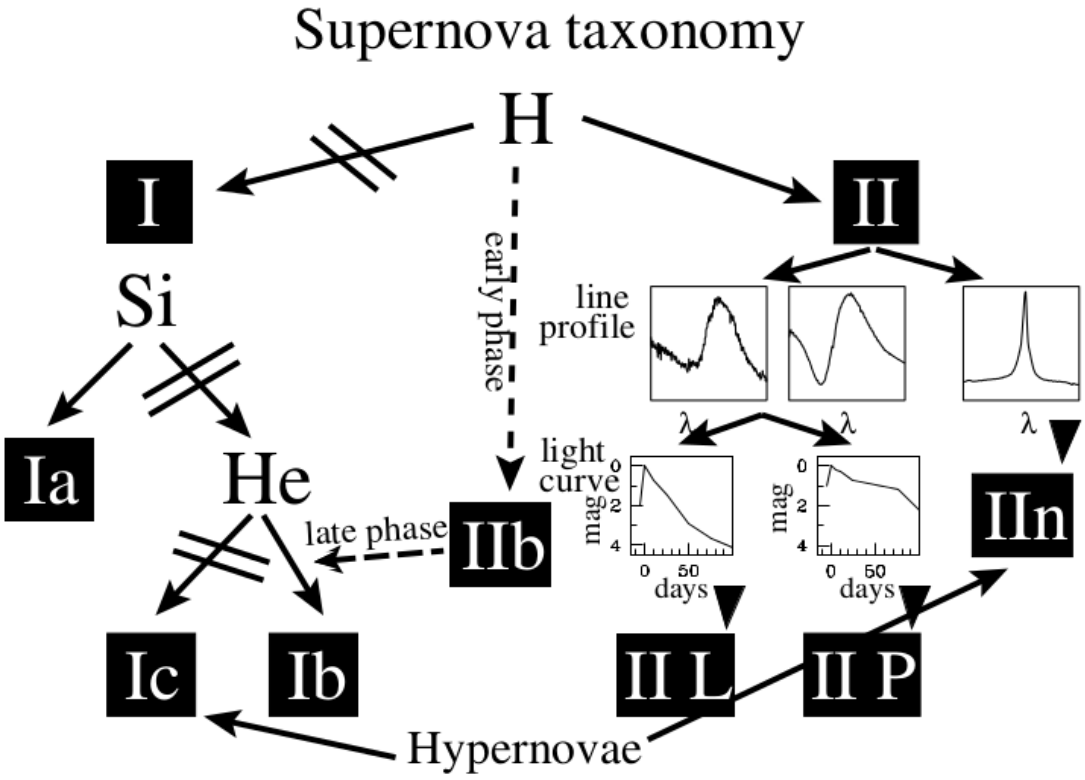

Figure 1.1: Classification of SN subtypes based on their observed spectral properties. The subtypes SN Ic and SN IIn belong to another category of SNe known as hypernovae. Figure from Cappellaro & Turatto (2001).

The properties provided in Table 1.1 are for SN subtypes considered normal. Peculiar SNe Ia such as 1991T and 1991bg are brighter (over-luminous) and dimmer (under-luminous) respectively, in comparison to normal SNe Ia, as Figure 1.3 shows. We do not discuss the peculiarity of CC SNe.

The subtypes SN Ib and SN Ic (SN Ib/c) have a physical relation to SNe II in that their progenitors are believed to be the same as those for SNe II, but with stripped hydrogen and helium envelopes (FP97). SNe Ib/c and the SNe II subtypes are collectively referred to as core-collapse supernovae (CC SNe). CC SNe are commonly found in late type-galaxies near spiral arms and HII regions and are very scarce in early-type galaxies (FP97; Barbary et al. 2012b, hereafter B12b). The progenitor systems of CC SNe are believed to be massive stars with masses of $> 8\ M_{\odot}$. In contrast, SNe Ia have been observed in all types of galaxies and do not seem to have preference for locations of their occurrence (Branch & Tammann 1992), although one of the recent studies indicate

Table 1.1: Relative brightness, anticipated progenitor and preferred environment of the various SN subtypes. By massive stars in this table, we mean stars with masses $> 8\ M_{\odot}$.

SN Type (Normal case)	Average peak absolute magnitude[a]	Anticipated progenitor[c]	Anticipated location[c]
Ia	-18.7	4-7 $M_{\odot}$ stars[b]	ellipticals and early-type spirals[a]
Ib	-17.0	short-lived massive stars, more massive than II progenitors	nearer bright H II regions
Ic	-16.0	highest mass stars, more massive than Ib progenitors	ongoing SF regions
IIP	-15.7	stars at the lower mass range of massive stars	recent SF regions
IIL	-17.4	stars more massive than IIP progenitors	recent SF regions
IIb	-16.7	stars more massive than IIL progenitors	closer to H II regions
IIn	-16.9	stars less massive than IIP progenitors[d]	Not common in ongoing or recent star forming regions

[a] - These are indicative averaged peak R-band magnitudes adapted from Li et al. (2011b).

[b] - Oemler & Tinsley 1979, Filippenko (1997).

[c] - Anderson et al. (2012)

[d] - This is quite the opposite of what is popularly known in the literature about the progenitors of SNe IIn being luminous blue variables (e.g. Groh et al. 2013), which are massive blue stars several time larger than the SN IIP anticipated progenitors (see e.g. Humphreys & Davidson 1994.)

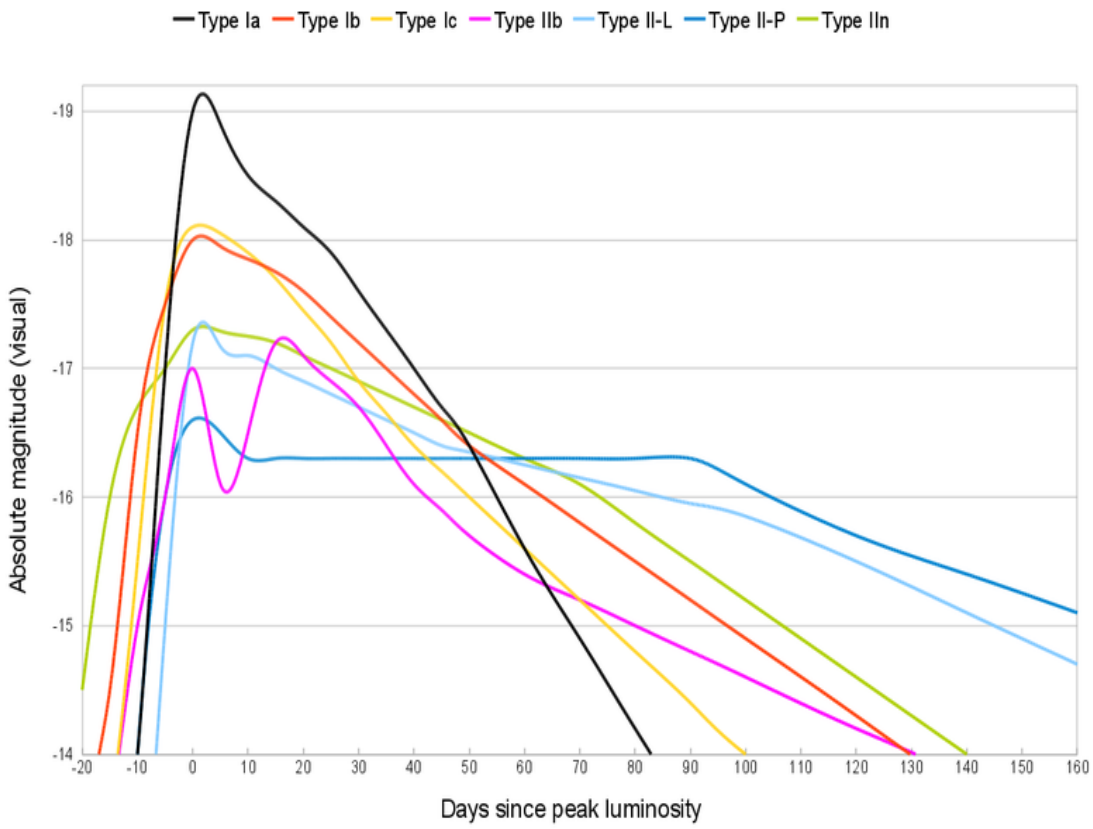

Figure 1.2: Light curves of the various SN subtypes taken from the International Virtual Observatory Association (IVOA) site "http://wiki.ivoa.net/twiki/bin/view/IVOA/CSPTimeSeries".

that these transients are more associated with ellipticals and early-type spirals (Li et al. 2011b). The progenitor stars for SNe Ia are believed to have a mass range of 4 - 7 $M_{\odot}$ (Oemler & Tinsley 1979, FP97).

In their volume limited SN sample drawn from the local universe out to 60 Mpc for CC SNe and 80 Mpc for SNe Ia, Li et al. (2011b) quantifies the distribution of SN subtypes into a pie chart show in Figure 1.4.

We provide below brief descriptions of the characteristics of the various SN types and subtypes.

1.3.1 SNe Ia

There is a consensus among the astrophysics community that SNe Ia result either from an accretion scenario (also known as the single-degenerate (SD) scenario) or a merger scenario. In the accretion scenario, the carbon-oxygen (CO) white dwarf (WD) is in a binary system with a companion, usually an evolved star, from which it accretes mass through the companion's expansion and Roche lobe overflow (Förster et al. 2006). The CO WD does this up to a point where its mass reaches a certain critical mass limit known as the Chandrasekhar limit, which has a value of about 1.40 $M_{\odot}$. On reaching this mass

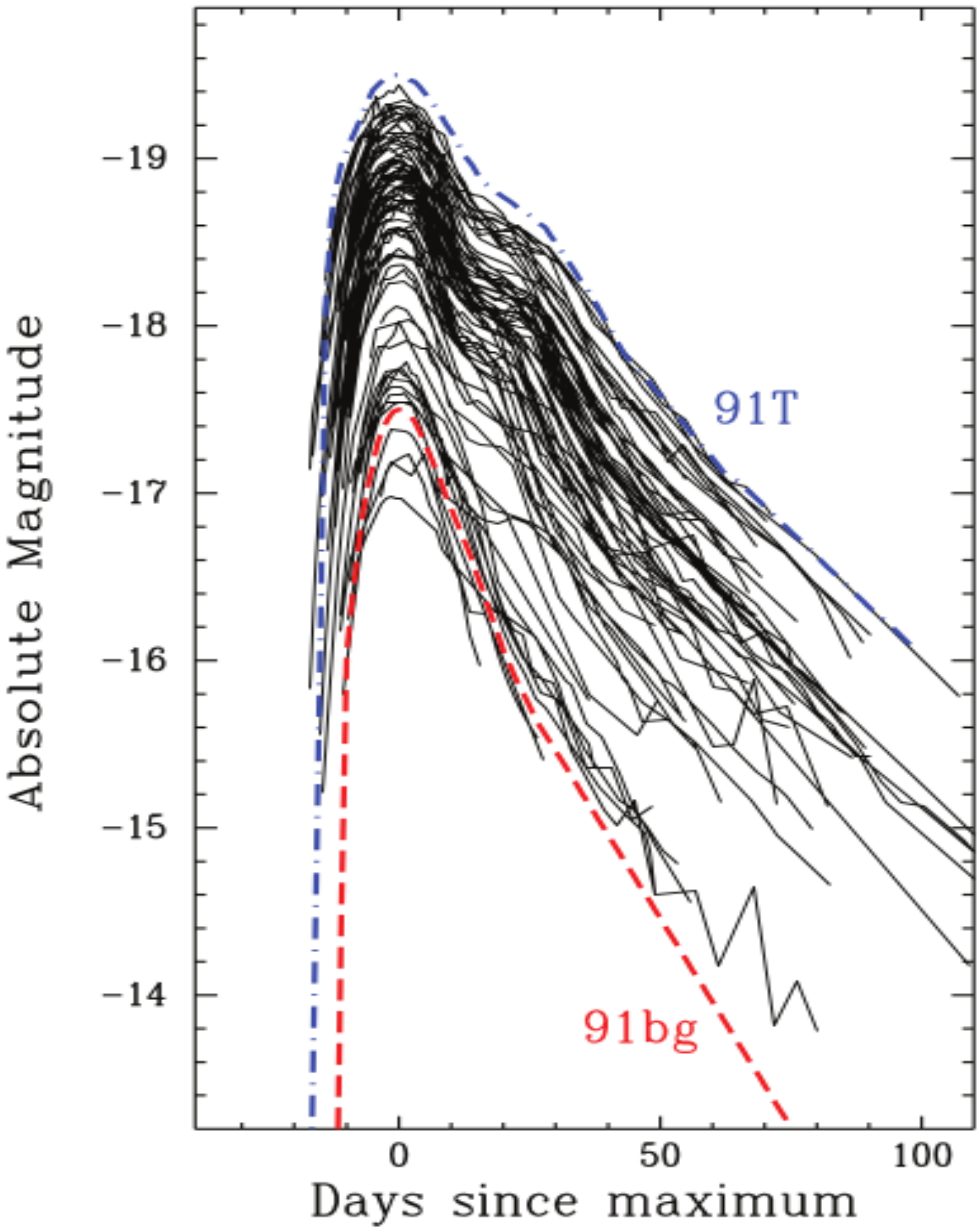

Figure 1.3: Observed R-band absolute magnitudes of SN Ia light curves considered by Li et al. (2011b). The blue dashed-dotted and red dashed lines represent the light curves for the Peculiar SNe Ia 91T and 91bg respectively. Figure from Li et al. (2011b).

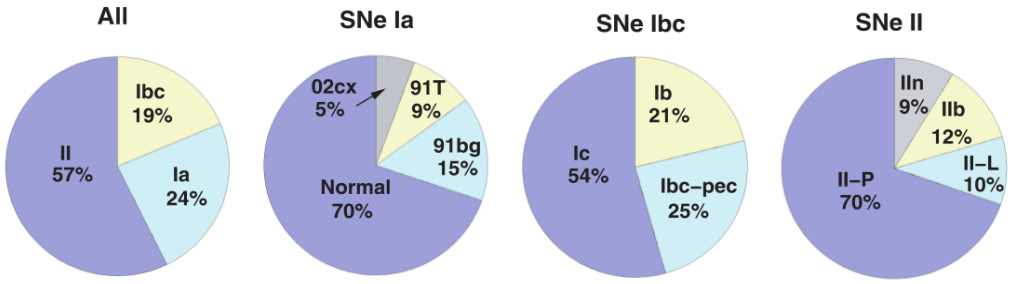

Figure 1.4: Distribution of SN types and subtypes from a volume limited sample in the local universe out to 60 Mpc for CC SNe and 80 Mpc for SNe Ia, compiled by Li et al. (2011b). The first pie chart details the percentage composition of SNe II, SNe Ibc and SNe Ia from their total sample of 180 SNe. In the second pie chart (from left), the subclass "02cx" refers to a class of peculiar SNe Ia that display characteristics similar to those of the peculiar SN Ia 2002cx (see Li et al. 2003b for the description of SN 2002cx). The subclass Ibc-pec in the third (from left) pie chart represent peculiar SNe Ibc, which includes the objects SN 2003id and SN 2002ap (see Li et al. 2011b and references therein).

limit, the CO WD initially supported by electron degeneracy pressure is no longer able to support itself via this mechanism against gravitational collapse and this leads to an ignition of its carbon component, which introduces a thermonuclear runaway reaction (Yungelson & Livio 2000). The ensuing reaction releases a vast amount of energy that disrupts the entire star in a SN Ia explosion.

The accretion scenario is also hypothesized to include the so-called sub-Chandrasekhar mass models (also referred to as double-detonation models) in which a CO WD has a low mass core compared to the previous case and surrounded by a mantle that comprises helium (Hillebrandt & Niemeyer 2000). The explosion mechanism in this case is caused by the compression of the CO core by the surrounding helium layer, leading to the ignition of carbon (Yungelson & Livio 2000) and the subsequent lower than Chandrasekhar mass SN Ia explosion.

In the merger scenario, two WDs in a binary system orbit each other and after a period of about 2×10^5 to 5×10^8 years, the angular momentum lost via gravitational radiation causes their orbit to shrink, leading to the formation of a massive disk around the largest of the two WDs which starts the accretion process all over again that eventually leads to a SN Ia explosion (Iben & Tutukov 1984). The merger scenario is also known as the double-degenerate (DD) scenario.

SNe Ia exhibit strong silicon lines near maximum brightness in their spectra as a deep trough at the wavelength λ6150 Å, attributed to the blueshift of Si II λ6355 (Filippenko 1988; da Silva 1993; Mazzali et al. 1993; FP97). They also display a remarkable homogeneity in such properties as absolute magnitudes and light curve shapes, with subtle variations in their general photometric and spectroscopic data (Branch & Tammann 1992; FP97; Hillebrandt & Niemeyer 2000). Figure 1.5 shows the spectra of three SNe Ia

at 5 days after maximum light, with spectral homogeneity among the three candidates clearly visible.

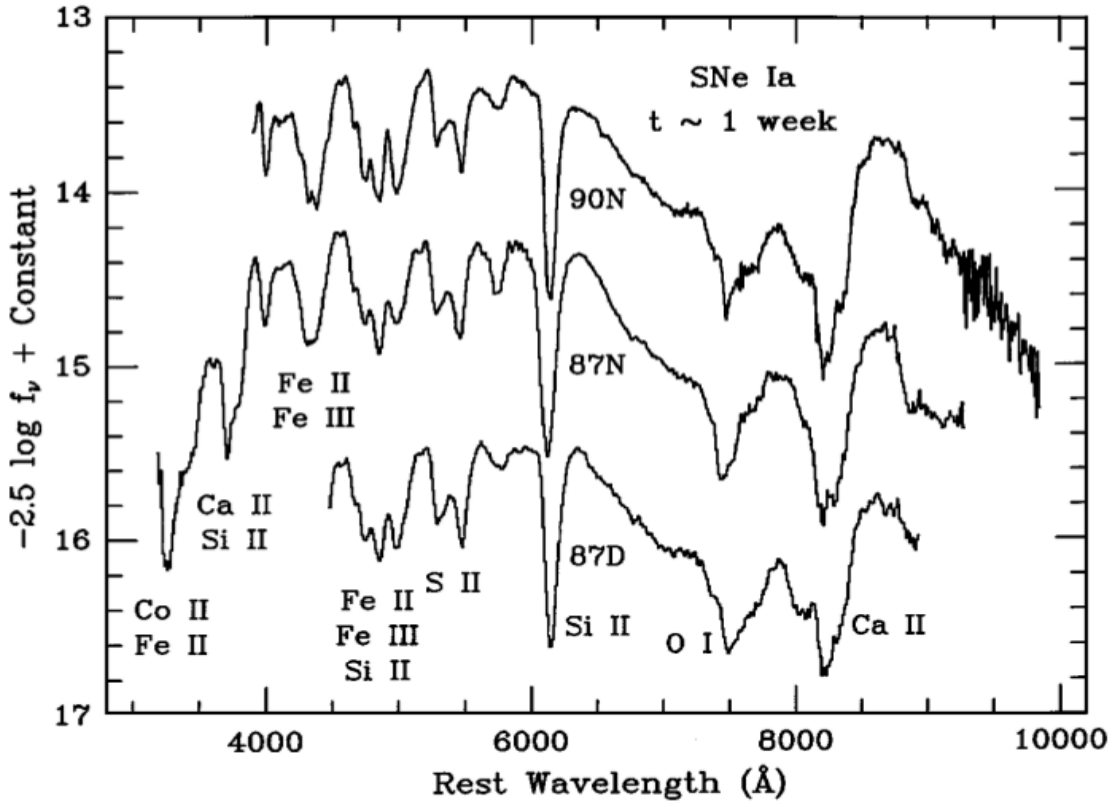

Figure 1.5: Spectra of 3 SNe Ia at about one week past maximum light. The host galaxies and their redshifts (kms^{-1}) are: 90N (NGC 4639; 970), 87N (NGC 7606; 2171), and 87D (MCG+00-32-01; 2227). Figure from FP97.

The late time spectra of SNe Ia are dominated by elements of iron and cobalt (Branch & Tammann 1992, FP97) as shown by the top most curve in Figure 1.8.

Despite the remarkable homogeneity displayed by SN Ia spectra shown in Figure 1.5, subtle differences among the spectra are noticeable on small scales. Also the light curves of various SNe Ia shown in Figure 1.2 varies over a range of peak magnitudes, with SN 1991T topping the range and SN 1991bg falling in the lowest range. As Table 1.1 indicates, SNe Ia considered normal have R-band magnitudes of around -18.7. Over-luminous SNe Ia have been found to show slow decay rates than the under-luminous ones (Phillips 1993).

The observed light curves of SNe Ia are powered by the decay of the radioactive isotopes ^{56}Ni (^{56}Nickel) and ^{56}Co (^{56}Cobalt), which are synthesized at the time of the explosion (Hillebrandt et al. 2013). The decay of ^{56}Ni into ^{56}Co ($^{56}\text{Ni} \rightarrow {}^{56}\text{Co}$) is responsible for the optical luminosity observed during the early phase (5-20 days after explosion) of the SN, whereas the decay process $^{56}\text{Co} \rightarrow {}^{56}\text{Fe}$ (^{56}Iron) powers the exponential decay

phase of the light curve, which occurs between 35 - 65 days after explosion (Colgate & McKee 1969). Each ^{56}Ni $\rightarrow$ ^{56}Co and ^{56}Co $\rightarrow$ ^{56}Fe decay process releases 1.72 MeV and 3.59 MeV of γ-photons, as Figure 1.4 shows.

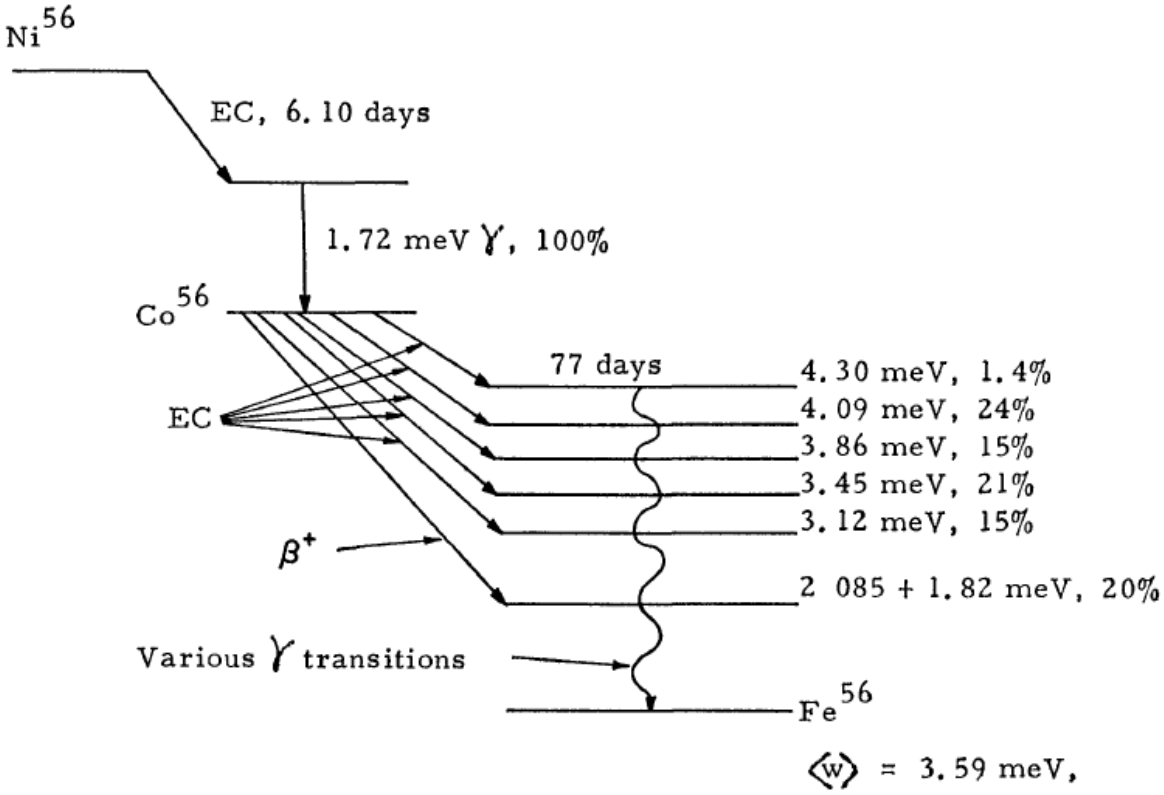

Figure 1.6: The radioactive decay process ^{56}Ni $\rightarrow$ ^{56}Co $\rightarrow$ ^{56}Fe, showing the various decay processes involved: Electron capture (EC), positron decay (β^+) and gamma decay (γ). Figure from Lederer et al. (1967).

1.3.2 CC SNe

The general theoretical understanding of the process leading to a CC SN event reported in the literature is that when nuclear fusion ceases in the parent star, its core becomes unstable and undergoes gravitational collapse. Following the start of the gravitational core-collapse, a series of intermediate processes occur before the actual SN II event takes place. The core, made mostly out of iron at this stage, gets compressed up to a level where nuclei degeneracy pressure does not allow any further compression (Janka et al. 2007). The outer core material and the stellar outer envelopes fall inwards and bounce off the hard nuclei degeneracy pressured iron core, generating a shock wave that reverses the direction of the in-falling material (Burrows et al. 2007). It is believed that such a shock wave loses energy and eventually stalls at a certain distance from the central core but receives a boost of energy via neutrinos that diffuse out of the compact dense core. The escape of neutrinos from the compressed iron core possess sufficient energy

that re-enegizes the stalled shock wave to disrupt the entire star in an explosion known as SN II, leaving a compact object at what was the centre of the star (Janka et al. 2007).

1.3.2.1 SNe Ib/c

The Si II feature observed in the spectra of SNe Ia is not seen in the SNe Ib and SNe Ic spectra (Filippenko 1988; Mazzali et al. 1993; FP97). As Figure 1.7 shows, SNe Ib are characterised by strong He I lines in their early-time spectra, which are not observed in the spectra of SN Ic taken at the same time. The late-time spectra of both subtypes are dominated by emission lines of intermediate mass elements, such as carbon, magnesium, oxygen and silicon (FP97), and at about 5 months after peak brightness, similar features are observed in both spectra (see Figure 1.8). Near maximum brightness, the spectra of SNe Ib resembles that of SNe Ia one to two months after maximum light (Filippenko 1988; FP97).

The progenitor stars for both subtypes are believed to be massive stars that have lost their hydrogen envelopes and also helium envelopes in the case of SNe Ic, during their evolution and prior to exploding (FP97).

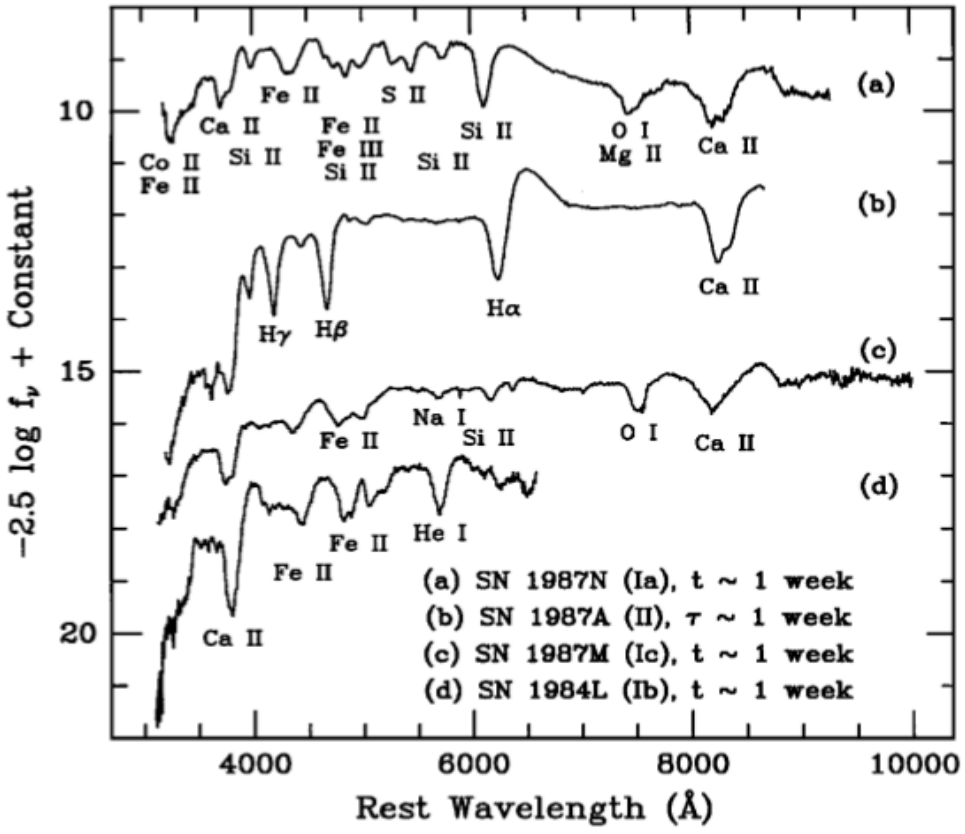

Figure 1.7: Early-time spectra of the three SN I subtypes and a SN II, at 1 week after peak brightness for the SN I subtypes and 1 week after core-collapse for the SN II subtype. Figure from FP97.

Smartt et al. (2009) suggest moderate mass interacting binaries to be the progenitors of SNe Ib/c and that the Wolf-Rayet progenitors may be responsible for the observed highly energetic broad-lined SNe Ic, also referred to as hypernovae.

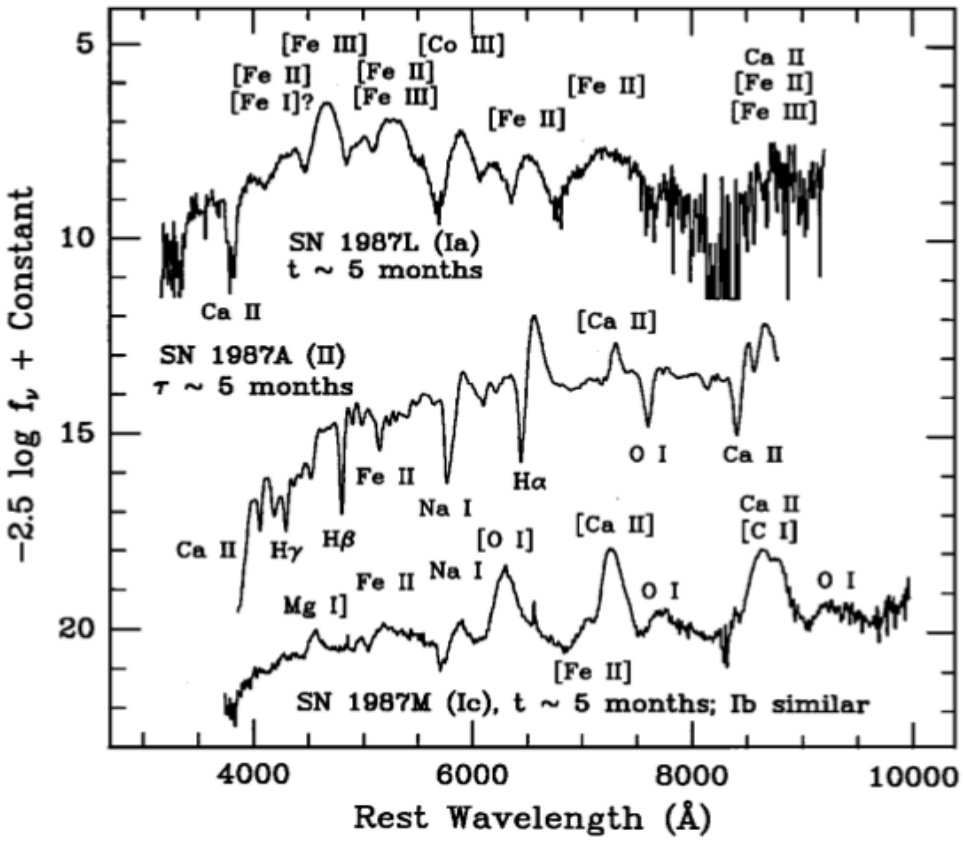

Figure 1.8: Same as Figure 1.7, at ∼5 months after peak brightness and core-collapse for SN I subtypes and SN II respectively, with the exception that the late-time SN Ia spectrum is for SN 1987L, not SN 1987N. Figure from FP97.

1.3.2.2 SNe II

The gradual spectral evolution of SN II subtypes resemble those of SNe Ib, demonstrating the physical link between the progenitors of the SNe Ib/c and those of SN II subtypes (FP97). The early-time (τ = 20 d in Figure 1.9) spectra for SNe IIP display almost no features and are dominated in the blue, signifying a colour temperature in the order of $\gtrsim$ 10,000 K (FP97). Also seen in these early-time spectra are weak hydrogen Balmer lines and He I λ5876. A few weeks after the estimated explosion date, the temperature of the expanding ejecta decreases to ∼5000 K and stays approximately constant at this value for anywhere between 10 to 80 days. It is during this time period that a plateau is observed in the light curve of SNe IIP (FP97; Maguire et al. 2012). The observed plateau phase in the light curve is a result of the hydrogen recombination wave front that moves through the large amounts of hydrogen ejecta and re-emits the energy injected by the

shock wave. The late-time (months after the explosion) spectra exhibit strong Hα lines and prominent emission lines of [O I], [Ca II] and Ca II (FP97).

SNe IIL on the other hand have light curves that decay linearly after maximum light

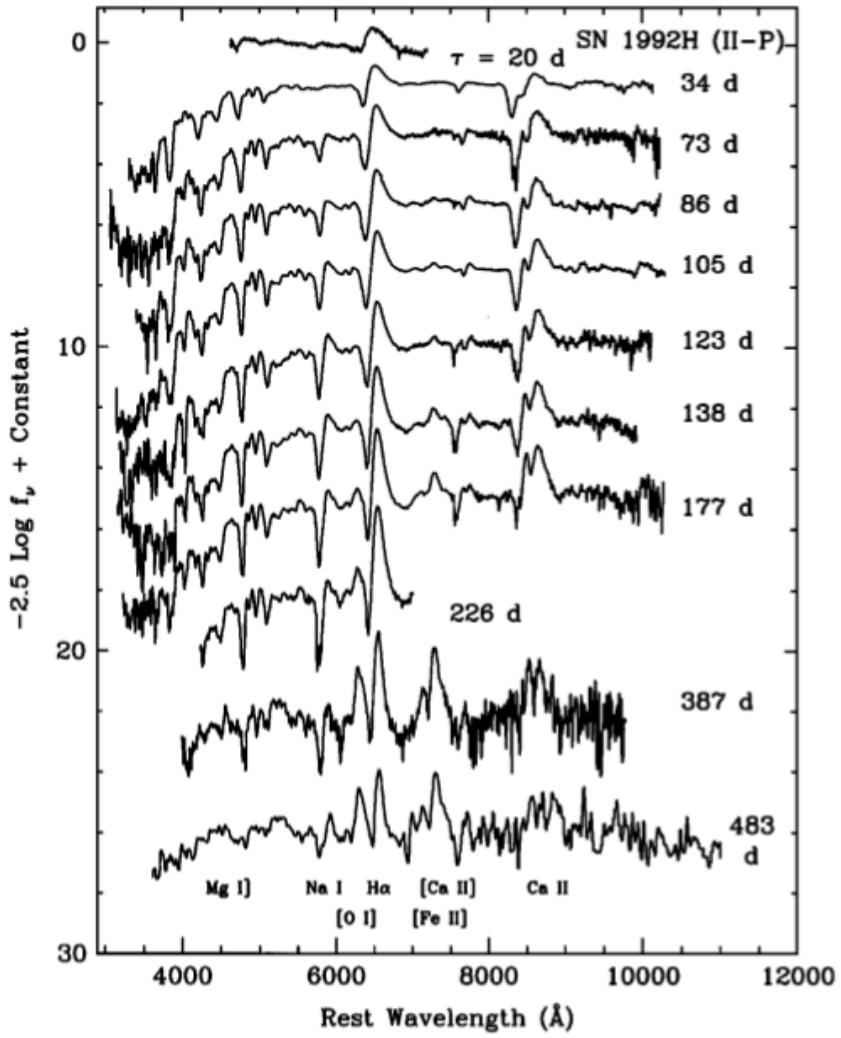

Figure 1.9: Early-time and late-time spectra of a SN II-P, SN 1992H in NGC 5377 at redshift cz = 1793 kms^{-1}, taken days (indicated by τ) after an estimated explosion date. Figure from FP97.

and in a similar fashion to the decay nature of SNe I. The absence of the plateau seen in the light curve SN II-P has been postulated to be due to the low mass hydrogen envelope that the SN II-L progenitor stars are believed to have, resulting in a limit in the hydrogen recombination processes responsible for the plateau effect seen in SNe II-P (FP97). The early-time spectra also appear blended and featureless and with dominance in the blue (see Figure 1.10). The late-time spectra, also displayed in Figure 1.10 at different times after explosion show a combination of low and high contrast P Cygni profiles of such elements as Na I, Hβ, Fe II and [O I]$\lambda\lambda$6300,6364.

A P Cygni profile is an emission line profile observed in T Tauri stars (pre-main

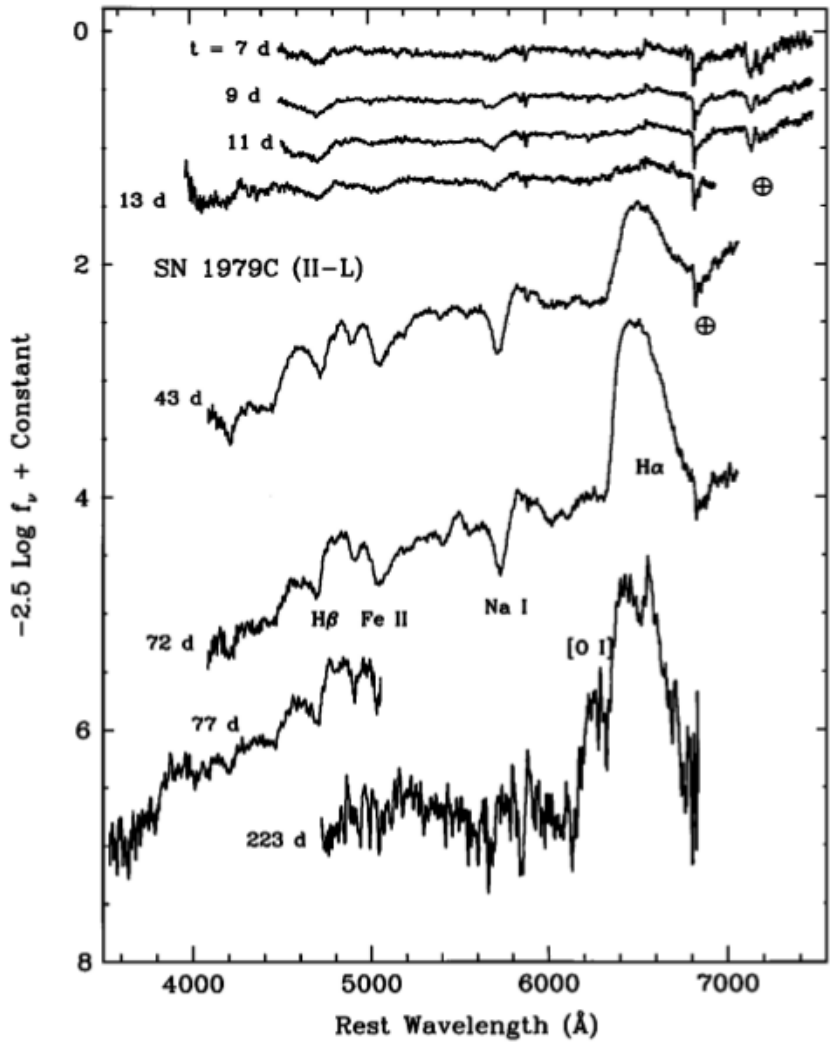

Figure 1.10: Early-time and late-time spectra of a SN II-L, SN 1979C in NGC 4321 at redshift cz = 1571 kms^{-1}, taken days (indicated by t) after an estimated explosion date. Figure from FP97.

sequence stars with a mass range 0.5 to 2.0 $M_{\odot}$ (CO06)), characterized by an absorption trough towards its blue end. The phenomenon signifies mass loss from a star. Figure 1.11, taken from CO06, Chap. 12, shows a sketch explaining a P cygni profile.

SNe IIn are characterised by a slow decay of their brightness and their spectra display weak or no broad P Cygni absorption lines (FP97, Pastorello et al. 2002). Their ejecta are believed to strongly interact with dense circumstellar matter blown off slowly by the progenitor stars with wind velocities of 50-1000 kms^{-1} and mass loss rates that exceed $10^{-4} M_{\odot}$ year^{-1} (FP97,Kiewe et al. 2012). Strong emission lines, especially Hα dominate the spectra of these objects, with narrow profiles, hence the "n" in the naming (Schlegel 1990, FP97, Smith et al. 2008). Early-time spectra of SNe IIn tend to be dominated in the blue, with a few of such spectra exhibiting He I emission lines for some candidates and narrow Balmer absorption lines with the corresponding absorption lines of Fe II, Ca

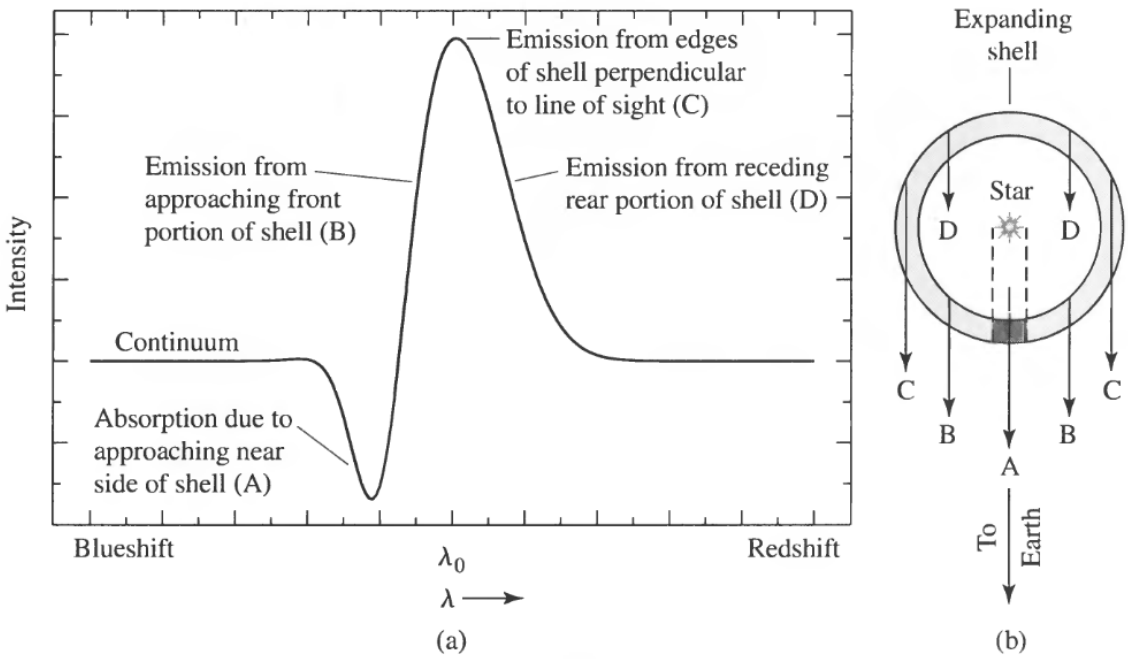

Figure 1.11: (a) Example of a P cygni profile showing a broad emission line peak and an absorption trough on the left side of the peak. (b) Demonstration of an expanding mass shell of a T Tauri star from which the P cygni profile originates. The positions of the letters indicate which part of the emission comes from what part on the expanding shell. The absorption trough is produced by an absorption of the light from the star by the intervening material in the part of the shell falling along our line of sight (shaded region). Figure from CO06.

II, O I or Na I in other candidates (FP97). Figure 1.12 shows spectra of five SN IIn candidates taken at the various indicated times τ after the explosion.

SNe IIb on the other hand are characterised by high-velocity hydrogen in their spectra near maximum light, but resemble more closely SNe Ib in their nebular (late-time) phase (Chevalier & Soderberg 2010). The best SN defining the properties of these types of objects is SN 1993J, discovered in the spiral galaxy M81 (Chevalier & Soderberg 2010).

Pastorello et al. (2008) studied the observational properties of SN 2008ax and found such properites as shape of the optical curve, bolometric luminosity and spectral line velocities to overlap those of SN 1993J, suggesting 2008ax to be a SN IIb. The progenitor stars of these peculiar objects are still not well understood (Pastorello et al. 2008; Kelly & Kirshner 2012). Figure 1.13 shows spectral evolution of SN 2008ax at various times (days) after core-collapse.

In the next sections, we discuss further SNe Ia, their frequency of occurrence in galaxy clusters and their applications in astronomy and cosmology.

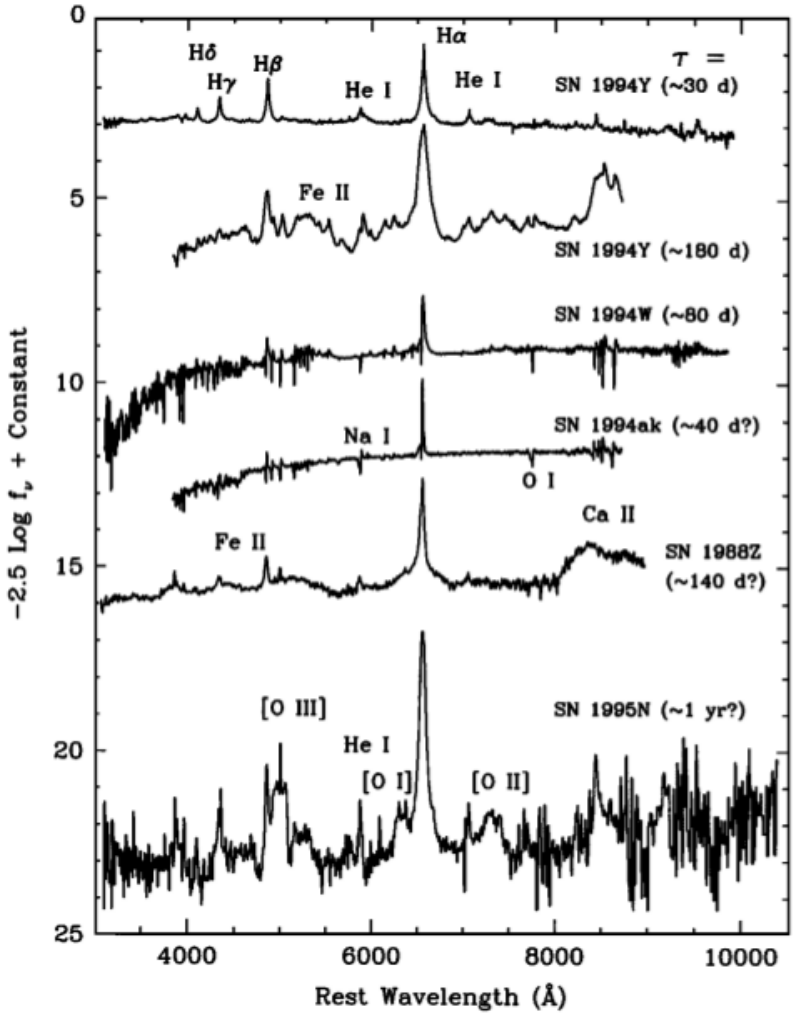

Figure 1.12: Spectra of five SN II-n candidates with host galaxies and redshifts (kms^{-1} as follows: SN 1994Y (NGC 5371; 2553), SN 1994W (NGC 4041; 1234), SN 1994ak (NGC 2782; 2562), SN 1988Z (MCG+03-28-022; 6595), and SN 1995N (MCG +02-38-017; 1534). Figure from FP97.

1.4 Importance of SNe Ia and their rate studies in clusters

SNe Ia rate measurements in galaxy clusters enable us to further our understanding of enrichment mechanism of the intra-cluster medium (ICM), which from X-ray observations have been found to contain a higher iron abundance than expected from SNe, based on current cluster SN rate measurements (Loewenstein 2006). Cluster SN (Ia) rate measurements also shed more light on the star formation histories of cluster galaxies, since such measurements play an important role in galaxy formation models as sources of feedback energy (Loewenstein 2006, Sharon et al. 2010). The progenitor systems of SNe Ia and their explosion paths are to this day not well understood and one way of addressing this challenge currently involves investigations of the delay time distribution (DTD) of SNe Ia, defined as the hypothetical time following a burst of star formation to when the first SN Ia events occur from such a burst (Maoz & Gal-Yam 2004; Maoz

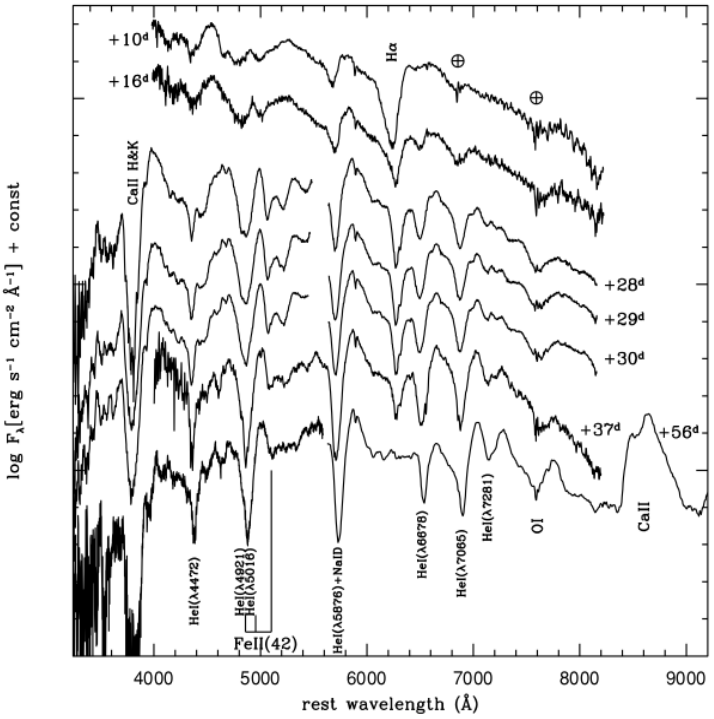

Figure 1.13: Spectral evolution of SN2008ax indicating spectral lines at various times (days) after core-collapse. A reddening correction of E(B - V) = 0.3 have been made to the spectra, placing them in the rest frame of the host galaxy. The crossed circles represent positions of important telluric lines. Figure from Pastorello et al. (2008).

et al. 2010, hereafter M10). Cluster SNe Ia also enable us to investigate the stellar population found in the ICM, which has been found to account for anywhere between 5% to 50% of the total stellar mass inside clusters (Feldmeier et al. 1998; Gal-Yam et al. 2003). SNe Ia detected both in clusters and the field have proven to be useful in constraining cosmological parameters (Kessler et al. 2009; Amanullah et al. 2010) and are thus powerful probes of the universe on the grandest scale. We discuss below each of these applications in more detail.

1.4.1 Cluster SNe Ia Iron yield

The observed mass of iron in the ICM for clusters at redshifts $0 \leq z \leq 1$ have been found to be several times larger than could have been produced by the total number of SN events observed to date in this redshift range (Maoz & Gal-Yam 2004). Based on the assumption that stars in clusters formed with a standard stellar initial mass function (IMF) (Salpeter 1955), the derived mean iron yield per single SN Ia and CC SN event is about 0.7 $M_{\odot}$ and 0.1 $M_{\odot}$ respectively (Maoz & Gal-Yam 2004; Mazzali et al. 2007b). Combining this with the integrated number of SNe Ia detected in clusters out to redshift z = 1.45 represent only about 10% of the fraction of iron mass estimated to be produced by SNe Ia in clusters (M10). This is the so-called iron problem in clusters alluded to above. It has been suggested by various authors in the literature that the implication

of the iron problem is an early production of the bulk of iron by SN events at higher redshifts.

In light of the above, a conclusion has be drawn stating that either (i) the IMF is to be skewed towards production of more CC SNe to account for the observed excess ICM iron abundance, or (ii) SN Ia events were more common at higher redshifts and occurred within short delay times (see a discussion of this in the next sub-section) to have produced the excess iron (Maoz & Gal-Yam 2004; Loewenstein 2006; Maoz & Mannucci 2012). SN Ia rate measurements beyond $z = 1$ show an increasing trend and thus suggests the latter, as Figure 1.14 shows. More cluster SN Ia rate measurements at higher redshifts are clearly needed to support this hypothesis.

1.4.2 DTD and star formation history of cluster galaxies

A number of authors have found in their studies that SN Ia rate measurements track the star formation history (SFH) out to higher redshift (Barris & Tonry 2006; Poznanski et al. 2007) and their overall conclusion is that the SN Ia DTD, defined in the introductory paragraph of this section, is concentrated at short delay times. Several attempts to measure the SN Ia delay times have been made by comparing observed SN Ia rates to the theoretical rates, constructed from the convolution of the SFH with the delay function. The delay is defined as the SN rate as a function of time after a brief burst of star formation (Foster et al. 2006, Loewenstein 2006). The results of such measurements have been inconsistent (Sullivan et al. 2006b). Moreover, uncertainties in the SFH predictions hampers the accuracy of the theoretical rates, potentially contributing to the observed discrepancies in the measured delay times (Sharon et al. 2007).

To address these inconsistencies, Sullivan et al. (2006b) advocated for the parametrization of the SN Ia delay times with not only a single model but a "two-component" model proposed by Mannucci et al. (2005) and Scannapieco & Bildsten (2005). The model isolates the "prompt" SN Ia component characterised by shorter delay times, from the "old" SN Ia component that comprises longer delay times and found mostly in elliptical galaxies in clusters. Since clusters contain mostly early-type galaxies, a bulk of the old stellar populations is found within their environments. Because cluster galaxies have relatively simple SFH, measurements of SN Ia rates in clusters can thus provide observational constraints on the shape of the "old" SN Ia component DTD (Sharon et al. 2007, M10). Processes leading to the occurrence of SNe Ia are linked to their delay times and for this reason, measuring the rate of SN Ia events in a given cluster at a particular epoch also provides a way of constraining the global SFH of galaxies in that cluster (e.g. Madau et al. 1998a).

It has been widely proposed and theoretically motivated in the literature (Sand et al.

2012 and references therein) that the SNe Ia late-time DTD, Ψ, can be parametrized by a power law of the form

$$\Psi(t) \propto t^s. \tag{1.1}$$

where t represents the time lapse after the instantaneous stellar formation epoch at a certain redshift and s the late-time DTD scaling exponent. The predictions of the DD and double-detonation models have been found to be described well by DTD scaling components of s = -1 and s = -2 respectively (Totani et al. 2008; M10; Ruiter 2011, Sand et al. 2012). Multi-wavelength photometric observations and optical spectroscopy have demonstrated that cluster galaxies formed their stars at redshift $z_f \sim 3$ (M10; Sand et al. 2012). Using this redshift to determine t, Sand et al. (2012) fitted a power law of the form given in (1.1) to the observed cluster SN Ia rates as a function of redshift shown in Figure 1.8 and derived a scaling component value of s = -1.62±0.54.

B12b performed a similar study recently, also assuming an instantaneous star formation epoch at $z_f \sim 3$ and derived a scaling exponent value of $-1.31^{+0.55}_{-0.40}$ (see B12b for further details). M10 tested the effect of fitting a power law to SN Ia data, characterised by a non-instantaneous star formation epoch with exponentially decaying SFH at $z_f = 5$, with several characteristics exponential times τ_{SF} = 0.5, 1, 2, 3 and 4 Gyr. The fit in each of these cases was worse than for the case of an instantaneous star formation discussed above. It therefore also appears from observations of SN Ia rates in clusters that cluster galaxies formed their stars in an instantaneous burst at redshift $z_f \sim 3$.

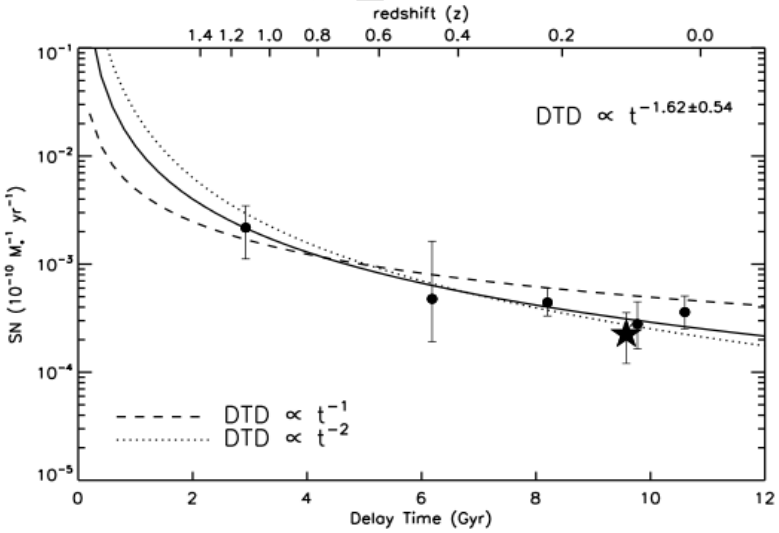

Figure 1.14: Observational constraints to the shape of the DTD Ψ obtained by fitting a power law of the form $\Psi \propto t^{-s}$ to the early-type/red sequence cluster SN Ia rate data vs delay time (Gyr). Instantaneous cluster star formation in a single burst at redshift $z \sim 3$ is assumed. The best fit curve is given by the solid curve with s = -1.65±0.54. The fitted dashed curve defined by s = -1 and dotted curve defined by s = -2 correspond to the expected power laws predicted by the DD and double-detonation SN Ia models respectively. Figure from Sand et al. (2012).

1.4.3 SNe Ia Progenitor Systems

The SN Ia late-time DTD discussed in the previous sub-section also provides one way of constraining the explosion channels of SNe Ia, which to this day remain poorly understood. As introduced in sub-section 1.3.1, the SD, DD and double-detonation scenarios are the three current actively studied explosion channels for SNe Ia. Studies by various authors suggest a late-time SNe Ia DTD that appears to be consistent with explosion paths predicted by the DD and double-detonation models, but not the SD models which predict a fast decline of the DTD at late delays (Mennekens et al. 2010; Ruiter et al. 2009; Sand et al. 2012). It has been concluded in the literature that if SD and DD models are considered to have similar realisation probabilities, then the DD channel is expected to be dominant in early type galaxies and that all channels are plausible in late-type galaxies, with SD channel contributing a larger fraction, due to its postulated high frequency at short delay times (Greggio 2005; Mannucci et al. 2008; Mennekens et al. 2010).

1.4.4 Intra-cluster stellar component tracer

Stars inside a cluster (referred to as intra-cluster (IC) stars), not belonging to any member galaxy in the cluster but bound by the cluster's gravitational potential, have been found to account for between 5% to 50% of the observed total cluster stellar mass (Fredmeier et al. 1998). Gal-Yam et al. (2003) pioneered the use of SNe Ia to trace such stars and using only two hostless SNe Ia discovered in Abell clusters at redshifts $0.06 < z < 0.19$, they determined the average mass composition of IC stars to be $20^{+20}_{-12}\%$ of the total cluster stellar mass. IC stars as can be expected are intrinsically faint and combining that with the cosmological dimming of surface brightness that scales as $(1+z)^4$ makes their detection impossible for clusters at intermediate and higher redshifts. Observations of SNe Ia have been able to overcome this difficulty as they are visible out to redshifts $z = 1$ and beyond, thereby opening a new window on studying the evolution of IC stars at various redshifts.

1.4.5 Cosmological distance measurements and parameter estimation

Knowledge of SNe Ia revolutionized our understanding of the universe more than a decade ago, by demonstrating that the universe has been accelerating in its expansion (Riess et al. 1998; Perlmutter et al. 1999). SNe Ia represents the most luminous and homogeneous of all SN subtypes described in section 1.3 and for this reason, they form one of the best methods for measuring galactic and extra-galactic distances (Brown et al. 2010; Kim 2011). Their apparent homogeneity is based on the knowledge that they all originate from a CO WD that explodes on reaching a critical mass limit of about 1.4 $M_{\odot}$, known as the Chandrasekhar mass (e.g. Branch & Tammann 1992, Phillips 1993). However, there exist slight differences in their measured peak absolute magnitudes, as shown in

the top panel of Figure 1.15, which are believed to be caused by such factors as different progenitor masses, rotation rates and accretion rates (Phillips 1993; March et al. 2011).

The rate of decline of brighter SNe Ia is slower than that of the dimmer ones (Phillips 1993). To be used as standard candles (objects with a known brightness) for measurements of cosmological distances, the observed scatter in their peak absolute magnitudes have to be corrected for. One way of doing this is using the "Phillips correction", which provides a correlation between the light curve decline rate of a SN Ia and its peak magnitude (Jha et al. 2007). The Phillips correction involves determining the quantity $\Delta m_{15}(B)$, known as the light curve decline rate parameter (Phillips et al. 1999), which measures the amount of decline in the light curve of a SN Ia measured in the blue-band at 15 days after maximum light. Using $\Delta m_{15}(B)$, the effects of host galaxy dust extinction to light from the SNe are estimated and corrected for (Phillips 1993, Phillips et al.1999), thereby producing a standardised SN Ia light curve. For this reason, SNe Ia are referred to as standardizable candles. Another correction applied to the absolute magnitudes measurements is the so called "K-correction", which describes how the measured brightness of objects in a given band varies with redshift. A further discussion of K-correction is provided in Chapter 4.

The top panel of Figure 1.15 illustrates a range of the SNe Ia light curves and the bottom panel shows the standardized light curve produced from the application of correction techniques to light curves in the top panel.

Determining distances in astronomy and cosmology using standard candles make use of the relation

$$m - M = 5log_{10}d_L + 25 \tag{1.2}$$

where m is the apparent magnitude of the object, M is the absolute magnitude (apparent magnitude of the object if observed at a distance of 10 parsecs from Earth) and d_L is the distance to the object in mega-parsecs, known as the object's luminosity distance. The quantity $m - M$ is known as the distance modulus, often represented by μ in supernova cosmology literature. Normal SNe Ia have been found to reach similar peak absolute magnitudes in a given band of the visible spectrum, with a scatter of $\sim$0.3 magnitudes for candidates that appear to be unaffected by host galaxy dust extinction in the visual and blue bands (Vaughan et al. 1995). The use of modern SN Ia distance measurements techniques such as the "spectral adaptive lightcurve templates (SALT)", which parametrize SN Ia light-curves using luminosity, light-curve decline rate and color parameters (see Guy et al. 2005, 2007 for an explanation of these parameters and how their use), reduce the scatter to about 0.12 magnitudes (Guy et al. 2007). Other SN Ia distance measurement techniques include the "Multicolor light curve shape - MCLS" (Riess et al. 1996). Both SALT and MCLS measure the quantity μ on the LHS of (1.2).

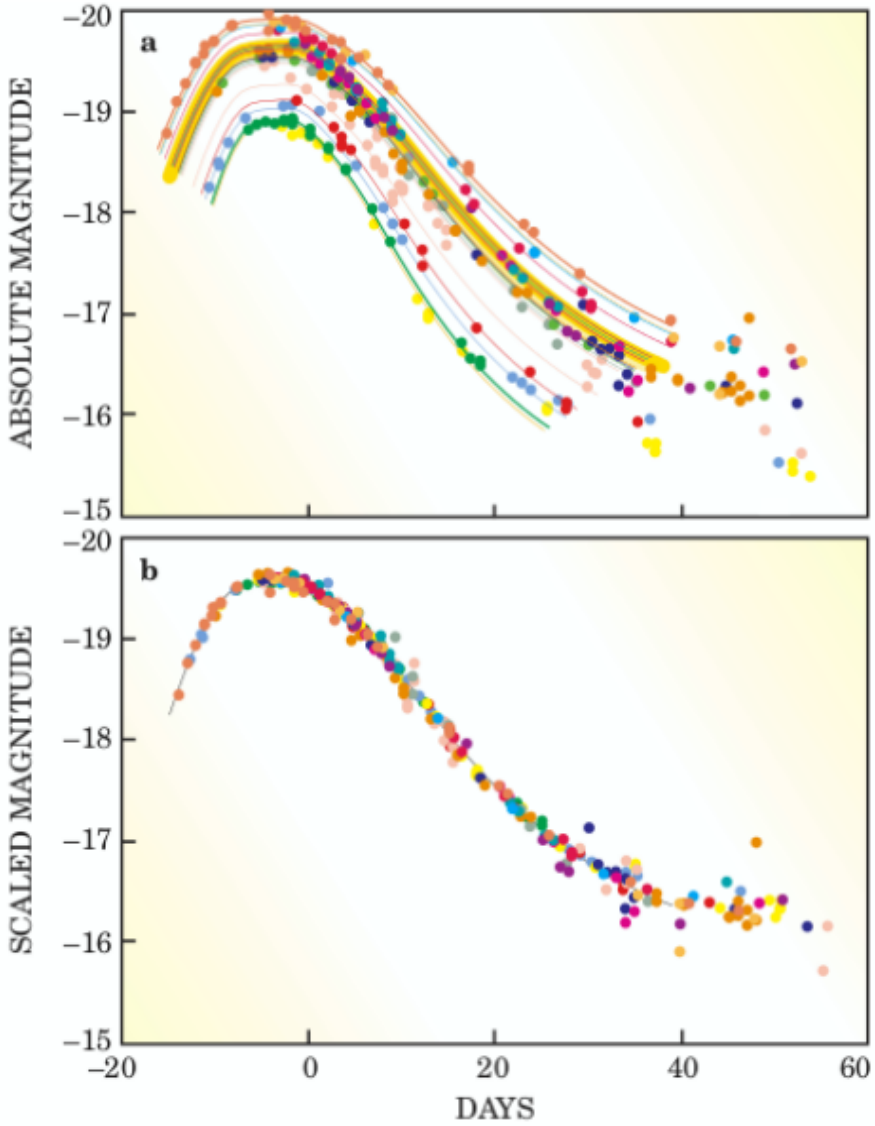

Figure 1.15: SN Ia light curves measured at low redshift by Mario Hamuy and collaborators (Hamuy et al. 1996). (a) Absolute magnitude vs time (days) before and after maximum light. The intrinsic peak brightness of outliers from the norm (yellow band), where most of the light curves are found to reside, can be deduced from their time scales. The brighter SNe reach peak luminosity and decline slower than their fainter counter parts. (b) After application of correction techniques to the light curves, which involves stretching the time scales of the respective light curves and scaling their brightnesses to match the standard light curve, all light curves are matched to produce a "standardized" light curve. Figure from Perlmutter (2003).

Goobar & Perlmutter (1995) pioneered a method that can constrain the cosmological parameters Ω_m and Ω_Λ, which makes use of (1.2) and the expression for luminosity distance for an object at redshift z

$$d_L = R_0(1+z)S(\chi(z)), \tag{1.3}$$

where

$$\chi(z) = \frac{c}{R_0 H_0}\int_0^z \frac{dz'}{\sqrt{\Omega_m(1+z')^3 + \Omega_k(1+z')^2 + \Omega_{DE}f(z)}} \tag{1.4}$$

and

$$S(\chi(z)) = \begin{cases} \sin\chi(z) & \text{if } \Omega_k < 0, \\ \chi(z) & \text{if } \Omega_k = 0, \\ \sinh\chi(z) & \text{if } \Omega_k > 0. \end{cases} \tag{1.5}$$

The quantity R_0 represents the present value of the scale factor of the universe $R(t)$ and has the value c/H_0, where c and H_0 represent the speed of light and the Hubble constant respectively. The variable k in (1.5) denotes the spatial curvature of the universe and takes on the values 1, 0, and -1 corresponding to a universe with positive, flat and negative spatial curvature respectively (e.g. Hobson et al. 2006). The quantities Ω_m, Ω_{DE} and Ω_k are known as cosmological or density parameters and represent the three components that the total energy density of the universe is believed to be made out of. Ω_k defines the degree of curvature of the universe. In a flat ΛCDM universe, $\Omega_k = 0$ and Ω_{DE} becomes Ω_Λ, implying that $\Omega_m + \Omega_\Lambda = 1$. Here Ω_m and Ω_Λ represent the ratios of the total matter and vacuum energy densities respectively relative to the critical density needed to obtain $\Omega_k = 0$ (see Hobson et al. 2006, Chapter 15). H_0 as stated earlier is the Hubble constant; a constant relating the recession velocities of galaxies and their distance from us.

The denominator of the integrand in (1.4) is known as the dimensionless Hubble parameter and is defined in many texts as the function $E(z)$, so (1.4) is often written in the form

$$\chi(z) = \frac{c}{R_0 H_0}\int_0^z \frac{dz'}{E(z')}. \tag{1.6}$$

The function $f(z)$ in $E(z)$ is known as the dark energy density function and related to the equation of state parameter for dark energy $w(z)$ via the exponent

$$f(z) = \exp\left[3\int_0^z \frac{1+w(z')}{1+z'}dz'\right], \tag{1.7}$$

derived from the continuity equation $\dot{\rho} + (\rho + c^2/p)3\dot{R}/R = 0$ for a cosmological fluid with density ρ and pressure p.

The cosmological model of the universe that best fits our observational data is called ΛCDM (Komatsu et al. 2011) and operates under the Friedmann-Robertson-Walker (FRW) metric, which assumes that the universe is homogeneous and isotropic on largest (cosmological) scales. ΛCDM assumes, among other assumptions, that the universe is spatially flat and the equation of state parameter w for dark energy is a constant value of -1, irrespective of z. Under such a model, (1.7) becomes unity and as stated before, dark energy DE is given by the cosmological constant Λ, rendering (1.3) into the new form

$$d_L = (1+z)\frac{c}{H_0}\int_0^z \frac{dz'}{\sqrt{\Omega_m(1+z')^3 + 1 - \Omega_m}}, \tag{1.8}$$

To constrain the cosmological parameters Ω_m and Ω_Λ, measurements of μ from (1.2) for SNe Ia as well as their redshifts are made using methods that include the SALT and MCLS techniques described above. The measured μ_{obs} values are compared to the theoretically predicted values μ_{thr}, obtained by computing the values of d_L in (1.8) using the measured SN Ia redshifts and a chosen cosmology for Ω_m as inputs for z. The integral in (1.8) is performed for each redshift, with chosen values of Ω_m, Ω_Λ and H_0. The determined d_L values are then substituted on the RHS of (1.2) to obtain μ_{thr}. The best fit cosmology to the data is obtained through χ^2 minimization of μ_{thr} and μ_{obs}, yielding the best fit parameters for Ω_m and Ω_Λ.

Figure 1.16 shows the Hubble diagram for the Union2.1 compilation SNe Ia data set, which consists of 580 SNe Ia, and the best fit cosmology to the data (solid curve).

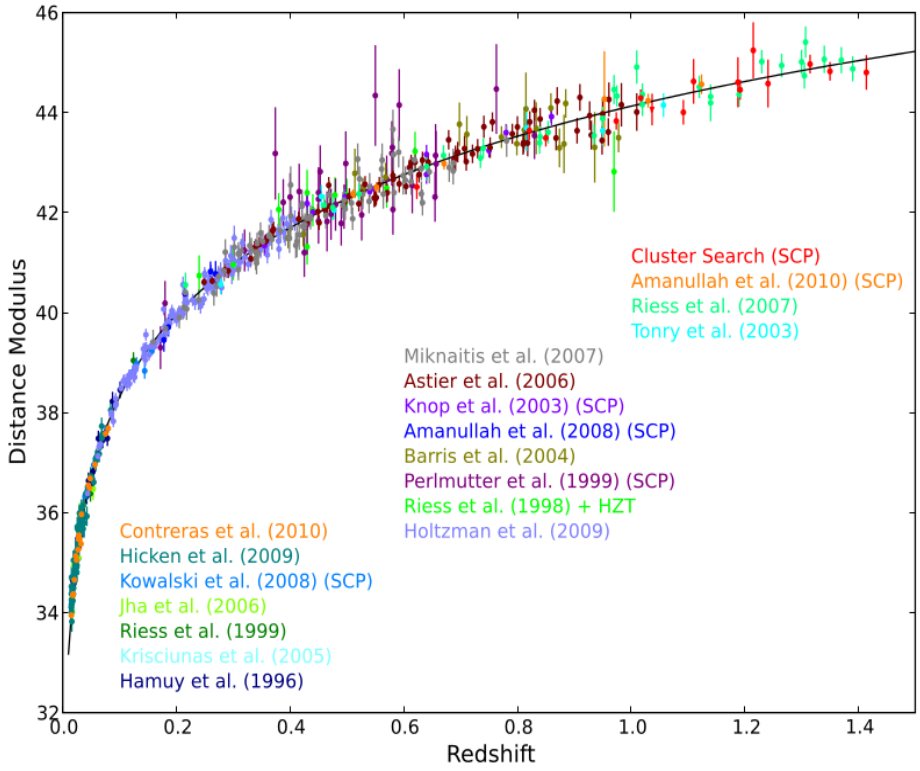

Figure 1.16: Hubble diagram for the Union2.1 compilation data comprising 580 SNe Ia from various sources distinguished by colour. The solid curve represent the best-fitted cosmology for a flat universe with $\Omega_m = 0.27$ and $w = -1$. Figure from Suzuki et al. (2012).

Suzuki et al. (2012) derived from the best-fit cosmology in Figure 1.16, values of $0.277^{+0.022}_{-0.021}$ and $0.705^{+0.040}_{-0.043}$ for Ω_m and Ω_Λ respectively, using the Union2.1 compilation SNe Ia data alone.

1.5 Previous Cluster SN Ia Rate Measurements

Galaxy clusters are made up of strong gravitational potential wells and are the largest gravitationally bound systems, making them ideal laboratories for studying enrichment mechanisms of the intra-cluster medium (ICM). The ICM has been observed to contain the majority of the baryons in clusters (Maoz & Gal-Yam 2004; Sand et al. 2008). The strong gravitational potential wells enable clusters to retain all elements produced within them, including iron and other heavy elements produced from SNe explosions (Sharon et al. 2010). Rich clusters contain at least 50 galaxies that are brighter than or have luminosities equivalent to that of the Milky Way within a 1 MPc radius (Sparke & Gallagher 2007, hereafter SG07) and have mass estimates of $M \gtrsim 3 \times 10^{14} M_\odot$ (Schneider 2006). Clusters can extend over more than 1 Mpc in diameter (Schneider 2006) and are mostly made up of early-type galaxies, which are old elliptical galaxies with minimal or no star formation. This means that the SN Ia events occuring in these systems are those associated with the older stellar populations or long delay times (Sullivan et al. 2006b;

Sand et al. 2008).

The first cluster SN measurements were made by Crane et al. (1977), where they used a sample of 8 SNe discovered in E/SO galaxies in the Coma cluster, within 3' of the cluster centre and derived a cluster SN rate of 6±2 SNU, where SNU (supernova units) in this case means SNe per 100 years per 10^{12} $L_{\odot}$. Four of the 8 SN candidates were SNe I and the other four were of an unknown type. Also in the same study, they derived using two SNe (of types SN I and peculiar) discovered in two spirals, a rate of 8±5 SNU.

In the following year, Barbon (1978) used a sample of 5 SNe I discovered also in the Coma cluster and derived a cluster SN I rate of between 0.07 and 0.10 SNe per 10^{10} $L_{\odot}$ per 100 years. The determined rate is reported as SN I rate, owing to the inability to distinguish between the characteristics of SN I subtypes at the time, as discussed above.

After this pioneering work by the two groups, subsequent cluster SNe Ia rate measurements have been conducted at various redshifts by a number of groups. To highlight some of the recent measurements in order of increasing redshift, Mannucci et al. (2008) re-analysed the Cappellaro et al. (1999) data, consisting of 136 SNe obtained in the local universe from observations of more than 8000 galaxies at redshifts $z < 0.04$ for many years. Out of the total sample, a sub-sample of 20 SNe Ia discovered in cluster galaxies in the range $0.005 < z < 0.04$, was used to derive a cluster SNe Ia rate of $0.057^{+0.021}_{-0.016}$ SNuM (SNuM = SNe per 100 years per 10^{10} $M_{\odot}$) at a mean redshift of $z = 0.020$.

Dilday et al. (2010) used a sample of 8 SNe Ia discovered in clusters from the SDSS C4 catalog - a catalogue containing clusters in the redshift range $0.03 < z < 0.17$ from the survey's main spectroscopic sample - to derive a cluster SN Ia rate of $0.060^{+0.029}_{-0.021}$ SNuM at a mean redshift $z = 0.084$. Sand et al. (2012) recently used a sample of 11 SNe Ia discovered in 57 X-ray selected galaxy clusters in the redshift range $0.05 < z < 0.15$ and derived an overall cluster SN Ia rate of $0.049^{+0.021}_{-0.018}$ SNuM at a mean redshift of $z = 0.10$. Sharon et al. (2007) used a sample of 6 cluster SNe Ia discovered by the Wise Observatory Optical Transient Survey in the redshift bin of $0.06 < z < 0.19$ to derive at a mean redshift $z = 0.15$ a cluster SN Ia rate of $0.098^{+0.068}_{-0.048}$ SNuM.

Dilday et al. (2010) in the same publication as above used another sample of 25 SNe Ia discovered in clusters from the SDSS MaxBCG catalogue - a catalogue containing clusters in the redshift range $0.10 < z < 0.30$ from the survey's photometric measurements - to derive a cluster SN Ia rate of $0.088^{+0.027}_{-0.020}$ SNuM at a mean redshift of $z = 0.225$. Using the three cluster SNe Ia discovered in clusters in the range $0.2 < z < 1.0$ by the Canadian-France-Hawaii Telescope Supernova Legacy Survey, Graham et al. (2008) derived a cluster SN Ia rate of $0.1^{+0.09}_{-0.04}$ SNuM at a mean redshift of $z = 0.46$. Recently, Sand et al. (2012) converted this rate to $0.177^{+0.212}_{-0.124}$ SNuM to take into account the "diet

Salpeter IMF", which is the commonly used IMF in cluster SN rates determinations and introduces a 30% reduction in the total mass considered under the usual Salpeter IMF (e.g. B12b, Sand et al. 2012).

Sharon et al. (2010) found 11 SNe Ia candidates in HST images of clusters in the range $0.50 < z < 0.90$, of which only 5 had spectroscopic confirmation and used the average between the spectroscopically confirmed and photometric candidates to derive a cluster SN Ia rate of $0.112^{+0.055}_{-0.039}$ SNuM. B12b rescaled the rate upwards to $0.151^{+0.138}_{-0.116}$ SNuM to take into account correction effects that were not made for evolution in the mass-to-light ratio determination in the SDSS g and r bands between the redshifts $z = 0.6$ and $z = 0$. Also and most recently, B12b used a sample of 8 ± 1 SNe Ia discovered in clusters in the range $0.9 < z < 1.46$, from the HST Cluster Supernova Survey to derive a cluster SN Ia rate of $0.36^{+0.23}_{-0.19}$ SNuM at a mean redshift of $z = 1.12$.

Figure 1.16 provides a plot of the recent SN Ia rates discussed above as a function redshift.

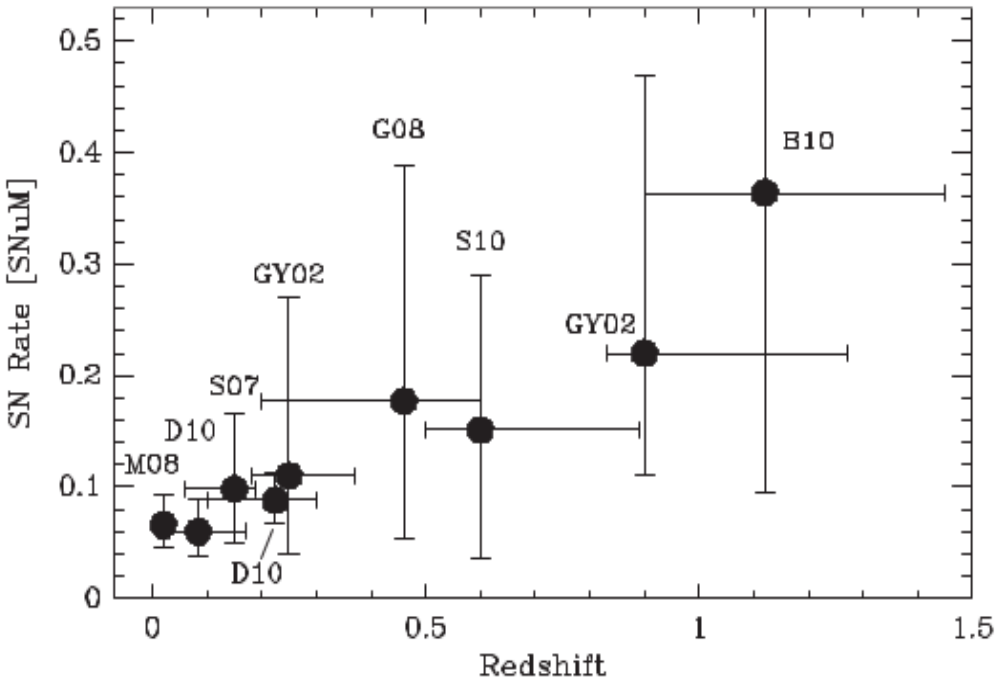

Figure 1.17: Cluster SN Ia rates per unit stellar mass (in units of SNuM $\equiv$ SNe per 100 yr per 10^{10} $M_\odot$) versus redshift. Horizontal error bars represent redshift intervals for each survey, with filled circles marking positions of the visibility-time-weighted mean redshift of each survey. Vertical error bars are the summed statistical and systematic 1σ confidence limits. The shown labels represent: M08-Mannucci et al. (2008); D10-Dilday et al. (2010); S07-Sharon et al. (2007); GY02-Gal-Yam et al. (2002); G08-Graham et al. (2008); S10-Sharon et al. (2010); B10-Barbary et al. (2010), which essentially is Barbary et al. (2012b). Figure from Maoz et al. (2010).

We do not review the CC SN rates in this thesis.

Chapter 2

Observations and Data Reduction

The observations and data reductions for the images used in this thesis were performed by Dr Steven M. Crawford and his collaborators (Crawford et al. 2006, 2009, 2011), at the University of Wisconsin. We provide a detailed description of these two aspects.

2.1 Observations

The observational data for all six clusters were acquired with the WIYN 3.5 m telescope (with image quality of 0.7 arcsecond median seeing) using the Mini-Mosaic Camera, which consists of two 2K $\times$ 4K SITe[1] CCDs. The Mini-Mosaic Camera has a pixel scale of 0".14 per pixel and a field of view of 9'.6 $\times$ 9'.6. We discuss the WLTV Survey and its goals in more detail, provide a short literature review on our cluster sample and a brief description of the R-band filter.

2.1.1 The WLTV Survey

Most of the details provided in this sub-section have been summarized from Crawford (2006) and Crawford et al. (2011). The WLTV was a photometric survey conducted between October 1999 and June 2005, using, as stated above, the WIYN 3.5 m telescope. The goals of the Survey were to acquire variable and proper-motion data for projects that included the search for supernovae and measurements of their rates in clusters and the field. Other planned projects for the survey are provided in Crawford (2006) and Crawford et al. (2011). The survey gathered data on 10 galaxy clusters in the redshift range $0.3 < z < 0.9$ in 5 band-passes; $UBRI$ and z. Each cluster was observed up to a depth of $\sim$25 mag in each of the $UBRI$ bands and 23-23.5 mag in the z band. On average, each cluster was observed $\sim$7 times over the duration of the survey. Also, nearly all clusters were observed more than once on a given observational date, as Figure 2.1 shows.

[1] SITe is short for Scientific Imaging Technologies, Inc. - a company that specialises in the manufacturing of CCD imaging components and modules.

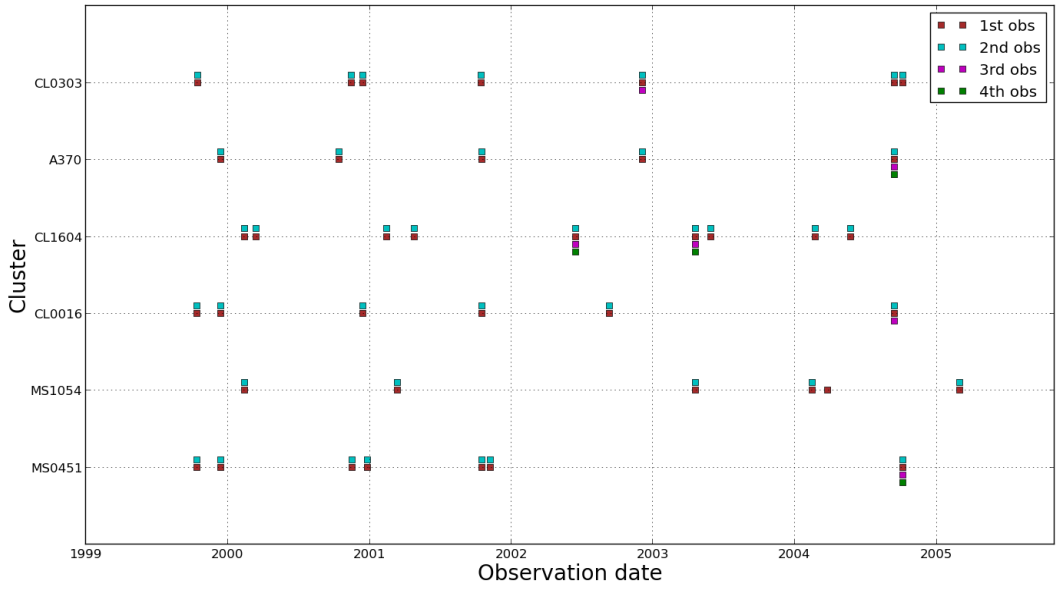

Figure 2.1: Cadence for our cluster sample. The brown squares represent the first observations of the clusters on a given observational date. Two observations in one night per cluster forms the bulk of the multi-observational runs (shown as 1st and 2nd obs in the legend). The magenta and green squares (3rd obs and 4th obs in the legend) represent the 3^{rd} and 4^{th} observational runs respectively, on a given night for the clusters indicated on the plot.

More observational details on the WLTV survey are accessible from the online "Direct Imaging Manual for Kitt Peak" hereafter as "MNL02", written by Massey et al. (2002).

2.1.2 Our Cluster Sample

As introduced in Chapter 1, we considered six galaxy clusters from the WLTV survey in this thesis. They fall in the redshift range $0.3 < z < 0.9$ and their selection from the survey's total sample of 10 galaxy clusters was purely random. We discuss some of the known properties of each cluster.

2.1.2.1 MS0451

MS0451-03 is located at redshift 0.54 at an RA and DEC of 04:54:10.8 and -03:00:56 respectively (Crawford et al. 2006). It is one of the most luminous X-ray galaxy clusters at intermediate redshifts and contains about 319 known galaxies (Moran et al. 2007). Figure 2.2 shows a colour image of the cluster.

The cluster has been found to be isothermal (constant in temperature) from spectral imaging data, with an isothermal temperature in the range (10.0-10.6) $\pm$ 1.6 keV at 90% confidence range, and its ICM iron (Fe) abundance is in the order of (0.32-0.40) $\pm$ 0.13 solar (Donahue et al. 2003). Donahue et al. (2003) also found MS0451-03 to be elongated and estimated, using their own and previous Sunyaev-Zeldovich data, the

Figure 2.2: True colour image of MS0451-03 centred around the brightest cluster galaxy (BCG) seen just above the foreground blue galaxy. The image was produced from V, R and I CCD frames of observations conducted between May 1992 and January 1994, with the Tektronix 2048 × 2048 pixel CCD (for the R band) and HRCam (for the V and I bands) mounted on the University of Hawaii 2.2 m telescope. Figure from Luppino et al. (1999).

cluster's angular diameter distance to be $D_A = 1219\pm^{340}_{288} \pm 387$ Mpc. The angular diameter distance is another measure of distances to astronomical objects. It is inferred from an object's angular size θ on the sky and its transverse line of sight proper diameter D. It is represented mathematically as $D_A = D/\theta$ (see Hobson et al. 2006, Chapter 14 and Schutz 2009, Chapter 12 for further explanations). Donahue et al. (2003) also estimated using the Chandra X-ray data the total mass of MS0451 to be in the range of (8.6-8.9)$\pm$1.2 $\times$ $10^{14}h^{-1}M_{\odot}$ at a cluster centric radius of $\sim$ 0.97 h^{-1} Mpc. The unit of measure h represent the current value of the Hubble constant H_0 divided by 100, i.e. $h = H_0/100$.

2.1.2.2 MS1054-03

MS1054-03 (MS1054) is located at redshift $z = 0.83$, at an RA and DEC of 10:56:59.5 and -03:37:28.39 respectively (Crawford et al. 2009). It is also one of the known brightest

X-ray galaxy clusters and is the Extended Medium Sensitivity Survey's (a large sky coverage survey with moderate depth and sensitivity and probes the bright end of the X-ray luminosity function of clusters) most distant cluster with an X-ray luminosity of $L_X = 2.2 \times 10^{45}\ h_{50}^{-1}$ ergs s^{-1} in the temperature range 2-10 keV (Donahue 1996; Lewis et al. 2002; Goto et al. 2005). van Dokkum et al. (1999) found a high fraction of merging galaxies in the cluster and used this discovery as evidence for the hierarchical structure formation model that requires the observed luminous local cluster ellipticals to have formed out of episodes of merger activities. Figure 2.3 shows a colour composite image of MS1054-03 mosaic field, courtesy of the Hubble Space Telescope (HST). Jee et al. (2005) estimated the cluster's mass within a 1 Mpc radius to be $(9.6 \pm 0.8) \times 10^{14}\ M_{\odot}$

Figure 2.3: Colour composite image for MS1054-03 made from the HST filters F606W, F775W and F850LP of the Advanced Camera for Surveys and Wide Field Camera, covering an area of 5' of the cluster mosaic field. Figure from Blakeslee et al. (2006).

The cluster is irregular and elongated and has a velocity dispersion of $\approx$ 1170 km s^1 (van Dokkum et al. 1999). Velocity dispersion refers to the root mean squared deviations of the random motion velocities of individual galaxies in a cluster from their

average velocity. Mathematically, this is represented as $\sigma = \sqrt{\langle \mathbf{v}^2 - \langle \mathbf{v} \rangle^2 \rangle}$, where $\mathbf{v}$ is the velocity vector for the random motions of individual galaxies and $\langle \mathbf{v} \rangle$ is the average velocity of the random motions. For a formal definition and mathematical derivation of σ, see Schneider (2006), Chapter 2. The cluster is found to contain 89 member galaxies (van Dokkum et al. 2000).

2.1.2.3 CL0016+16

CL0016+16 is located at redshift $z = 0.55$, at an RA and DEC of 00:18:33.6 and +16:26:16.01 respectively (Crawford et al. 2011). The cluster is rich, elongated and contains over 200 spectroscopically confirmed galaxies (Crawford et al. 2011). Geach et al. (2011) estimated the core mass of the cluster to be more than 10^{15} $M_{\odot}$. Due to a scarcity of mass estimations on this cluster in the literature, we are unsure of the extent of the core that Geach et al. (2011) based their mass estimation on.

The cluster appears to belong to what has been observed to be a supercluster structure within the redshift range $0.530 < z < 0.558$, which contains two other X-ray clusters RX J0018.3+1618 and RX J0018.8+1602 and both smaller in size (Connolly et al. 1996; Worrall & Birkinshaw 2003). Figure 2.4 shows a gray scale plot of three fields of CL0016+16.

2.1.2.4 CL1604+4304

CL1604+4304 is located at redshift $z = 0.90$, at an RA and DEC of 16:04:18.27 and +43:04:38.42 respectively (Crawford et al. 2009). The cluster consists of over 40 galaxies, has a mass estimate of more than 8×10^{14} h_{65}^{-1} $M_{\odot}$ within a cluster centric radius of 770 h_{65}^{-1}, a velocity dispersion of $\sigma = 982$ kms^{-1} and an X-ray luminosity $L_x = 2.0 \times 10^{44}$ ergs s^{-1} (Postman et al. 2001; Crawford et al. 2009). Figure 2.5 shows a composite i-band image of the supercluster that hosts CL1604+4304.

Postman et al. (2001) reported that CL1604+4304 contains significant populations of elliptical-like galaxies and blue galaxies and has a 45% fraction of active galaxies within the central 1.0 h_{65}^{-1} Mpc. An active galaxy in this case is defined as having a rest equivalent width [O II] greater than 15 Å. The names CL1604+4304 and CL1604 are used interchangeably to refer to the same cluster.

2.1.2.5 Abell 370

Abell 370 (A370) is located at redshift $z = 0.37$, at an RA and DEC of 02:39:53.1 and -01:34:35.0 (Hu et al. 2002). The cluster is known to host two bright cD (central Dominant) galaxies which together with their dark matter content gives it a very high density profile that results in strong lensing of background objects (Abdelsalam 1998; Richard et al. 2010). A370 boasts an X-ray luminosity of 2.37 $h^2 \times 10^{44}$ ergs s^{-1} (Smail et al. 1997). Figure 2.6 shows an image of A370, taken with HST in July 2009.

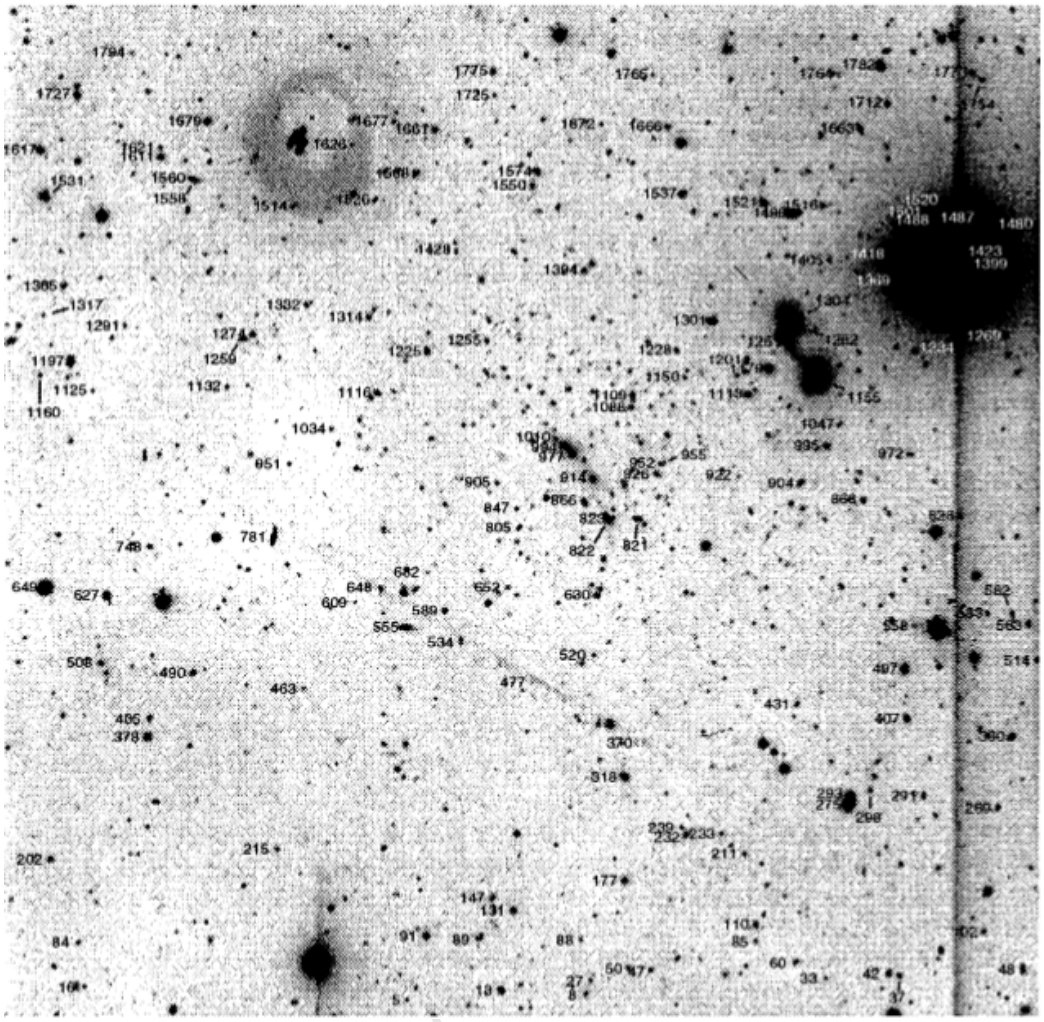

Figure 2.4: Gray-scale plot of three fields of CL0016+16. Object numbers have been tagged to galaxies with R-band magnitudes of less than 21 and fainter galaxies with redshifts. Figure from Ellingson et al. (1998).

The cluster has been confirmed to have a bimodal mass distribution, suggesting that in its current form, it may be a result of a merger between two equally massive clusters (Richard et al. 2010). Using strong lensing techniques, AbdelSalam et al. (1998) estimated the mass of A370 to be in the range (4-6) $\times$ 10^{14} h^{-1} $M_{\odot}$ within a central 2' $\times$ 2' field. Using a distance scale D_s of 5.533 kpc/" (see chapter four for the description and derivation of D_s), this corresponds to a centre radius of $\sim$ 0.35 Mpc. The cluster has more than 324 member galaxies (Lah et al. 2009).

2.1.2.6 CL0303+17

CL0303+17 (CL0303) is located at redshift $z = 0.42$, at an RA and DEC of 03:03:20.6 and +17:07:16.0 respectively (Dressler & Gunn 1992). CL0303+17 is a less populous cluster, with about 200 member galaxies, a velocity dispersion of σ = 912 kms^{-1} (Dressler & Gunn 1992) and an X-ray luminosity of 1.05 h^{-2} $\times$ 10^{44} (Smail et al. 1997). Figure 2.7

Figure 2.5: A composite BVR image covering a central field of 3'.6 of the cluster CL1604+4304. The marked squares in the image represent confirmed galaxy members of the cluster. Figure from Postman et al. (1998).

shows a CCD colour image of the cluster.

CL0303+1706 is non-circular and appears to poses a second core in its higher resolution observational data, raising the possibility of a highly likely merger scenario in progress (Kaiser et al. 1998). We have no total mass estimate for this cluster and are therefore unable to make a good comparison to the rest of the clusters. Kaiser et al. (1998) provides only an estimate of the gas mass of $98.1 \pm 31.2 \times 10^{12} M_{\odot}$ within a central radius of 1 Mpc (aperture radius of 3'), derived using weak lensing methods.

Table 2.1 provides a summary of our cluster sample properties reviewed in this subsection. As the Table demonstrates, we could not find in the literature mass estimates for each cluster at the same radius from the cluster centre.

Figure 2.6: A370 as observed by HST on 16 July 2009. The two cD galaxies are located in the image centre and to the right from the centre next to the red (elongated) luminous arc. Image from http://en.wikipedia.org/wiki/Abell_370.

2.1.3 The R-band filter

Table 2.2 gives the observation dates for images taken with the R-band filter at different epochs for each cluster in our sample. The R-band filter or simply the R-filter is part of the "Harris UBRI set", with properties and wavelength coverages shown in Table 2.3 and Figure 2.8 respectively.

The R-filter collects light particles known as photons from an astronomical source. Any photon that has a wavelength falling in the range shown in Figure 2.8 for the R-filter gets captured by it. At the end of the imaging exposure, the photon counts are converted into astronomical images that are then analyzed further for a specific purpose. Further details on the R-band filter and its use in the WLTV Survey are provided in MNL02.

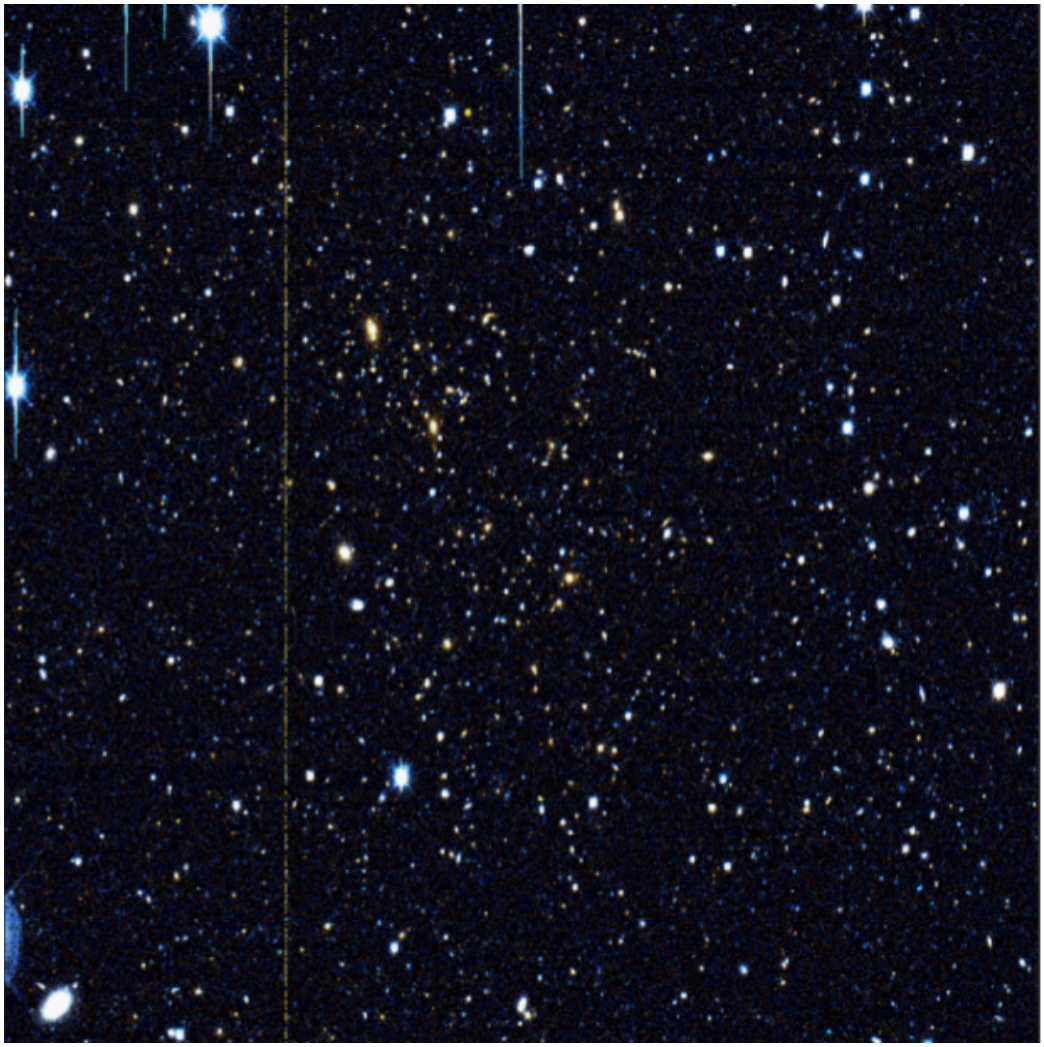

Figure 2.7: Colour image for the CL0303+1707 cluster field, centred around the cluster's BCG. Figure from "http://www-supernova.lbl.gov/public/figures/".

Table 2.1: Summary of the RA and DEC, redshift z, number of galaxies, velocity dispersion σ, mass estimate as well as X-ray luminosity L_x for our cluster sample.

Cluster	RA (J2000)	DEC (J2000)	z	Number of galaxies	σ (kms^{-1})	Mass estimate ($\times 10^{14}$ $M_\odot$)	L_x (erg s^{-1} $\times 10^{44}$)
MS0451	04:54.10.8	-03:00:56.86	0.54	319	1354	(8.6-8.9)$\pm$1.2 h^{-1} [a]	44
MS1054	10:56:59.5	-03.37:28.4	0.83	89	1170	9.6$\pm$0.8 [b]	16
CL0016	00:18:33.6	+16.26:16.0	0.55	$>$ 200	1230	$>$ 10 [c]	37
CL1604	16:04:18.3	+43:04:38.4	0.9	20-40	982	$>$ 8 h^{-1} [d]	2.0
A370	02:39:52.5	-01.39:52.5	0.37	$>$ 324	1350	(4-6)h^{-1} [e]	2.37 h^{-2}
CL0303	03:06:18.7	+17:18:03.7	0.42	$\sim$ 200	912	0.98$\pm$0.31 [b]	1.05 h^{-2}

[a] - Within a central radius of 0.97 h^{-1} Mpc (Donahue et al. 2003).

[b] - Within a central radius of 1 Mpc (Jee et al. 2005, Kaiser et al. 1998).

[c] - The central cluster radius was not specified for this case (Geach et al. 2012).

[d] - Within a central radius of 0.77 Mpc (Postman et al. 2001).

[e] - Within a central radius of 0.35 Mpc (AbdelSalam et al. 1998).

2.2 Data Reduction

As stated above, the image reduction process on all images used in this thesis was performed by Dr Steven M. Crawford prior to the start of the thesis. The following is an outline of the basic image reduction steps performed for images taken with the Mini-Mosaic Camera, reproduced with permission from Dr Crawford's webpage[2]:

1. Use Saha's preproc3 task on the biases and flats (with flags 0,0), e.g.: preproc3, "zero000.fits","zero000.fits",0,0; and on the object frames with appropriate flags, e.g.: preproc3,"obj000.fits","obj000.fits",3,0.

2. Use the adgmask IDL task to create masks of any ghosts, which has the same syntax as "preproc3" but without flags needing to be set, e.g.: adgmask,"obj000.fits", "mask000.fits"

3. Run the *IRAF* tasks mscred.ccdproc, -.zerocombine, -.flatcombine, on the bias, flat, and object frames

4. Turn the object frames into one image using the *IDL* task "adg.mosmaker"

5. Turn the mask frames into one mask image using the *IDL* task "adg.masmaker"

6. Transfer the header information using the *IDL* task "adg.headercopy"

7. Make the illumination image and correct the data, by performing the following tasks:

[2] http://www.astro.wisc.edu/~crawford/Projects/WLTV/minimo-rdx.html.

Table 2.2: R-band observation dates for our cluster sample.

Cluster	Frame ID	Observation date
CL0016+16	tw01.1099	15-10-1999
CL0016+16	tw01.1299	15-12-1999
CL0016+16	tw01.1200	15-12-2000
CL0016+16	tw01.1001	18-10-2001
CL0016+16	tw01.0902	12-09-2002
CL0016+16	tw01.0904	15-09-2004
A370	tw03.1299	15-12-1999
A370	tw03.1000	15-10-2000
A370	tw03.1001	18-10-2001
A370	tw03.1202	06-12-2002
A370	tw03.0904	15-09-2004
CL0303+17	tw04.1099	16-10-1999
CL0303+17	tw04.1100	15-11-2000
CL0303+17	tw04.1200	15-12-2000
CL0303+17	tw04.1001	16-10-2001
CL0303+17	tw04.1202	06-12-2002
CL0303+17	tw04.0904	15-09-2004
CL0303+17	tw04.1004	06-10-2004
MS0451-03	tw05.1099	14-10-1999
MS0451-03	tw05.1299	15-12-1999
MS0451-03	tw05.1100	18-11-2000
MS0451-03	tw05.1200	26-12-2000
MS0451-03	tw05.1001	15-10-2001
MS0451-03	tw05.1101	09-11-2001
MS0451-03	tw05.1004	06-10-2004
MS1054	tw07.0200	15-02-2000
MS1054	tw07.0301	15-03-2001
MS1054	tw07.0403	22-04-2003
MS1054	tw07.0204	16-02-2004
MS1054	tw07.0304	26-03-2004
MS1054	tw07.0305	02-03-2005
CL1604	tw10.0200	15-02-2000
CL1604	tw10.0300	15-03-2000
CL1604	tw10.0201	15-02-2001
CL1604	tw10.0401	26-04-2001
CL1604	tw10.0602	15-06-2002
CL1604	tw10.0602	15-06-2002
CL1604	tw10.0403	22-04-2003
CL1604	tw10.0503	30-05-2003
CL1604	tw10.0602	24-02-2004
CL1604	tw10.0602	26-05-2004

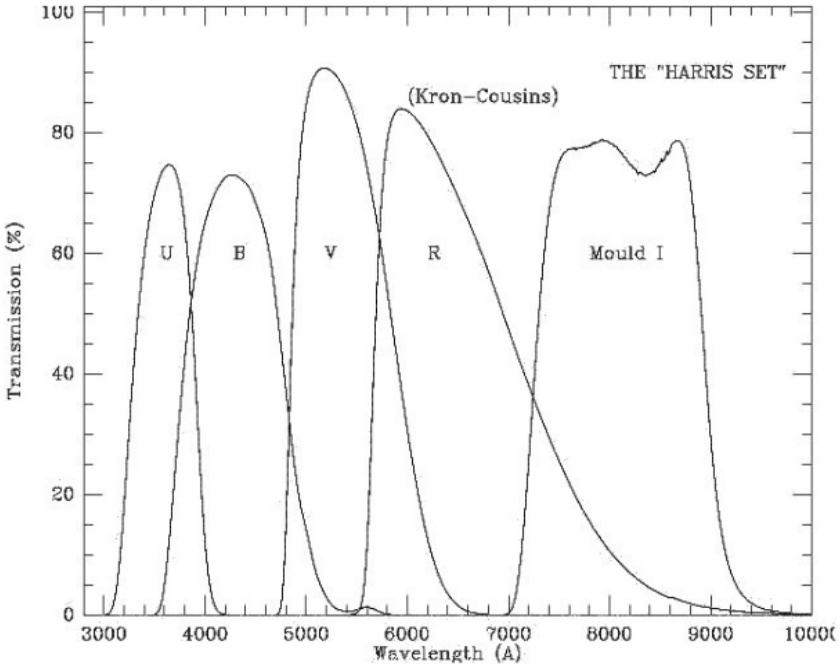

Figure 2.8: The "Harris Set" utilized in acquiring the observational data (with the exception of the V filter) used in this thesis. Figure from MNL02.

Table 2.3: Properties of the Harris *UBRI* filters in the WLTV Survey

Filter	Central Wavelength (Å)	Fullwidth at Half Maximum - FWHM (Å)	Maximum Transmission (%)
U	3594.68	642.34	77.68
B	4326.62	1038.78	66.72
R	6460.54	1526.12	82.57
I	8386.92	2090.08	93.17

- Run the *IRAF* task "cira.makemask" on the images to make the object mask (omask)
- Multiply the new masks by the old masks, obtained in step 2
- Combine all the images with masks optimally by setting the *IRAF* parameters weight, scaling and combine all to median, and rejection=avsigclip
- Minimize or maximize that image to near the level of the sky
- Run the *IRAF* task "ccdred.mkillumcor" on that image
- Take the inverse of the image made by mkillumcor; and then
- Run the *IRAF* task "ccdred.ccdproc" with the new image set as the illumination correction.

8. Make a sky image by mosaicing all the images in a given filter, using the object masks again and the same settings. Normalize the sky image to each image and

then subtract it, making use of the *IDL* task "adg.fringeremove"

9. Subtract any low order surface from the images using the *IDL* task "adg.imageflatten" by performing the following tasks:

   - Make a temporary image out of the product of a given image and omask (obtained in the first bullet in step 7). Ensure that omask is set to a value of 0 or 1
   - Use imsurfit with order 2 on the temporary image to create a surface image
   - Subtract the created surface image from each image.

10. Multiply the images and the masks by the super mask to account for growth in bad columns. This marks the end of the reduction process for images taken with the Mini-Mosaic Camera. The images are named according to the cluster ID, the band and original ccd number as well as the date (month and year) of the observation run. For example, in the image name *tw05.R128.1004.fits*, tw05 is the WLTV cluster ID, R128 means the R-band with a ccd number of 128 and 1004 represents the month and year of the observation run.

2.3 Summary

To summarize, we have photometric data on 6 clusters observed in the redshift range $0.3 < z < 0.9$. On average, each cluster was observed at least once a year over the duration of the Survey. Nearly all our observations were performed more than once for each cluster on a given night, with some clusters observed up to 4 times in one night, as Figure 2.1 has demonstrated.

Chapter 3

Transient Detection Methods

We present an account of two transient detection methods that were considered in this thesis. The one method is performed using the "IRAF image subtraction algorithm" and the other is carried out with the "ISIS image subtraction algorithm" (Alard & Lupton 1998; Alard 2000) that we have modified slightly for our data sample. The IRAF method was only performed on the cluster MS0451-03 and due to the length of time taken to perform the transient search, we looked into developing an automated version of the process that we then applied to all the clusters. We discuss the steps of each algorithm in detail in the next sections.

3.1 IRAF image subtraction algorithm

IRAF[1] is a general purpose open source software developed to, as the name suggests, reduce and analyze astronomical data. We discuss in the following sub-sections the steps performed in developing differenced images under the IRAF image subtraction algorithm.

3.1.1 Selecting a Reference Frame

This step is performed by determining the full width at half maximum (FWHM) of the point spread function (PSF) for each image, using the IRAF task *imexam*. The PSF is defined as the spread of a theoretical point in an image. It provides a description of how light rays from an astronomical source are distributed or spread at the plane of the detecting instrument on the ground. The FWHM for each image was determined by taking the average of the measured FWHM for three unsaturated stars in that image. The same three stars were used in performing this task in all frames. The image yielding the lowest average FWHM is taken to be the reference image, if it does not suffer from a considerable amount of artifacts or else the next image with the closest lowest average FWHM is adopted as the reference image. The selected reference frame for MS0451-03

[1] IRAF is written and supported by the National Optical Astronomy Observatories and operated by the Association of Universities for Research in Astronomy, Inc. under cooperative agreement with the National Science Foundation

was *tw05.R186.1001.fits* shown in Table 3.1, with an average seeing value of 0.524.

3.1.2 Matching the Seeing

After selecting the reference frame, the images are convolved and PSF matched using the IRAF task *gauss*. From the determined FWHM of each image, we derive the pixel standard deviation for each image σ_{image}, using the relation

$$FWHM = 2\sqrt{2ln2}\sigma_{image} \simeq 2.354\sigma_{image} \tag{3.1}$$

In this thesis, we created what we called image convolution brackets or categories that all images were categorised into. These categories were (i) $\sigma_{image} < 2.3$, (ii) $2.3 < \sigma_{image} < 3.0$, (iii) $3.0 < \sigma_{image} < 4.0$, (iv) $4.0 < \sigma_{image} < 5.0$, (v) $5.0 < \sigma_{image} < 6.0$ and so on. The individual images were placed into one of the categories that contained their determined value of σ_{image}.

All images belonging to the same convolution category are convolved to the same seeing[2] defined by the upper bound of each convolution category, which we call σ_{cc}.The seeing of an image is obtained from its determined FWHM via the relation

$$Seeing = FWHM \times pixel\ scale, \tag{3.2}$$

where pixel scale refers to the angular size covered on the sky by a single pixel on a CCD. The WIYN WLTV Mini-mosaic camera described in Chapter 2 has a pixel scale of 0".14 per pixel. Tables 3.1 and 3.2 provide summaries for many of the points we have discussed thus far for the 16 images of the cluster MS0451-03. The motivation behind the establishment of the convolution categories is to avoid the deterioration of the signal to noise among the images that would otherwise be encountered if all images were convolved to the seeing of the worst frame, as it is done with traditional IRAF methods.

The convolution kernel values (denoted by σ_c in (3.3)) given in column 4 of Table 3.1 for the individual images represent input parameters to the gauss task to convolve each image to the seeing specified by the upper bound σ_{cc} of the convolution category it falls into. The parameters are determined from the equation

$$\sigma_c = \sqrt{\sigma_{cc}^2 - \sigma_{im}^2}. \tag{3.3}$$

We wish to caution that although the value of σ_{image} determined for the reference image dictates that it belongs to the first category, it is repeatedly utilised in each convolution bracket by convolving it to the seeing defined by the upper bound of each

[2]The seeing of an astronomical image refers to the amount of atmospheric turbulence introduced in the image as a result of the interaction between atmospheric gas particles and light rays, as they travel from an astronomical source to the detector on the ground. The higher the turbulence, the larger the seeing.

Table 3.1: Photometric properties of the 16 images for the cluster MS0451 with their determined convolution kernels and scaling factors. The scaling factors are required for scaling the flux of images to match that of the reference image.

Image	Average FWHM	Average Seeing	σ_{im}	Convolution kernel	Scaling Factor
tw05.R186.1001.fits	3.74	0.524	1.5887850	1.663058049	1
tw05.R191.1001.fits	4.47	0.626	1.8988955	1.297765731	1.006309092
tw05.R128.1004.fits	4.787	0.670	2.0335599	1.074539037	0.838112448
tw05.R125.1004.fits	4.793	0.671	2.0361088	1.069701432	0.837206616
tw05.R3075.1299.fits	4.943	0.692	2.0998301	0.938463452	1.954595886
tw05.R124.1004.fits	4.953	0.693	2.1040782	0.928899928	0.837765096
tw05.R3076.1299.fits	5.033	0.705	2.1380629	0.847754184	3.980934746
tw05.R121.1004.fits	5.057	0.708	2.1482583	0.821575527	0.858362868
tw05.R113.1200.fits	5.545	0.776	2.3555650	1.857771124	0.937194299
tw05.R106.1100.fits	5.727	0.802	2.4328802	1.157681554	0.961095792
tw05.R114.1200.fits	6.515	0.912	2.7676296	1.063909538	0.961537375
tw05.R2051.1099.fits	6.603	0.924	2.8050127	0.867925518	1.124392537
tw05.R105.1100.fits	6.76	0.946	2.8717077	1.011451551	0.982795521
tw05.R092.1101.fits	9.11	1.275	3.8700085	2.817740422	1.04376178
tw05.R091.1101.fits	9.723	1.361	4.1304163	2.817740422	1.04110842
tw05.R124.1099.fits	10.97	1.536	4.6601529	1.811898162	1.10877559

bracket, using its determined convolution kernel parameters given in column 3 of Table 3.2.

Table 3.2: Standard deviation for the convolution categories, σ_{cc} and convolution kernel for the reference image in the four convolution categories.

Convolution category	Standard deviation of convolution category, σ_{cc}	Convolution kernel reference image
$\sigma_{im} < 2.3$	2.3	1.66
$2.3 < \sigma_{im} < 3.0$	3.0	2.54
$3.0 < \sigma_{im} < 4.0$	4.0	3.67
$4.0 < \sigma_{im} < 5.0$	5.0	4.74

3.1.3 Correct for Atmospheric Extinction

Dust and gases in the Earth's atmosphere have the ability to absorb and scatter some of the photons from astronomical sources. This results in a reduction of the total amount of photons registered by a detector on the ground, causing mismatches in the total flux of the images. This process is known as atmospheric extinction and is corrected for by matching the flux of each convolved epoch image created in the previous step to the flux of the convolved reference image in a given convolution category.

3.1.4 Create the Difference Image

The convolved reference frame in each convolution category is subtracted from each convolved and flux matched frame falling within that category to produce difference images.

3.1.5 Create the Signal to Noise Image

The produced difference images are normalised by their corresponding error images and the error image of the reference frame. This is done in order to smooth out the photon count fluctuations that are inherent in the images (Poisson uctuations). An error image is produced from taking the square root of the absolute value of each PSF and flux matched image. The normalization produces the desired signal to noise (S/N) images that we then thoroughly visually scan for signs of potential transient objects.

3.1.6 Detect the Transients

As stated in the previous sub-section, potential transient candidates are located by visually scanning thoroughly across the S/N images. Caution is exercised to not confuse false detections of transients with genuine transients. False detections are caused by saturated stars that fail to subtract properly and some other objects such as cosmic rays, which usually are only present in one frame and not in the rest of the frames taken on the same night.

3.1.7 Summary

We summarise in this sub-section the main steps involved in the IRAF image subtraction algorithm, using the reference frame *tw05.R186.1001.fits* and the epoch frame *tw05.R128.1004.fits* in Figure 3.1 for illustration.

1. Identify reference image
2. PSF match the images (seeing matching)
3. Correct for atmospheric extinction (flux matching)
4. Subtract the resultant reference image from the psf and flux matched epoch image to produce a difference image
5. Normalise the difference image with its corresponding error image to produce the S/N image (Figure 3.2).

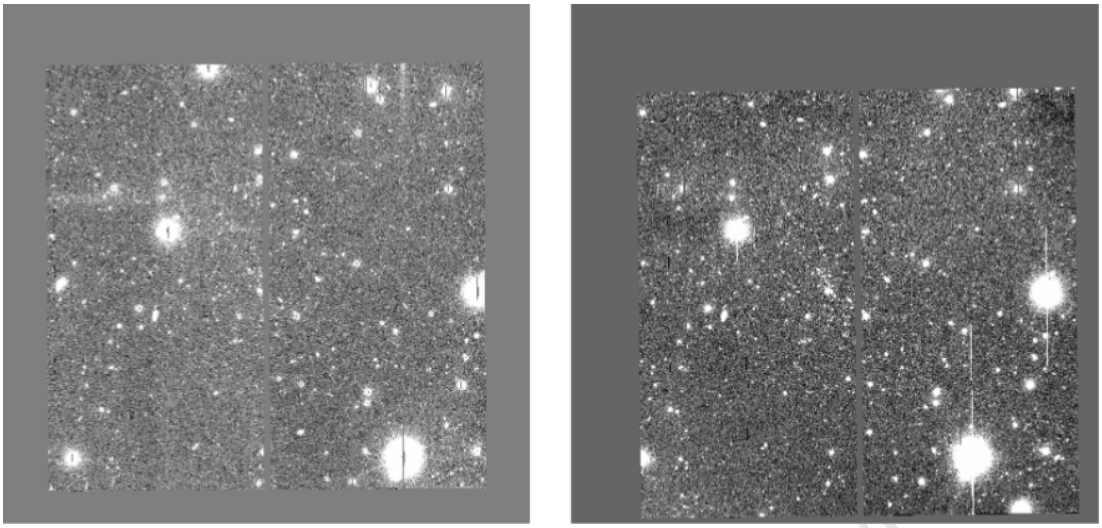

Figure 3.1: Reference image tw05.R186.1001.fits (left panel) and epoch image tw05.R128.1004.fits (right panel). The two frames are PSF and flux matched before subtraction.

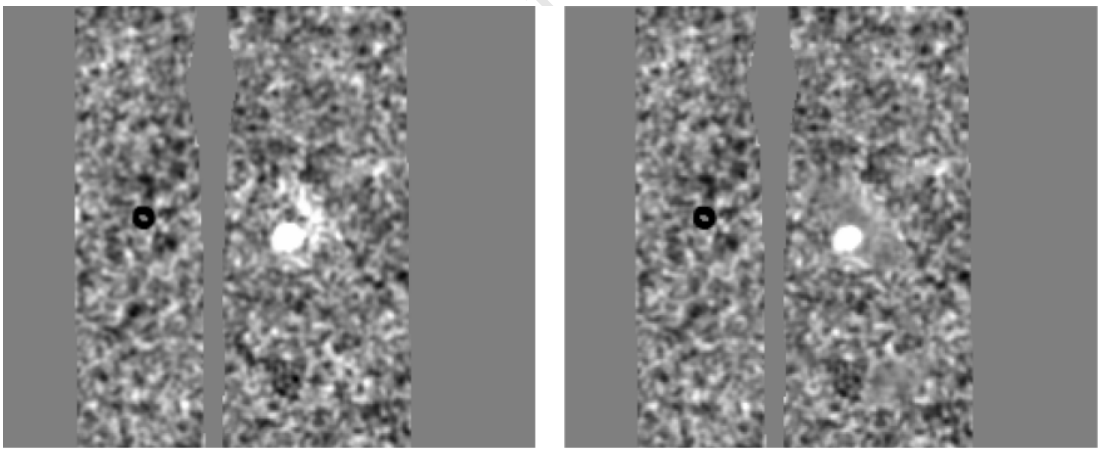

Figure 3.2: Difference image *dtw05.R128.1004.R186.1001.fits* (left panel) and its S/N image *sntw05.R128.1004.R186.1001.fits* (right panel), zoomed in on the bright foreground SN candidate discovered in the epoch frame *tw05.R128.1004.fits*. The tiny bright areas seen to the right and above the SN candidate in the difference image, believed to be due to photon noise, are smoothed out in the S/N image as a result of normalization of the difference image by error images. The missing data column in the middle is a propagation of an artifact from the reference frame and the columns on the left and right boundaries of the images correspond to ccd gaps in the epoch and reference frames.

3.2 ISIS image subtraction algorithm

Our main transient detection method in this exercise is an automated algorithm that makes use of the ISIS image subtraction package described by Alard & Lupton (1998) and Alard (2000). The package consists of C-shell scripts that call individual routines (written in the C programming language) to perform various tasks in the image differencing process. In its original form, the ISIS image subtraction algorithm could not process our data sample. We performed a number of modifications to the code's C-shell scripts and appended extra (python) scripts to the code to bring it into a form that could process our data successfully. The modifications made are discussed as they apply to the various sub-sections below. During the PSF and image differencing steps described below, the algorithm divides the image into smaller regions, process them individually and then mosaic the individual processed regions into a complete frame. We discuss in the following sub-sections the steps performed under this algorithm.

3.2.1 Selecting a Reference Frame

Just as in the IRAF algorithm, we start by determining the reference image from measurements of the FWHM of three stars in each image using the exact same approach followed in the IRAF algorithm and have *tw05.R186.1001.fits* as our selected reference frame for MS0451-03.

3.2.2 Remove Blank Regions

Unlike in the IRAF algorithm, the ISIS code cannot process blank regions around the images. An area containing data common to all the images is determined and cropped out of the original images, for use in the ISIS code. This is accomplished with a script written in python. Table 3.3 shows the sizes of the original and cropped out images for all clusters, needed for the automated algorithm.

Table 3.3: Sizes of the original cluster images and cropped out images for our cluster sample.

Cluster	Number of images	Size of original images (pixels)	Size of cropped out images (pixels)
MS0451-03	14	5000 × 5000	3600 × 3600
MS1054-03	11	5000 × 5000	3200 × 3200
CL0016+16	13	6000 × 6000	3200 × 3200
CL1604+4304	23	6000 × 6000	3200 × 3200
A370	12	6000 × 6000	2800 × 2800
CL0303+17	15	6000 × 6000	3200 × 3200

Following the selection of a reference image and reduction of original images to sizes that do not contain blank regions and common to all images for a given cluster, the steps below, akin to the IRAF algorithm, are performed and we describe each one of them.

3.2.3 Image registration

This step was not performed in the IRAF algorithm as the images for all clusters in our sample have undergone image alignment. Nonetheless, we performed it under the ISIS algorithm, as it forms an integral part of the automated process. Under this step, the code starts by re-mapping the coordinates of objects in all images to their corresponding counterparts in the reference image. The process is referred to as "astrometric" transformation and the transformation factor is determined by fitting a 2-dimensional polynomial using up to 500 stars from both the epoch and reference images (Alard & Lupton 1998). This process is triggered by the C-shell script "interp.csh".

3.2.4 Create a Composite Reference Frame

The next step in the package after registering the images to the reference frame is to create a composite reference frame by stacking a number of good seeing frames and the recommendation is to use 10 percent of the total images for a given cluster to do the stacking (See "A TUTORIAL TO ISIS2.1")[3]. This step however introduced bad regions and peculiar shapes in our resultant composite reference frame that propagated onwards to cause distorted shapes in the difference images (discussed in the next sub-section). To mitigate this effect, we attempted using only the reference frame selected in 3.2.1 as the composite reference frame and the resultant difference images met our expectations. We therefore adopted the reference frame to be the composite reference image and tweaked the C-shell scripts to recognise this change.

3.2.5 Mask off Brighter Stars

Unlike in the IRAF algorithm, saturated stars and some other brighter stars were masked off under the automated algorithm, to avoid errors that we encountered in determining the optimal convolution kernel solution by the algorithm, for each of the individual regions in an image. The presence of much brighter stars in some regions of an image led to a distortion of those regions in the subtracted image and masking them out as shown in Figure 3.3 proved to fix our problem.

3.2.6 Match the Seeing and Flux

Unlike in the IRAF algorithm, the reference image in the case of the automated algorithm is not degraded to the worst seeing frame but the PSF matching and atmospheric correction is performed between each individual image and the reference image. The advantage of doing this is to preserve the signal to noise ratio in the reference image, which otherwise gets lowered when it is convolved to the seeing of the worst frame. The ISIS automated algorithm attempts to use all available information in an image to derive

[3] The tutorial is accessible from http://www2.iap.fr/users/alard/package.html.

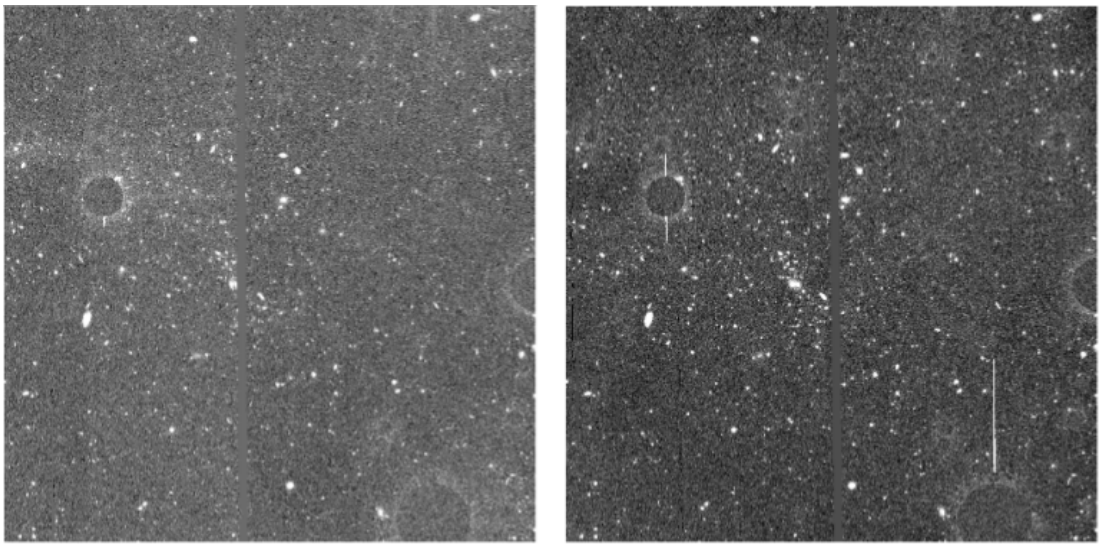

Figure 3.3: Reference image *tw05.R128.1004.fits* (left panel) and the epoch image *tw05.R186.1001.fits* (right panel), both reduced to the common maximum size of 3600 × 3600 pixels containing no blank regions around the edges for all images of the cluster MS0451-03. The masks over the three brightest saturated stars are also visible.

a convolution kernel that gives the optimal image subtraction solution (Alard & Lupton 1998). The optimal convolution kernel solution is modeled from a set of Gaussian functions combined with polynomial functions and least square solution methods.

3.2.7 Create the Difference Image

The adopted composite reference frame is subtracted from each PSF and flux matched image by launching the script "subtract.csh", which triggers the "mrj_phot" code within the package to produce difference images (shown in Figure 3.4). Matching the seeing and flux between the composite reference frame and each epoch frame is also accomplished via the script "subtract.csh".

3.2.8 Create the Signal to Noise Image

The produced difference images are normalized by the sum of the photon noise expected from the two images in the pair (the equivalent of error images in the IRAF algorithm) to produce what we refer to as signal-to-noise (S/N) images (called "var.fits" images in the algorithm) that transients are located in, just as in the IRAF algorithm. The S/N images are created via the script "detect.csh". The original cluster images had areas with known artifacts for which masks were developed. These masks were applied to the developed S/N images using a python script that we incorporated into the algorithm, in order to reduce the detection of false transients.

3.2.9 Detect the Transients

The automated algorithm locates the position of all transients that meet a set minimum detection threshold via the script "find.csh" and exports their x and y pixel coordinates to a file. The green highlighted areas seen in the S/N image in Figure 3.4 indicate the positions of such transients.

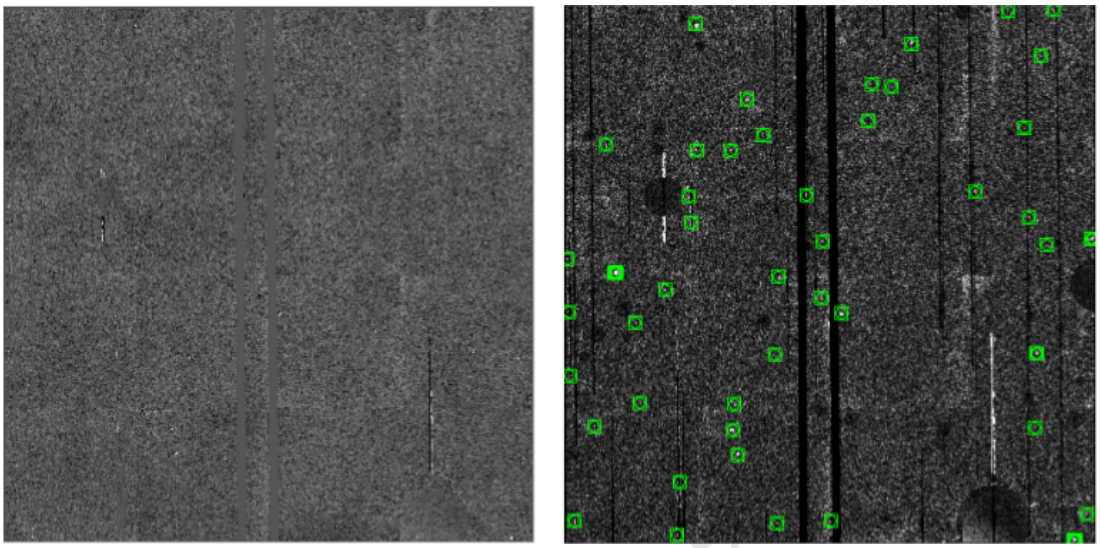

Figure 3.4: Difference image (left panel) and S/N image (right panel) developed from the pair in Figure 3.3. The green squares shown in the S/N image highlight the positions of discovered transients that met the set minimum detection threshold of a signal to noise of 5.

Below is a summary of the main steps involved in the image subtraction and transient recovery process, using the ISIS automated image subtraction algorithm.

1. Measure the $FWHM$ of at least three stars in an image to determine the reference frame. This is performed in IRAF.

2. Crop out of the original images an image that does not contain blank regions around the edges and common to all the images. For MS0451-03, this corresponds to an image size of 3600 × 3600 pixels (Table 3.1).

3. Apply the *ISIS* automated image subtraction and transient recovery steps:

   - **interp.csh** - performs the coordinate matching of objects between the reference frame and each epoch frame
   - **ref.csh** - produces a composite reference frame for use in the image subtraction process. We did not make use of this step for our case
   - **subtract.csh** - triggers the "mrj_phot" program to model the best convolution kernel solution and performs image subtraction
   - **detect.csh** - normalizes the difference images with sum of the photon noise from the two images

- **find.csh** - produces a text file containing the x and y coordinates of the discovered transients.

3.3 Comparison of the Detection Methods

Both image subtraction algorithms performed well in locating transients in the cluster images and as would be expected, the automated algorithm performs the search much faster than its IRAF counterpart. The time span from identifying the reference frame to producing difference images for a cluster with an average of 16 images with sizes similar to those given in Table 3.1, is ∼1 week with the IRAF algorithm, but ∼1/2 a day with the automated algorithm.

3.3.1 Number of detected transients

We compare the number of transients detected with each of the two algorithms in the cluster MS0451 that the IRAF algorithm was only applied to. Table 3.4 provides the total number of transients, including real and artifacts, and the viable transients. By viable, we mean SN candidates, variable stars, AGN candidates and asteroids. However, the classification of variable stars is a concept we do not have a full grasp of, so the value provided in Table 3.4 for viable transients does not include variable stars.

Table 3.4: A comparison of the total number of transients found by the IRAF and ISIS search algorithms for the cluster MS0451.

Algorithm	Transients					
	SN candidates	AGN candidates	Asteroids	Cosmic rays	Other[a]	Total
IRAF	3	0	0	7	28	38
ISIS	1	0	0	2	22	25

[a] - Other include bad pixels, variability due to bad subtraction and perhaps variable stars, and other possible artifacts.

The larger number of cosmic rays detected with the IRAF algorithm compared to the ISIS algorithm is possibly due to the fact that the original size images were reduced under the ISIS algorithm (see Table 3.3), resulting in a reduced transient search area in the images.

3.3.2 Detection threshold

Images in the top row of Figure 3.5 shows the three SN candidates discovered with the IRAF algorithm and those in the bottom shows the corresponding exact regions of the images processed with the automated algorithm.

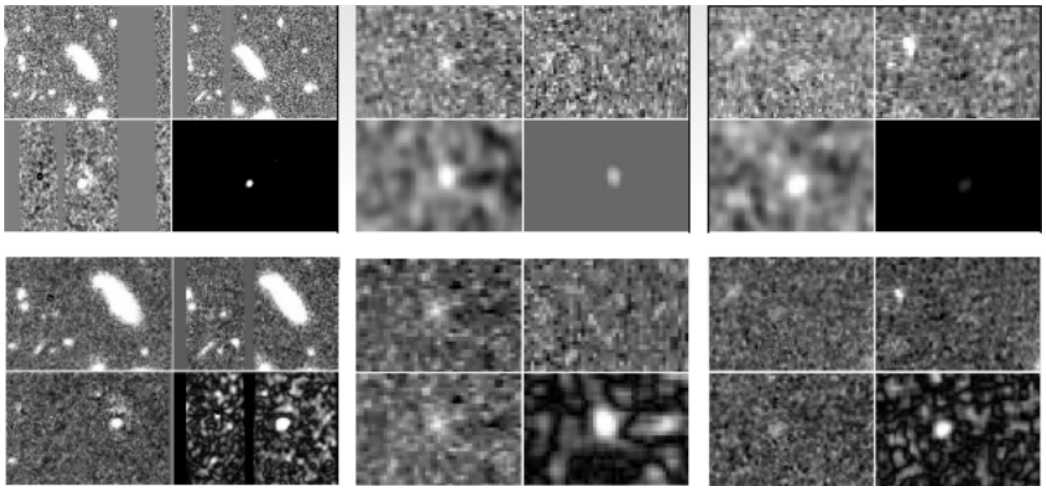

Figure 3.5: Top row: the three MS0451-03 SN candidates; MS0451_SN1, MS0451_SN2 and MS0451_SN3, discovered in the frames *tw05.R128.1001.fits*, *tw05.R114.1200.fits* and *tw05.R106.1100.fits* respectively, with the IRAF algorithm. Bottom row: comparison of their detection with the ISIS algorithm, where the last two were not detected at a SNR = 5 set to be the detection threshold for the ISIS pipeline. Each panel is made out of four images: Epoch (upper left), Reference (upper right), Difference (bottom left), S/N (bottom right).

The minimum transient detection threshold was set to a SNR of 5 for all clusters, to reduce the high noise level encountered at SNR < 5. This resulted in the SN candidates MS0451_SN2 and MS045_SN3 going undetected under the automated algorithm. Lowering the SNR to 3 under the automated algorithm resulted in the detection of only MS0451_SN2. MS0451_SN3 could only be detected at SNR cut of 2.5 along with many other objects that were comparable to the background noise. We therefore increased the SNR cut to 5 for all clusters to increase our chances of detecting candidates that were reasonably well above the noise level. Our derived result for the cluster SN Ia rate in Chapter 4 with the automated algorithm is therefore only accurate to a SNR cut of 5.

3.4 Detected transients and their classification

Among the overall number of discovered transients in our cluster sample were SN candidates, asteroids, AGN and variable star candidates. As pointed out in sub-section 3.3, Classification of the variable stars is an exercise beyond the scope of this thesis. We therefore only list in Table 3.5 the discovered AGN and SN candidates and some of the transients we classified as asteroids, along with their RA and DEC determined using the NED "X/Y offset calculator to RA and DEC"[4].

3.4.1 Classification of the transients

We describe the criteria followed in classifying the transients listed in Table 3.5.

[4]The NED "XY offset calculator to RA and DEC is described further in section 4.1

Table 3.5: Supernovae, Active Galactic Nuclei and some Asteroid candidates discovered in the cluster images, along with their determined RA and DEC and date of observation.

Transient candidate	RA (J2000)	Dec (J2000)	Observation date
MS0451_SN1	04:54:12.4	-03:00:45.0	06-10-2004
MS0451_SN2	04:54:18.2	-02:59:06.7	26-12-2000
MS0451_SN3	04:54:05.12	-03:01:28.46	18-11-2000
MS1054_AGN1	10:57:11.1	-03:38:33.8	22-04-2003
MS1054_asteroid1	10:57:01.1	-03:34:42.2	15-02-2000
MS1054_asteroid2	10:56:46.6	-03:36:33.0	22-04-2003
MS1054_asteroid3	10:56:49.2	-03:39:18.3	15-03-2001
CL0016_asteroid1	00:18:30.2	+16:25:40.6	15-12-1999
CL0016_asteroid2	00:18:45.3	+16:24:29.6	12-09-2002
CL0016_asteroid3	00:18:23.6	+16:22:38.7	15-10-1999
CL0016_asteroid4	00:18:46.8	+16:23:23.0	15-09-2004
CL0016_asteroid5	00:18:46.8	+16:23:22.9	18-10-2001
CL0016_asteroid6	00:18:46.9	+16:23:16.9	15-12-2000
CL1604_AGN1	16:04:14.4	+43:01:32.0	30-05-2003
A370_AGN1	02:40:02.9	-01:35:22.0	06-12-2002
A370_asteroid1	02:39:51.2	-01:33:57.0	06-12-2002
CL0303_SN1	03:06:10.6	+17:19:07.8	15-10-2001
CL0303_AGN1	03:06:36.6	+17:16:38.0	15-11-2000
CL0303_asteroid1	03:06:28.9	+17:18:06.7	06-10-2004
CL0303_asteroid2	03:06:31.9	+17:15:09.3	16-10-2001
CL0303_asteroid3	03:06:53.2	+17:18:43.0	15-11-2000
CL0303_asteroid4	03:06:38.2	+17:19:47.0	06-12-2002
CL0303_asteroid5	03:06:27.6	+17:16:45.0	15-09-2004
CL0303_asteroid6	03:06:28.7	+17:18:44.0	16-10-1999

3.4.1.1 Supernova candidates

One of the criteria that we followed in classifying the discovered transients as SN candidates is via observation of a conspicuous bright object in the differenced image. The position of such an object was found to coincide with that of galaxy with an overwhelming increase in its brightness compared to the brightness it has in the reference image. Figure 3.6 gives such an example for the SN candidate CL0303_SN1.

MS0451_SN1 appears to have caused the observed increase in size/brightness of its perceived host galaxy, the brightest elongated object with a north-west to south-east orientation in the upper left and right panels of the four pane diagrams of images in the first column of Figure 3.5.

The candidates MS0451_SN2 and MS0451_SN3 however did not conform to this criterion, as there were no apparent host galaxies at their discovered locations, as shown in the second and third columns of Figure 3.5. The two candidates are likely to be hostless cluster events.

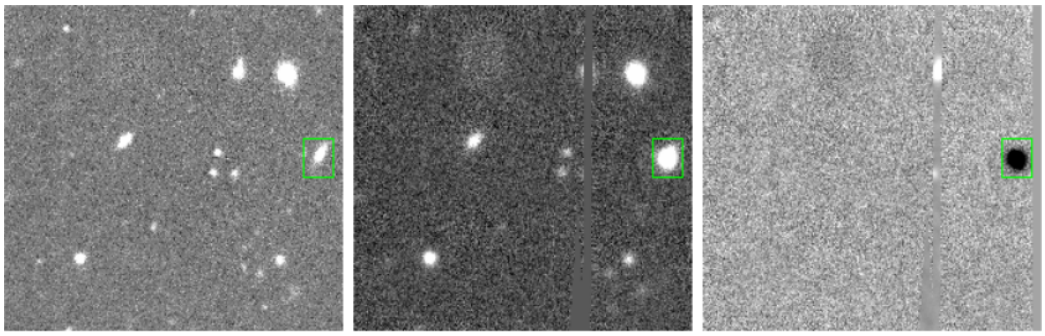

Figure 3.6: Left: reference frame *tw04.R115.1004.fits* for CL0303+17 with the suspected host galaxy for CL0303_SN1 contained inside the rectangle; Middle: epoch frame *tw04.R051.1001.fits* for the same cluster showing an overwhelming in the brightness of the same galaxy, believed to be due to a SN event; Right: difference frame *conv_tw04.R051.R1001.fits* developed from the reference and epoch frames, showing the residual SN candidate CL0303_SN1.

3.4.1.2 Asteroids

We classified transients observed to shift in position by a considerable amount of pixels on timescales of minutes as asteroids. The manner in which this shift was detected was through observations of the same object in other frames taken on the same night with cadences of tens of minutes or hours in some cases. Figure 3.7 shows an example of such objects observed in two frames *tw01.R104.0902.fits* and *tw01.R105.0902.fits* with a cadence of 13.38 minutes, for the cluster CL0016+16.

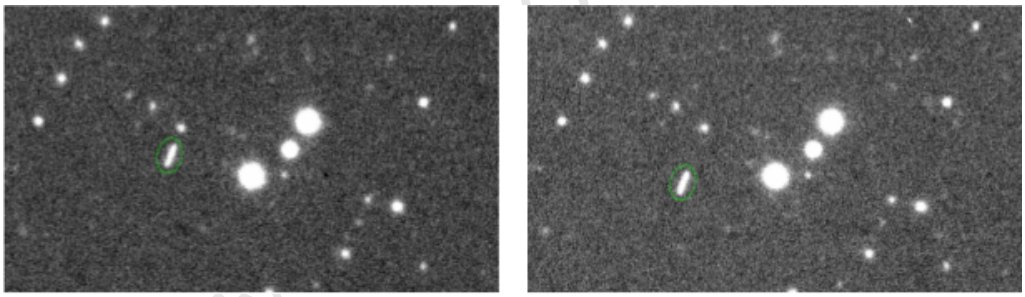

Figure 3.7: Asteroid candidate "CL0016_asteroid2" enclosed inside the two green ellipses shown, detected in the frames *tw01.R104.0902.fits* (left panel) and *tw01.R105.0902.fits* (right panel) with a cadence of 13.38 minutes between the frames. The asteroid was found to have shifted in position between the two images by approximately 15 pixels in the leftward x direction and 45 pixels in the downward y direction.

Candidate asteroids appear in the images as streaks (elongated) and not as point sources due to their fast constant motions during exposures, which takes approximately 10 minutes for each frame.

3.4.1.3 Active Galactic Nuclei

We classified transients observed to show variability in many of the frames taken over the duration of the survey to be Active Galactic Nuclei (AGN). A370_AG1 located at an RA and DEC of 02:40:02.9 and -01:35:22.0 respectively in A370, was found to display

variability in seven frames observed between December 1999 and 2002. Other classified AGN candidates given in Table 3.4 were found to show similar variabilities in their fields they were located.

Chapter 4

Data Analysis and Results

As discussed above, only two cluster SN candidates MS0451_SN1 and CL0303_SN1 were found with the automated algorithm in the clusters MS0451-03 and CL0303+17 respectively, at a detection threshold of SNR = 5. The derivation of our cluster SN Ia rate involves normalising the total number of discovered SN Ia candidates in a given cluster by the total luminosity L_{tot}, within the search area of that cluster, the survey's detection efficiency ϵ and duration T in years, as will be discussed below. Determination of parameters that goes into the calculation of L_{tot} is beyond the scope of this thesis and reserved for future work. We turn to the literature for such parameters to approximate the value of L_{tot} that we require. Although we have not detected any SN candidates for the rest of the clusters considered in this thesis, we nonetheless attempt to place upper limits on the number of SNe Ia that we expect to find in these clusters. We have neither spectroscopic nor photometric redshift information for our discovered SN candidates. We assume their redshifts (with exception of MS0451_SN1, see discussion below) to be the same as their cluster redshifts.

4.1 Cluster search area membership for SN candidates

Our cluster search area is within 1 Mpc of the cluster centre. This choice of the search area is purely based on the cluster search areas used by a number of authors in performing cluster SN Ia rate measurements. Sharon et al. (2010) and Sand et al. (2012) both use 1 Mpc for the cluster search area. We make use of the former's work quite a lot in the derivation of our cluster SN Ia rate and to enable a comparison of our result to theirs like shown below, we use the same cluster search area as theirs.

To determine whether or not our discovered SN candidates are located within this search area, we use the "distance between two points $a1(x1, y1)$ and $a2(x2, y2)$" formula

$$d(a1, a2) = \sqrt{(x2 - x1)^2 + (y2 - y1)^2}, \tag{4.1}$$

to determine their locations from the cluster centre.

4.1.1 Search area membership for CL0303_SN1

CL0303_SN1 was discovered in the frame *tw05.R051.1001.fits* for the cluster CL0303+17, located at an RA and DEC of 03:06:18.66 and +17:18:03.37 respectively (Table 1.1). To determine the RA and DEC for CL0303_SN1, we make use of the NED[1] "X/Y offset to RA/DEC" tool using as inputs, its x and y pixel coordinates in *tw05.R051.1001.fits*, the cluster centre's RA and DEC and x and y pixel coordinates, also in the frame *tw05.R051.1001.fits* and the pixel scale of 0".14. Converting the RA and DEC for CL0303_SN1 and the cluster centre into degrees, we determine using (4.1) CL0303_SN1's distance from the cluster centre in degrees. Conversion into Mpc using a distance scale D_s of 5.533 / arcsecond yields a distance of R = 0.756 Mpc from the cluster centre. CL0303_SN1 therefore does fall within our specified search area. The distance scale D_s is computed using the NED "Cosmology Calculator" using redshift of the SN candidate and the cosmology assumed in this thesis as inputs.

4.1.2 Search area membership for MS0451-03 SN candidates

The RA and DEC for MS0451_SN1 was determined in the same way as for as for CL0303_SN1, and was found to roughly be in good agreement with that of the foreground SN candidate "MS0451.6-0305-cand1" discovered by Sharon et al. (2010). Sharon et al. found "MS0451.6-0305-cand1" to be a foreground SN event, with a host galaxy redshift of $z = 0.16$. Based on this knowledge, we classified "MS0451_SN1" not a member of MS0451-03 but a foreground object.

Repeating the same search area membership determination procedure as above on the other two MS0451-03 SN candidates, we find the locations of MS0451_SN2 and MS0451_SN3 to be at distances R = 0.268 Mpc and R = 1.473 Mpc respectively from the cluster centre. We therefore only consider CL0303_SN1 and MS0451_SN2 in deriving cluster SN Ia rate for CL0303+17 and MS0451-03. Tables 4.1 and 4.2 summarise the determined properties for CL0303_SN1 and the three MS0451 SN candidates.

D_L which stands for luminosity distance is also an output of the NED Cosmology Calculator in determining the value of D_s and is used in the calculation of the absolute magnitude corresponding to the survey's detection limit, discussed in sub-section 4.4.3.

In the next sections, we give an account of the astrometic and photometric calibrations performed to derive the calibrated R-band magnitudes for CL0303_SN1 and MS0451_SN2, describe the steps involved in deriving the SN Ia rate for the clusters CL0303+17 and MS0451-03 and the rest of the clusters as well as discussion of the derived results. From here on, MS0451_SN1 and MS0451_SN3 will no longer feature in

[1] The NASA/IPAC Extragalactic Database (NED) is operated by the Jet Propulsion Laboratory, California Institute of Technology, under contract with the National Aeronautics and Space Administration.

Table 4.1: Summary of the determined properties of the SN candidate "CL0303_SN1" detected in the cluster CL0303+17.

Parameter	Cluster Centre	CL0303_SN1
x,y coordinates (pixels)	3667,2149	4488,2609
RA	03:06:18.66	03:06:10.62
DEC	+17:18:03.37	+17:19:07.50
z	0.42	0.42
R (degrees)	0.0	0.0379341724
D_s (kpc/")	5.533	5.533
R (Mpc)	0.0	0.7556031925
D_L (Mpc)	2301.1	2301.1

Table 4.2: Summary of the determined properties of SN candidates "MS0451_SN1", "MS0451_SN2" and "MS0451_SN3", detected in the cluster MS0451.

		SN candidate		
Parameter	Cluster Centre	MS0451_SN1	MS0451_SN2	MS0451_SN3
x,y coordinates (pixels)	2473,2233	2638,2145	2362,2519	964,1509
RA (degrees)	73.545	73.542	73.556	73.518
DEC (degrees)	-3.016	-3.008	-3.018	-3.074
z	0.538	0.16	0.538	0.538
R (degrees)	0	0.009	0.012	0.064
D_s (kpc/")	6.341	2.758	6.341	6.341
R (Mpc)	0.0	0.086	0.273	1.490
D_L (Mpc)	3093.7	765.4	3093.7	3093.7

our discussions below, as the former is not a cluster event and the latter lies outside the 1 Mpc cluster search area criterion.

4.2 Astrometic Calibration

Frames in which the SN candidates CL0303_SN1 and MS0451_SN2 were discovered were astrometrically calibrated to derive the actual R-band magnitudes for these sources. This was performed in ds9[2], where the epoch image containing the SN candidate was opened in one frame, and a digitized sky survey (DSS) image from the SAO-DSS server larger in size than the epoch image was uploaded in another frame.

4.2.1 Astrometric Calibration for CL0303+17

Figure 4.1 shows the epoch frame *tw04.R115.1001.fits* (left panel) and the SAO-DSS image used to perform astrometric calibration for the CL0303+17 field. To perform the

[2]ds9 is an astronomical imaging and data visualization programme developed by the Smithsonian Astrophysics Observatory (SAO).

calibration, identical stars between the two frames were crossed matched, as illustrated with green circles in the figure.

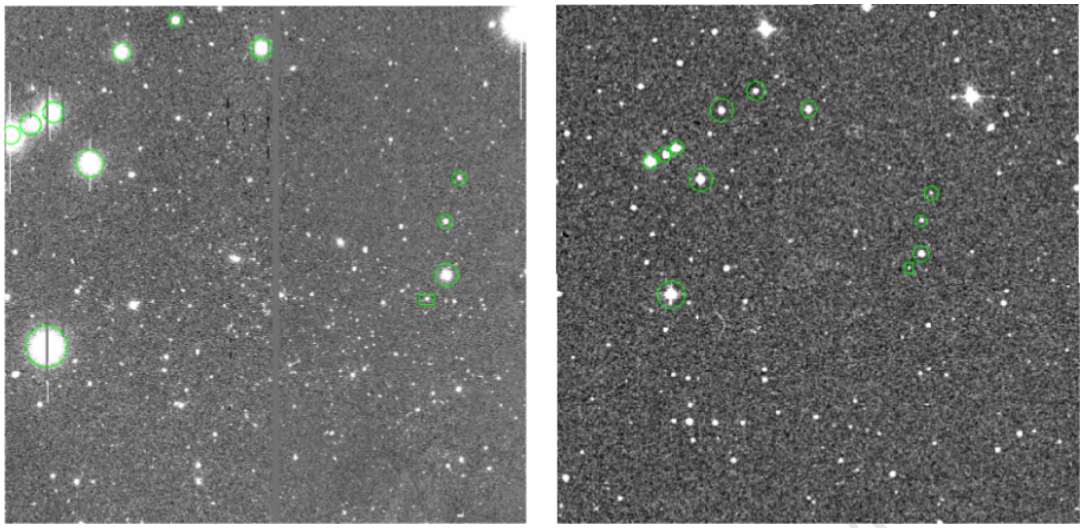

Figure 4.1: The epoch frame *tw04.R115.1004.fits* panel (left panel) and the SAO-DSS image (right panel) covering the entire field of our epoch image. The green circles in both frames illustrate corresponding stars used in carrying out astrometric calibration of the epoch frame. The rectangular boxes highlight the standard star used in the photometric calibration process described in the next sub-section.

The most obvious difference between the two frames is that corresponding objects are much brighter in the epoch image than in the SAO-DSS image due to the fact that our survey has a greater depth in comparison to the shallow DSS image. The implication of this is that only brighter objects can be seen in the DSS image, which mostly consist of stars in the Milky Way, whereas more objects, including stars and galaxies are detected in our epoch image.

4.2.2 Astrometric Calibration for MS0451-03

The astrometric calibration steps performed for CL0303+17 were repeated for MS0451-03 using the frame *tw05.R186.1001.fits* and its equivalent SAO-DSS frame. We have not bothered to illustrate this case with a figure similar to Figure 4.1, as the process is exactly similar to the case for CL0303_SN1.

4.3 Photometric Calibration

After completing the astrometric process, a stellar catalogue known as "The Guide Star Catalogue (GSC), version 2.2 (GSC 2.2)" was uploaded onto the SAO-DSS image to perform photometric calibration. We describe the individual processes for both "CL0303_SN1" and "MS0451_SN2".

4.3.1 Photometric Calibration for CL0303_SN1

We searched for nearest standard stars to the suspected host galaxy for CL0303_SN1 in the catalogue, that could have matches in the epoch frame *tw05.R051.1001.fits* that were free from artifacts and not unsaturated. We identified only one such candidate, enclosed by the rectangular boxes in the frames in Figure 4.1. The candidate standard star is located at an RA and DEC of 46.578306 degrees and +17.357573 degrees respectively, and has a catalogued R-band magnitude of $m_{std*,cat} = 17.66$. We then measured the candidate standard star's R-band magnitude in the epoch frame to be $m_{std*,im} = 9.82$, using the IRAF task *imexam*. We used the measured $m_{std,im}$ to derive the zero point magnitude of the observing instrument for the epoch frame using the equation

$$m = 2.5 \log flux + zp \tag{4.2}$$

where zp stands for zero point magnitude. The default zero point magnitude defined for the IRAF *imexam* task is $m_{zp,ime} = 25.00$. To derive the zero point magnitude for our observing instrument, we subtract $m_{std*,im}$ from $m_{std*,cat}$ and add the result to the default *imexam* zero point magnitude. Doing so, we obtain $m_{zp,inst} = 32.84$. To obtain the calibrated magnitude, we perform the following steps:

- measure the magnitude of the SN candidate in the signal to noise image (normalized difference image) - since the epoch image would contain the flux of the host galaxy as well;
- subtract $m_{zp,ime}$ from the result;
- add $m_{zp,inst}$to the difference.

Performing these three steps, with a magnitude of 15.04 measured for CL0303_SN1 in the S/N image, we determined its calibrated R-band magnitude to be $m_{SN1} = 22.84$.

4.3.2 Photometric Calibration for MS0451_SN2

Unlike in the case of CL0303_SN1, two standards stars from the frame *tw05.R113.1200.fits*, located at RAs and DECs of 04:54:25.5,-03:02:28.0 and 04:54:27.6,-030231.0 respectively were used in deriving the calibrated magnitude for MS0451_SN2, in order to increase accuracy of the result. We measured using *imexam* magnitudes of $m_{std*1,im} = 10.64$ for the first and $m_{std*2,im} = 11.00$ for the second standard stars. Their catalogued R-band magnitudes are $m_{std*1,cat} = 18.42$ and $m_{std*2,cat} = 18.82$. Following the same procedure as for CL0303_SN1, we subtract the average magnitude for the standard stars in the epoch frame from the average of their catalogued magnitudes and add the result to $m_{zp,ime}$ to obtain $m_{zp,inst} = 32.80$ for MS0451_SN2. We then measure the magnitude for

MS0451_SN2 in the S/N image[3], subtract $m_{zp,ime}$ from it and add to the difference the determined $m_{zp,inst}$ to obtain its calibrated magnitude. Doing so, we obtain a calibrated magnitude of $m_{SN2} = 27.74$ for MS0451_SN2.

Table 4.3 provides a summary of the photometric properties determined for CL0303_SN1 and MS0451_SN2. The values of $m_{std*,im}$ and $m_{std*,cat}$ given in the table for MS0451_SN2 are the average magnitudes for the two standard stars from the epoch frame and catalogue respectively.

Table 4.3: Summary of the photometric properties determined for the SN candidates CL0303_SN1 and MS0451_SN2.

Parameter	SN candidate	
	CL0303_SN1	MS0451_SN2
$m_{std,im}$	9.82	10.82
$m_{std,cat}$	17.66	18.62
$m_{zp,inst}$	32.84	32.80
Calibrated magnitude	22.84	27.74

4.4 Calculation of the Cluster SN Ia rate

As mentioned above, we use the SN candidates CL03034_SN1 and MS0451_SN2 to derive the cluster SN Ia rates for CL0303+17 and MS0451-03 respectively. To do this, we use the equation

$$SNu = \frac{N}{L_{tot}\epsilon T}, \tag{4.3}$$

where N is the total number of SNe Ia discovered, L_{tot} is the estimated total luminosity within 1 Mpc of the cluster centre, ϵ is the transient detection efficiency of the survey and T is the duration of the survey in years. We discuss the derivation of each of these quantities (with the exception of T) in detail.

4.4.1 Total number N of SNe Ia discovered

As has been stated above, we have no spectroscopic data to confirm whether or not our discovered SN candidates are SNe Ia. Colour index measurements of the candidates to determine their colour information to assist in typing them is beyond the scope of this thesis and reserved for future work. In the absence of such information, we attempt to derive the value of N by looking at similar exercises in the literature that have been conducted at similar redshifts as those for CL0303+17 and MS0451. The idea is to

[3] This was measured in the S/N frame produced with the automated algorithm. Attempts to measure the SN candidate's magnitude in the frame *sntw05.R113.1200.R186.1001.fits* that it was originally detected in with the IRAF algorithm returned an "INDEF" error.

determine the ratio of SNe Ia to the total number of SNe of all types discovered in the exercise, and then apply such a ratio to our discovered SN candidates to estimate the number of SN Ia events.

One such exercise is by Graham et al. (2008), carried out in the redshift range $0.2 < z < 1.0$, where they looked at quantifying the cluster SN Ia rate in this redshift bin using three cluster SNe Ia, i.e. $N = 3$, for a cluster search area of less than 1 Mpc radius (R $\sim$ 0.8 Mpc). Their study however did not report the total number of SNe of all types discovered within the specified search area for all clusters considered, from which 3 were SNe Ia. We are therefore unable to use this information for our purpose. Additionally, Graham et al. (2008) drew their sample from the Supernova Legacy Survey (SNLS), which forms part of the Canadian-France-Hawaii Telescope Legacy Survey[4] (Astier et al. 2006). The SNLS covers a redshift range of $0 <$ z < 1.2 and discovered from mid-2003 up to July 2007, a total number of 3110 SNe of all types, out of which 374 were SNe Ia, all with spectroscopic confirmation (Perrett et al. 2010). The SNLS redshift range encompasses the redshift for our cluster of interest, but we are still unable to use this ratio as it is likely to produce a more biased result, since their total count includes both field and cluster SNe.

We instead turn to the study by Sharon et al. (2010) in which they found 5 spectroscopically confirmed cluster SN Ia events out of a total of 14 cluster SNe discovered in their survey. Their study considered clusters in the redshift range $0.5 < z < 0.9$, which only includes the redshift for MS0451 and not for CL0303+17, but gives us a more reasonable estimate of the distribution of SNe Ia at intermediate redshifts Sharon et al. found 7 possible cluster SN Ia candidates, two of which are hostless events. We however make a highly conservative assumption in our analysis to only consider spectroscopically confirmed SNe Ia and treat the non spectroscopically confirmed cases as non SN Ia events. Doing so, we have 5/14 for cluster SNe Ia to cluster non SNe Ia. We use this ratio to determine the number of cluster SN Ia candidates N for our two clusters.

Since we did not find SN candidates in the rest of the clusters with the ISIS pipeline, their values for N is set to zero. We nonetheless derive upper limits on the value of $N = 0$ for each of these clusters (see Appendix A).

4.4.2 Total Luminosity L_{tot} within the Cluster search area

To estimate the value of L_{tot} within the search areas for CL0303+17 and MS0451, we make use of the Schechter luminosity function (LF), which gives a relation between the number of galaxies $\Phi(L)dL$ per unit volume in megaparsecs to the luminosity interval L and $L + dL$, expressed in mathematical form as

[4] http://www.cfht.hawaii.edu/Science/CFHLS/

$$\Phi(L)dL = \Phi_* \left(\frac{L}{L_*}\right)^{\alpha} \exp\left(\frac{-L}{L_*}\right) \frac{\Delta L}{L_*} \tag{4.4}$$

where L_*, known as the break luminosity, is the luminosity at which the low and high luminosity parts of the LF are separated (also known as the knee), Φ_* is the amplitude of the LF defined at L_*, known as the normalization parameter and has units of Mpc^{-3} and α is the slope of the lower luminosity or faint end of the LF (see SG06, Chapter 1 for more details and plots of the functional form of the Schechter luminosity function).

Integrating (4.4) from zero to infinity provides an estimate of the total luminosity density within a given volume and for a search area defined by a volume of 1 Mpc radius, we obtain a formulation for L_{tot} as

$$L_{tot} = \int_0^{\infty} L\Phi(L)dL \times V_{1Mpc} = \Phi_* L_* \Gamma(\alpha + 2) \times V_{1Mpc} \tag{4.5}$$

Computing the individual luminosities of the member galaxies within 1 Mpc of the cluster and then add them up is the most accurate way of determining the value of L_{tot} for the individual clusters. Such an exercise however, as stated in the brief introduction to this Chapter, is beyond the scope of this thesis and reserved as future work. We instead make use of values provided in the literature for L_*, Φ_* and α that have been derived for clusters in our sample at a radius of 1 Mpc, to calculate their individual L_{tot} values. One set of such values are those by Crawford et al. (2009), given in Table 4.4 as $M_{*,B}$, Φ_* and α for four of the six clusters in our sample.

Table 4.4: Literature values for the Schechter function parameters derived by Crawford et al. (2009) for four of our clusters and Kaiser et al. (1998) for CL0303+17, along with their respective $\Gamma(\alpha + 2)$ values that we have determined.

Cluster	SN candidate					
	$M_{*,B}$	L_* ($10^9 L_\odot$)	$\Phi_{*,old}$ (10^{-3} Mpc^{-3})	Φ_* (Mpc^{-3})	α	$\Gamma(\alpha+2)$
CL0303	-	23.7	-	30.3	-1	1
MS0451	$-20.54^{+0.28}_{-0.28}$	$4.09^{+1.06}_{-1.06}$	$130.9^{+17.1}_{-21.9}$	$126.0^{+16.5}_{-21.1}$	$-0.22^{+0.24}_{-0.20}$	$0.93^{+0.17}_{-0.15}$
MS1054	$-21.30^{+0.30}_{-0.32}$	$8.24^{+2.28}_{-2.43}$	$100.0^{+25.0}_{-31.0}$	$96.2^{+24.1}_{-29.8}$	$-0.76^{+0.22}_{-0.20}$	$0.91^{+0.15}_{-0.14}$
CL0016	$-20.34^{+0.32}_{-0.34}$	$3.41^{+1.00}_{-1.07}$	$110.1^{+23.9}_{-23.1}$	$106.0^{+23.0}_{-22.2}$	$-0.58^{+0.16}_{-0.14}$	$0.89^{+0.11}_{-0.09}$
CL1604	$-22.28^{+1.24}_{-1.50}$	$2.03^{+0.23}_{-0.23}$	$16.4^{+1.40}_{-15.4}$	$15.8^{+1.35}_{-14.8}$	$-0.74^{+0.54}_{-0.70}$	$0.90^{+0.37}_{-0.48}$
A370	-	$4.09^{+1.06}_{-1.06}$	-	$126.0^{+16.5}_{-21.1}$	$-0.22^{+0.24}_{-0.20}$	$0.93^{+0.17}_{-0.15}$

A conversion from $M_{*,B}$ to L_* is required in determining the value L_{tot} for the four clusters from (4.5). To perform the conversion, we use the absolute magnitude-luminosity relation

$$M_{*,B} - M_{\odot,B} = -2.5 \log \frac{L_{*,B}}{L_{\odot,B}}, \tag{4.6}$$

where $M_{\odot,B} = 5.48$ mag, $L_{\odot,B} = 0.16L_{\odot}$[5]. The values for Φ_* by Crawford et al. (2009) referred to as $\Phi_{*,old}$ in Table 4.4 were derived by considering a cluster search volume of V = 4031 Mpc^{-3} obtained using the equation

$$V = 4\pi R^2 \Delta r, \tag{4.7}$$

where R = 1 Mpc and Δr represents a redshift band equivalent to 0.1 and centred on the cluster redshift, with a value of 320.8 Mpc. For MS0451, the endpoints of Δr are 0.49 and 0.59. Using this volume, we convert the $\Phi_{*,old}$ values to new values $\Phi_{*,new}$ (referred to as Φ_* in Table 4.4) using the relation

$$V_{1Mpc} \times \Phi_{*,new} = V_{\Delta r} \times \Phi_{*,old}, \tag{4.8}$$

where $V_{1Mpc} = \frac{4}{3}R^3$, with R = 1 Mpc. The conversion assumes that the number of galaxies within 1 Mpc of the cluster is much larger than those outside this radius, thus we ignore their count.

The Schechter function parameters for CL0303+17 given in Table 4.4 were derived by Kaiser et al. (1998), where their cluster search volume was defined by a radius of 3' shown in Figure 4.2. Using the distance scale given in Table 4.1 for this cluster, this corresponds to a radius of approximately 1 Mpc. Kaiser et al. (1998) considered early-type galaxies, where they selected a sample defined by I_{band} magnitudes brighter than $I = 23$ with colours in the range $1.9 < V - I < 2.4$. Figure 4.2 shows the spatial distribution of the early-type galaxy sample. We have determined the value of L_* shown in Table 4.4 for CL0303+17 from the quantities $L/L_* = 65.81$ and $h^2 L/L_{\odot} = 1.49\text{e+}12$ reported in their paper, using the cosmology assumed in this thesis ($H_0 = 70$ km s^{-1}) for the value of h.

We could not find the values for L_*, Φ_* and α in the literature for A370. Since the velocity dispersion for this cluster is nearly the same as that for MS0451-03 (Table 1.1), we expect the total stellar mass for A370 to be closest to that for MS0451-03, than to the rest of the clusters in our sample. On that basis, we assume the values of L_*, Φ_* and α for A370 to be the same as those for MS0451-03, despite the latter's total X-ray luminosity being an order of magnitude higher than that of the former (see Table 1.1).

Substitution of the relevant quantities from Table 4.4 into (4.5) yields the estimated L_{tot} values given in Table 4.8 for the six clusters in our sample. The errors on L_{tot} values for our cluster sample were calculated via propagation of errors of the Schechter function parameters from the literature, assuming a normal distribution. The said errors were not correlated. This might be the case for all parameters and more accurate errors could

[5] source: http://marc.sauvage.free.fr/astro_book/OPT_pages/the_sun.html

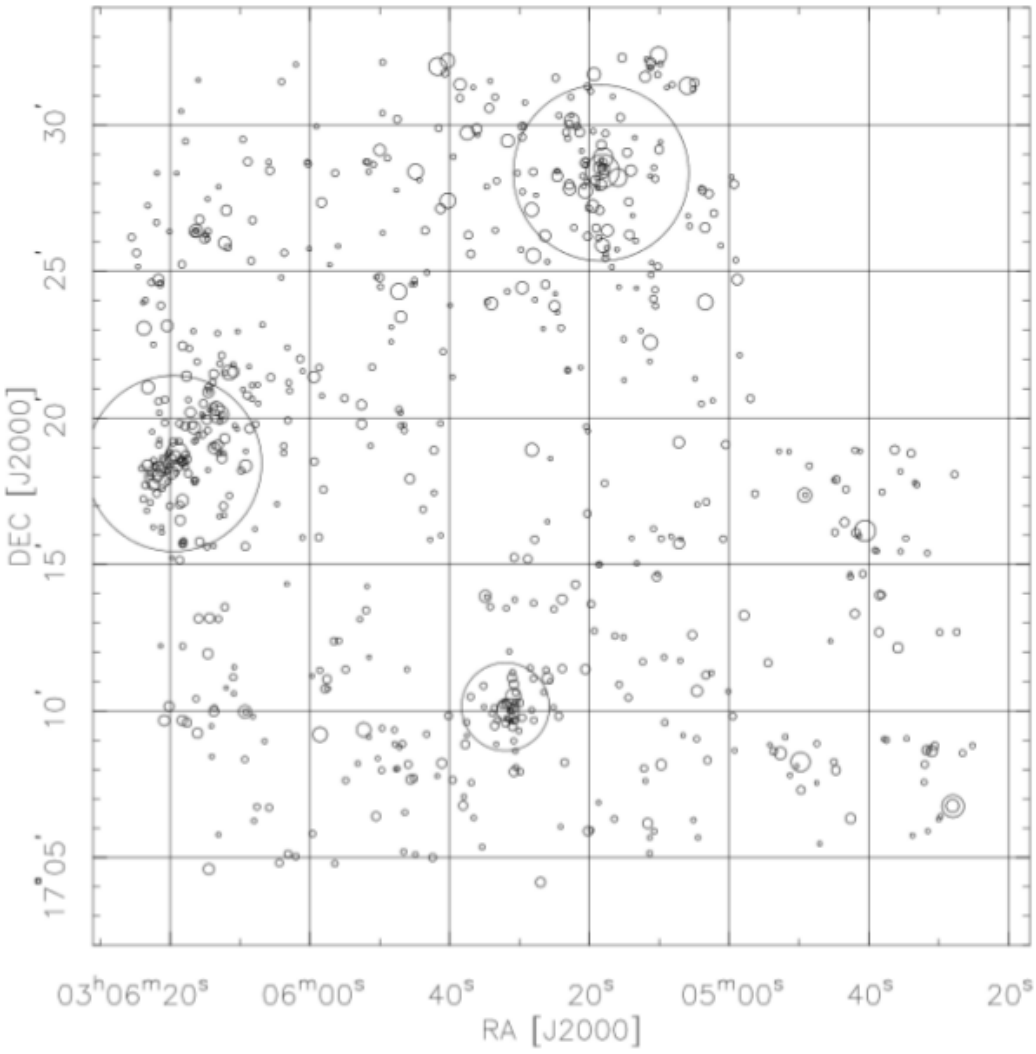

Figure 4.2: Spatial distribution of early type galaxies defined by a sample with a colour range $1.9 < V - I < 2.4$ and an I_{band} magnitude brighter than I= 23, at around the supercluster (MS0302+17) redshift of $z = 0.42$. CL0303+17 is located at the leftmost position, about halfway between the top and bottom of the figure, taken from Kaiser et al. (1998).

be calculated if the probability distributions for the fitted parameters were available. An example in this case was the negative error bar on the value of $L_{tot} = 1.21^{+1.47}_{-2.12}$ for CL1604, which obviously is incorrect, as it implies a negative lower limit on L_{tot} for the cluster.

4.4.3 Completeness Test and Transient Detection Efficiency ϵ

We performed a completeness test on our ISIS detection algorithm to ascertain the magnitude depth that it reaches in detecting transients. We did not do this for the IRAF algorithm. The fact that the latter is not automated makes such an exercise very tricky.

We developed a script that inserted 10 fake SNe in the images and then ran the ISIS pipeline all over again, a hundred times (100 iterations). For each iteration, the

fake SNe were inserted in the images randomly and were assigned random magnitudes in the range 20 to 26 magnitudes. This was the range of magnitudes that we were most interested in testing the detection completeness on. We did not expect any detection incompleteness at magnitudes of $m < 20$, as these were bright enough to be detected and the results shown in Figure 4.3 support this claim. The cluster chosen for this exercise was MS0451-03, which has a total number of 14 frames. The results were binned into 24 bins of magnitude with bin widths of 0.25 magnitudes. Figure 4.3 shows a histogram of the results obtained.

We observe in Figure 4.3 a detection completeness of between 80 - 100% in the magnitude range 20.0 to 23.1. The detection completeness falls below 50% between the central bin magnitudes of 23.4 and 23.6. We define the detection limit for our study to be the magnitude corresponding to a detection completeness of 50% and thus take the average of the two central bin magnitudes that the detection completeness falls below 50% in to approximate the detection limiting magnitude for our exercise, i.e. $m_{limit} = 23.5$

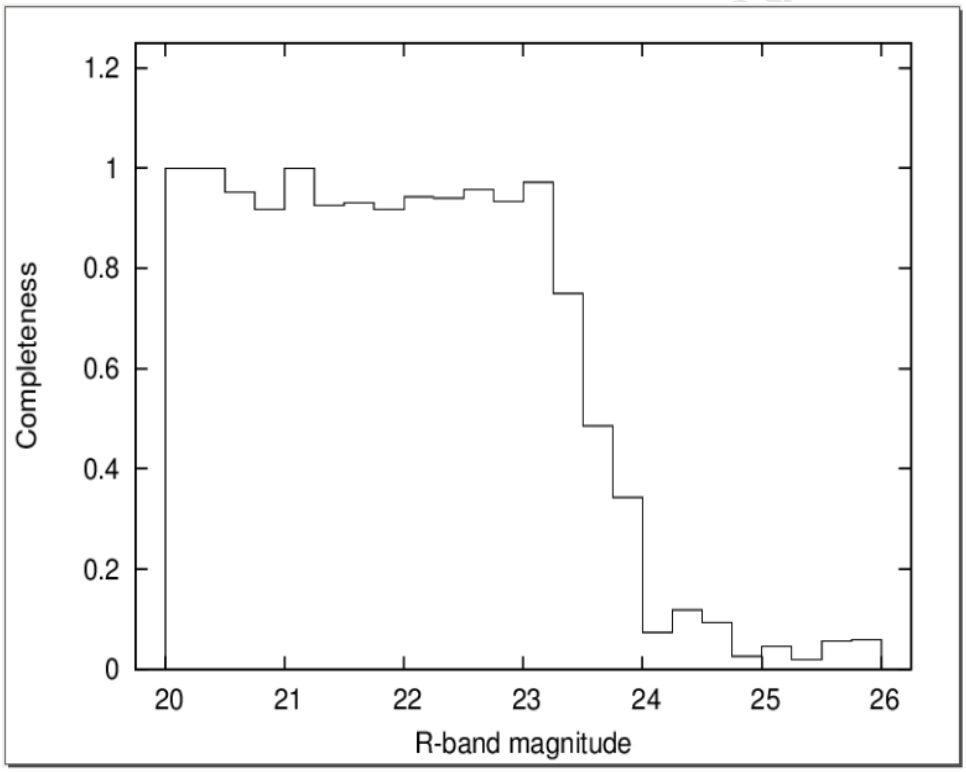

Figure 4.3: Completeness test for the automated transient detection method used in this work, using the 14 image frames for the cluster MS0451-03.

Using this magnitude limit, we derive its corresponding blue band absolute magnitude $M_{B,limit}$ at the various redshifts for our cluster sample. The aim of this calculation is to determine the control or visibility time (the length of time during which a SN is above the detection limit). To do this, we make use of the distance modulus equation similar to (1.2)

$$m_{limit} - M_{B,limit} = 5\log \mathrm{D}_L + 25 + K(z), \tag{4.9}$$

where D_L (introduced in section 4.1) is the luminosity distance to an object and the redshift dependent quantity $K(z)$ is called "$K-$correction". We discuss the $K-$correction concept in more detail below prior to determining the $M_{B,limit}$ values. For simplicity, we will denote $M_{B,limit}$ just by M_B.

4.4.3.1 K-Correction

$K-$correction refers to the correction made to observed magnitudes of astronomical sources, when comparing their rest-frame magnitudes in a given photometric filter at various redshifts to the observed magnitudes in a given filter bandpass at redshift $z = 0$ (Kim et al. 1996, hereafter K96). It relates rest-frame absolute magnitudes measured in a given filter at a particular redshift to the apparent magnitude measured for the same object in the same or different filter (Hogg et al. 2002). For a comparison made in the same filter, $K-$correction is expressed in mathematical form as

$$K_x = 2.5\log(1+z) + 2.5\log\left(\frac{\int(F(\lambda)S_x(\lambda)d\lambda)}{\int(F(\lambda/(1+z))S_x(\lambda)d\lambda)}\right), \tag{4.10}$$

where $F(\lambda)$ and $S_x(\lambda)$ are the spectral energy distribution (SED) and the x'th filter transmission respectively (K96). The general expression for dealing with more than one filter is slightly different from (4.10) and has the form

$$K_{xy} = K_x^{S_{x,den}\rightarrow S_y} - 2.5\log\left(\frac{\int(\mathcal{F}(\lambda)S_x(\lambda)d\lambda)}{\int(\mathcal{F}(\lambda)S_y(\lambda)d\lambda)}\right), \tag{4.11}$$

adapted from K96, where $\mathcal{F}(\lambda)$ represents an idealized stellar SED at redshift zero, for which the filters U,B,V,R,I are all equal to zero; and $K_x^{S_{x,den}\rightarrow S_y}$ denotes (4.10) with S_x in the denominator replaced by S_y. The subscripts x and y represent an unknown x and y filter pair, which could be a pair from the Johnson-Cousins $UBVRI$ filters.

To compute the M_B values from (4.9), we make use of the generalized $K-$correction values given in Table 2 of K96, which were derived using (4.11) from a sample of 29 rest frame spectra of three SNe Ia: SN 1981B; SN 1990N and SN 1992A, with epochs $-14 < t^B_{max} < 76$ after blue maximum light. K96 made a comparison at redshift $z = 0.5$ of the $K-$corrections K_{BR} and K_{VR} calculated from (4.11) using the filter pairs BR and and VR respectively, for the three SNe Ia. K_{VR} was found to show more scatter than K_{BR} at this redshift, in the plots for $K-$correction versus epoch shown in Figures 4.4 and 4.5.

K96 found that for redshift ranges $z < 0.1$, $0.1 < z < 0.35$ and $0.35 < z < 0.7$, the filter pairs that returned minimal scatter in the calculation of $K-$corrections using

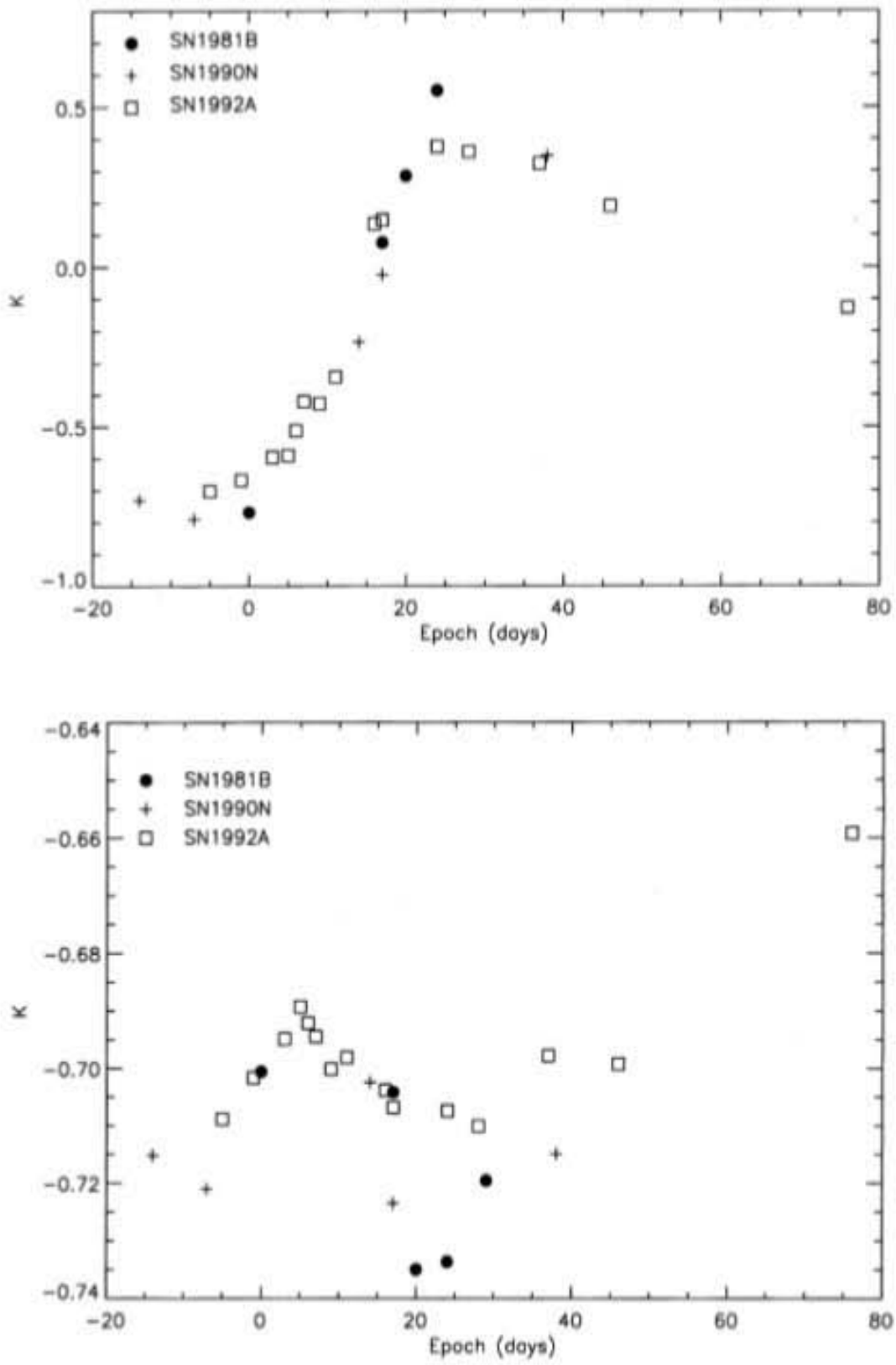

Figure 4.4: $K-$corrections K_{VR} (top panel) and K_{BR} (bottom panel) as a function of epoch determined at $z = 0.5$ for the SNe Ia: SN 1981B, SN 1990N and SN 1992A. It is clearly visible that the top panel has more scatter than the bottom panel, suggesting that $K-$correction estimates at redshift $z = 0.5$ produce less errors with the BR filter pair than with the VR filter. Figure from K96.

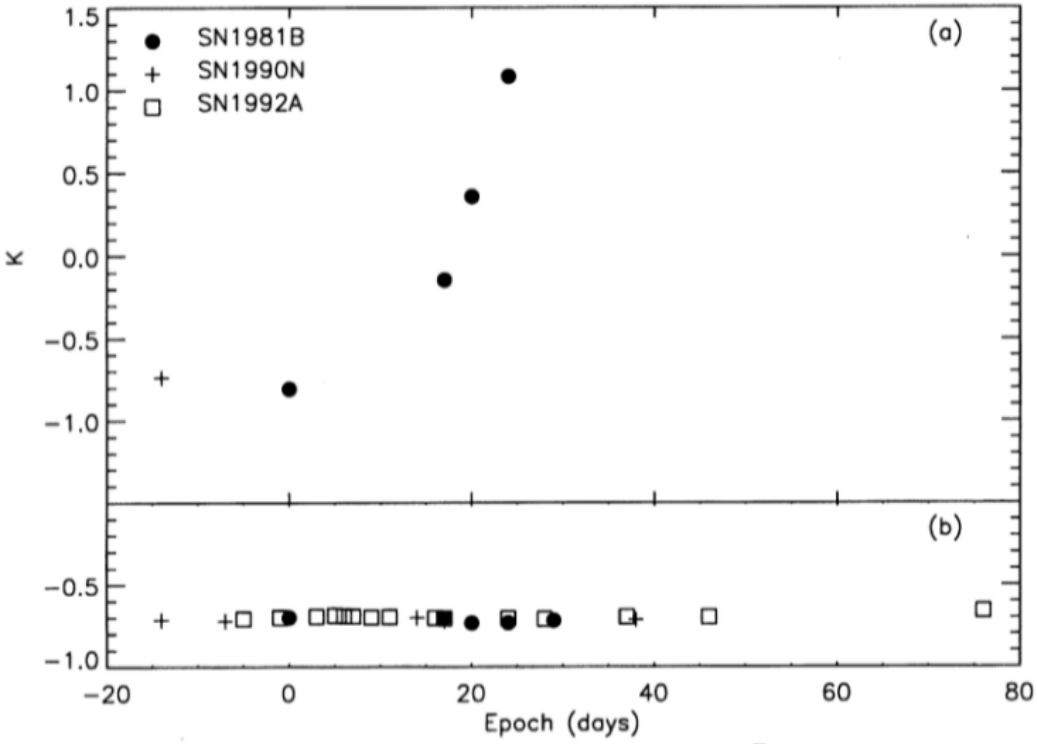

Figure 4.5: $K-$corrections K_{RR} (a) and K_{BR} (b) as a function of epoch determined at $z = 0.5$ for the SNe Ia: SN 1981B, SN 1990N and SN 1992A. The much smaller range for K_{BR} at this redshift is clearly visible. SN 1992A had insufficient spectral coverage in the R-band at this redshift, thus not visible in (a). Figure from K96.

(4.11) are RR, VR, and BR respectively. Since our cluster sample falls in the range $0.37 < z < 0.9$, we thus use $K-$corrections given by the filter pair BR (K_{BR}) to determine the values of M_B in (4.9). These $K-$corrections are obtained by adding up all K_{BR} values from Table 2 of K96 falling within the epoch range $-14 \leq t^B_{max} < 24$ days and associated with a redshift that corresponds or is closest to that of a given cluster in our sample, and then take the average.

We have selected the epoch range $-14 \leq t^B_{max} < 24$ days to ensure that the determined ranges of SN Ia visibility times (discussed in detail below) for our cluster sample - illustrated in Figures 4.6 and 4.7 - are contained within this epoch range.

Two of our clusters, MS1054 and CL1604 are located at redshifts beyond $z = 0.7$. Consequently, we assign to these two clusters $K-$correction values corresponding to $z = 0.7$, since beyond this redshift, R-band observations translate into rest-frame UV band, which hardly gets observed. Thus $z = 0.7$ provides somewhat a limit to the degree of $K-$correction we can apply to our R-band observations.

CL0016 is located at redshift 0.54, which is not found in Table 2 of K96. We utilise the values derived for $z = 0.5$, as this is the closest redshift to it. Table 4.5 provides the averaged $K-$correction values at the various cluster redshifts and the luminosity distance

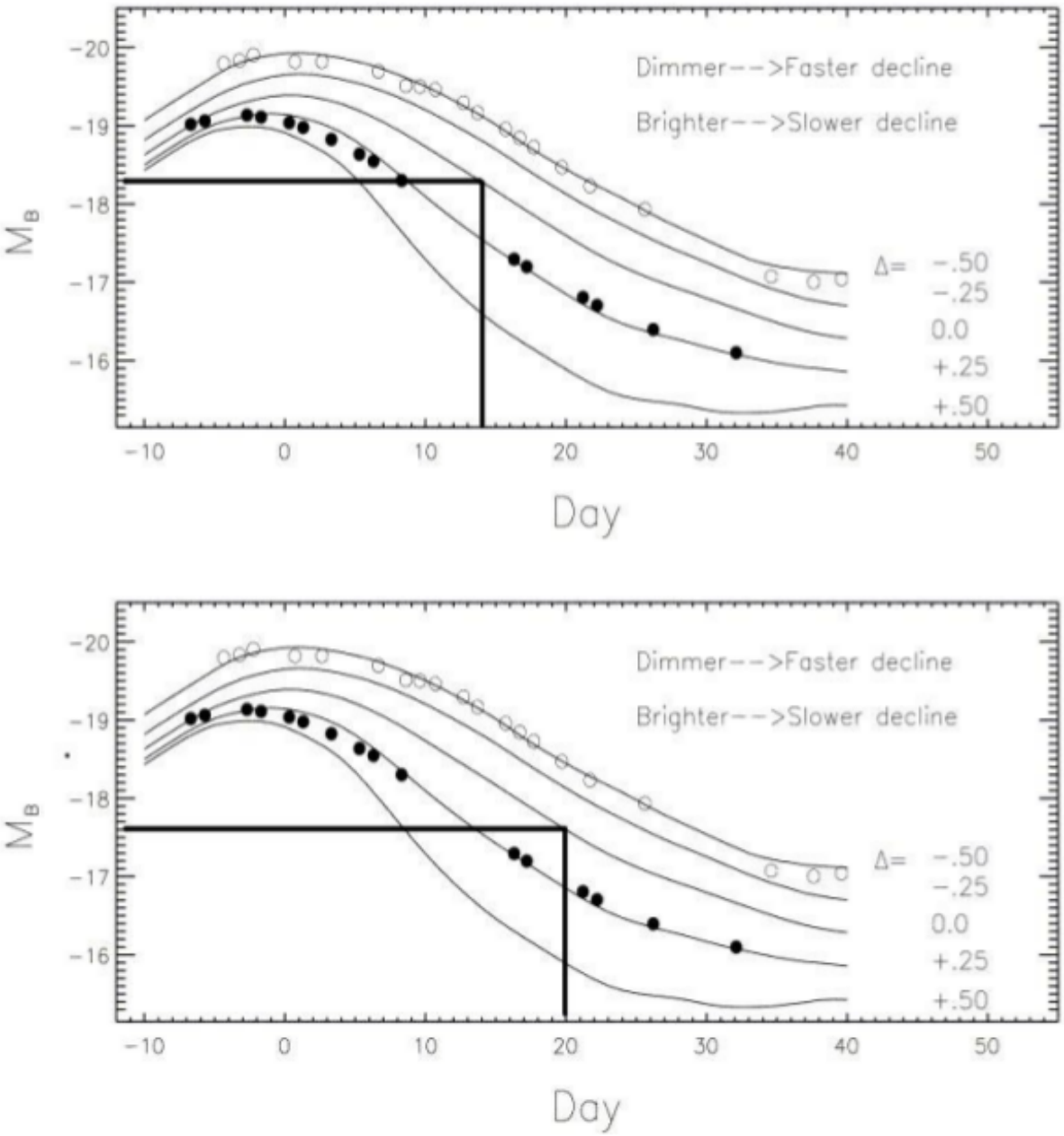

Figure 4.6: B-band SN Ia family light curves, depicting photometric differences between brighter and dimmer SNe Ia. The visibility times are estimated from the $\Delta = 0$ ($\Delta = M_V - M_{V,standard}$) light curve, using the straight horizontal and vertical black lines at their point of intersection on the curve. These are 24 days for MS0451_SN2 (top panel) and 30 days for CL0303_SN1 (bottom panel). Examples of a brighter and dimmer SN Ia are "SN 1995ac" and SN 1996X, over-plotted with open and filled circles respectively. Figure from Riess et al. (1998).

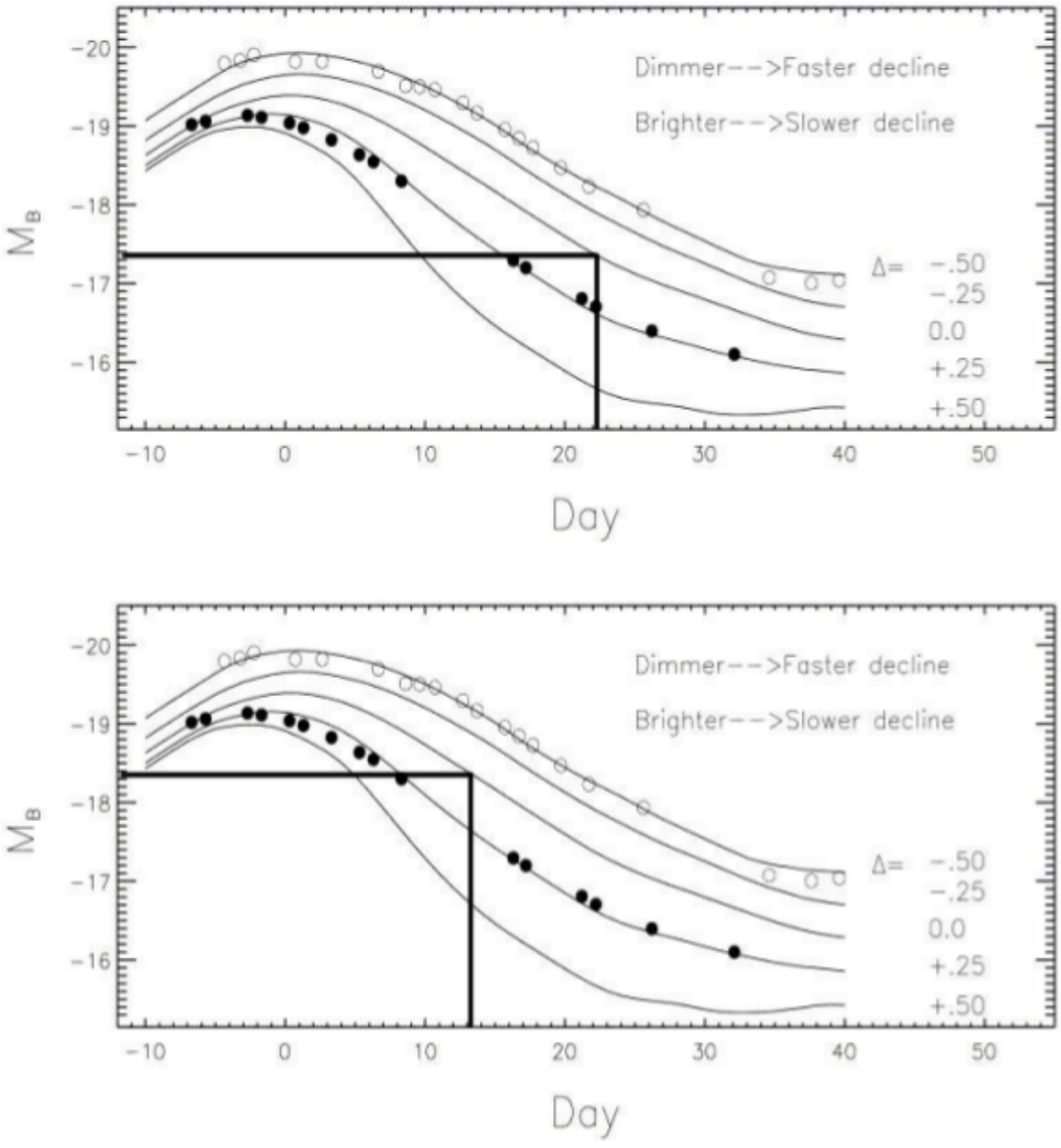

Figure 4.7: Same as Figure 4.6, except for visibility times of approximately 32 and 23 days for A370 (top panel) and CL0016+16 (bottom panel) respectively.

D_L values determined above for our cluster sample. We combine the two quantities with our exercise's determined limiting magnitude m_{limit} to compute from (4.9) the values of M_B also shown in Table 4.5, for our cluster sample.

Table 4.5: Average $K-$correction, D_L and M_B values determined from Table 2 of K96, the NED cosmology calculator and the distance modulus equation (4.9) respectively, for our cluster sample.

	SN candidate					
Parameter	MS0451	MS1054	CL0016	CL1604	A370	CL0303
z	0.54	0.83	0.55	0.90	0.37	0.42
D_L (Mpc)	3107.6	5249.9	3177.1	5800.9	1981.7	2301.1
Average $K-$correction	-0.649	-0.431	-0.649	-0.431	-0.634	-0.688
M_B	-18.31	-19.89	-18.36	-19.89	-17.35	-17.62

Figure 4.6 illustrates SNe Ia light curves with the indicated luminosity corrections Δ that we use to determine the SN Ia visibility times for our cluster sample. Δ is defined as the difference between the measured absolute V-band magnitude and the absolute V-band magnitude for a SN Ia of standard brightness and light curve shape, i.e. $\Delta = M_V - M_{V,standard}$ (Riess et al. 1996). Assuming our SN candidates to be standard SNe Ia, we use the light curve corresponding to the luminosity correction $\Delta = 0$ in conjunction with the determined M_B values in Table 4.5 to estimate the visibility times of SNe Ia at the cluster redshifts, using the thick horizontal and vertical black lines drawn on the plots. Doing so, we find visibility times of 24 days and 30 days for MS0451_SN2 and CL0303_SN1 respectively.

Notwithstanding a zero detection of SN candidates in the rest of the clusters, we have also made an indication of the visibility time that we would have expected from SNe Ia observed in such clusters, assuming them to be standard SNe Ia. Figures 4.7 and 4.8 illustrates this indication, from which we have determined visibility times of ~ 32 and 23 days for A370 and CL0016 respectively in Figure 4.7; and zero visibility for both MS1054 and CL1604 in Figure 4.8, owing to the higher M_B detection limits at these cluster redshifts. For this reason, we exclude these two clusters from further analysis in this thesis.

Table 4.6 is a reduced version of Table 2.1 to include the earliest detection dates of (potential) SN Ia candidates for the clusters that we determined visibility times for. The earliest detection dates are obtained by subtracting the determined visibility times from the frame observation dates. The total number of days for the frame ID *tw03.1100* is given as 30 days and not 32 as with the rest, due to the fact that its observational window stretching from the date of observation to its earliest detection date overlaps with that for *tw03.1000* by two days, hence the two days reduction.

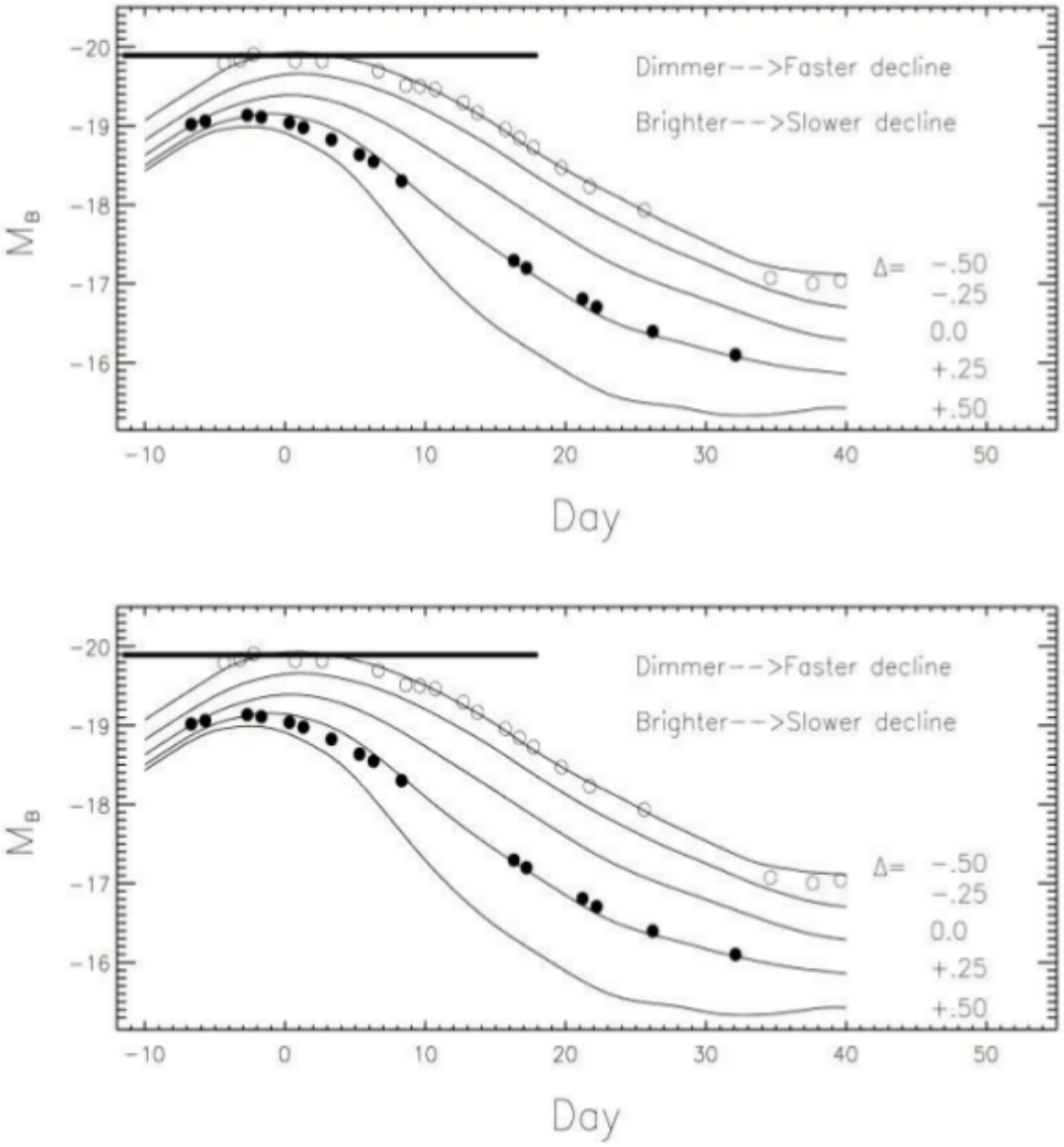

Figure 4.8: Same as Figure 4.6, except zero visibility, as the black horizontal lines show, for both MS1054-03 (top panel) and CL1604+4304 (bottom panel), due to the higher M_B detection limits at the redshifts of the two clusters.

Table 4.6: R-band observation dates, earliest SN detection dates and visibility times for four of our cluster sample.

Cluster	Image ID	Date of observation	Earliest SN detection date	Total number of days (dt)
A370	tw03.1299	15-12-1999	13-11-1999	32
A370	tw03.1000	15-10-2000	13-09-2000	32
A370	tw03.1100	15-11-2000	14-10-2000	30
A370	tw03.1001	18-10-2001	16-09-2001	32
A370	tw03.1202	06-12-2002	01-11-2002	32
CL0016+16	tw01.1099	15-10-1999	23-09-1999	23
CL0016+16	tw01.1299	15-12-1999	23-11-1999	23
CL0016+16	tw01.1200	15-12-2000	23-11-2000	23
CL0016+16	tw01.1001	18-10-2001	26-09-2001	23
CL0016+16	tw01.0902	12-09-2002	20-08-2002	23
CL0016+16	tw01.0904	15-09-2004	23-08-2004	23
MS0451-03	tw05.1099	14-10-1999	20-09-1999	24
MS0451-03	tw05.1299	15-12-1999	21-11-1999	24
MS0451-03	tw05.1100	18-11-2000	25-10-2000	24
MS0451-03	tw05.1200	26-12-2000	02-12-2000	24
MS0451-03	tw05.1001	15-10-2001	21-09-2001	24
MS0451-03	tw05.1101	09-11-2001	16-10-2001	24
MS0451-03	tw05.1004	06-10-2004	12-09-2004	24
CL0303+17	tw04.1099	16-10-1999	17-09-1999	30
CL0303+17	tw04.1100	15-11-2000	17-10-2000	30
CL0303+17	tw04.1200	15-12-2000	16-11-2000	30
CL0303+17	tw04.1001	16-10-2001	17-09-2001	30
CL0303+17	tw04.1202	06-12-2002	07-11-2002	30
CL0303+17	tw04.0904	15-09-2004	16-08-2004	30
CL0303+17	tw04.1004	06-10-2004	07-09-2004	30

The detection efficiency for our survey is defined as

$$\epsilon = \frac{\Sigma dt}{dT}, \tag{4.12}$$

where Σdt is total number of days given in column 5 of Table 4.6 for a given set of cluster frames, and dT represent the number of days that have lapsed between the start and end of the survey or the last observation date for a given cluster. Table 4.7 provides a summary of the determined visibility times, Σdt, dT and T (dT expressed in years) for our cluster sample.

Table 4.7: Summary of visibility times, Σdt, dT derived for four of our cluster sample.

	Cluster			
Parameter	MS0451	CL0303	A370	CL0016
Visibility				
Time (days)	24	30	32	23
Σdt	168	210	158	138
dT	1819	1817	1086	1796

Since our SN candidates MS045_SN2 and CL0303_SN1 were assigned their cluster's redshifts, the parameters in Table 4.7 derived for the clusters MS0451-03 and CL0303+17 also apply to them.

4.4.4 The SN Ia rate for clusters in our sample

We have determined all the quantities required in (4.3) to derive the cluster SN Ia rates for our sample. Table 4.8 provides the number of SN Ia candidates N, total luminosities L_{tot}, detection efficiencies ϵ as well as duration of the survey T for each cluster, from which the shown cluster SN Ia rates have been derived.

Table 4.8: The four parameters: N, L_{tot}, ϵ and T determined for the remaining four clusters of our sample and cluster SN Ia rates derived from them.

	Cluster			
Parameter	MS0451	CL0303	A370	CL0016
N	$0.36^{+0.84}_{-0.34}$	$0.36^{+0.84}_{-0.34}$	$0^{+1.83}_{-0.00}$	$0^{+1.83}_{-0.00}$
L_{tot} ($10^{12} L_{\odot,B}$)	$2.00^{+0.69}_{-0.69}$	$3.00^{+0.69}_{-0.69}$	$2.00^{+0.69}_{-0.69}$	$1.35^{+0.52}_{-0.53}$
ϵ	0.092	0.016	0.145	0.077
T (years)	4.98	4.97	2.98	4.92
$SNuB$				
(100 years $10^{10} L_{\odot,B}$)$^{-1}$	$0.39^{+0.91}_{-0.39}$	$0.21^{+0.48}_{-0.20}$	$0^{+0.93}_{-0.00}$	$0^{+0.75}_{-0.00}$

We remind the reader that this derivation was based on the assumption that all our cluster frames have same magnitude limit of $m_{limit} = 23.5$. Also, as can be seen from Table 4.4, Kaiser et al. (1998) did not include error bars on their derivation of L_* and

Φ_* and they assumed a value of -1 for α. Our search in the literature for an indication of error bars on the Schechter function parameters for CL0303+17 proved futile. We have therefore crudely assumed the error bars on L_{tot} for CL0303+17 to be the same as those derived for MS0451.

4.4.5 Comparison of results to literature

Figure 4.9 shows a plot of the previous cluster SN Ia rates at various redshifts and the rates we have derived for MS0451-03 and CL0303+17 (black filled squares), which both appear to be consistent with the previous measurements. Also shown in Figure 4.9 are the upper limits (the two downward pointing arrows) we have derived for the two clusters A370 and CL0016+16, both with zero SN Ia rates, as Table 4.8 shows.

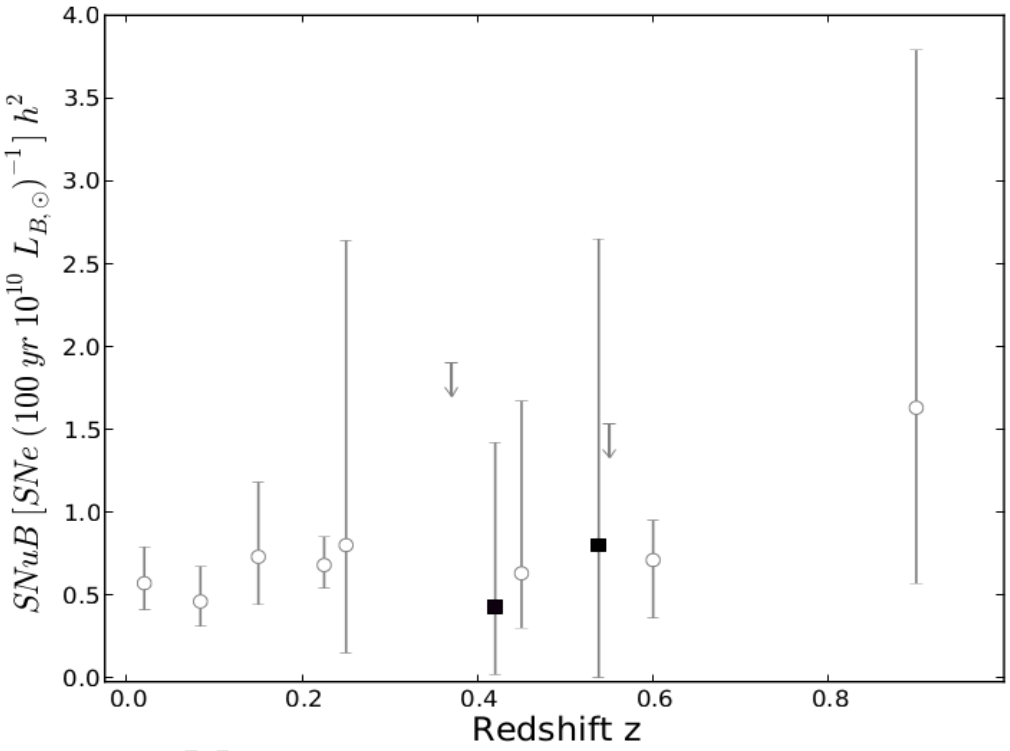

Figure 4.9: Our two cluster SN Ia rates determined for CL0303+17 and MS0451-03 (black squares) at redshifts $z = 0.42$ and $z = 0.54$ respectively, plotted against cluster SN Ia rates from the literature. The indicated SN Ia rates were derived in order of increasing redshift by Mannucci et al. (2008), Dilday et al. (2010), Sharon et al. (2007), Dilday et al. (2010), Gal-Yam et al. (2002), Graham et al. (2008), Sharon et al. (2010) and Gal-Yam et al. (2002). The vertical error bars represent the 68.27% confidence interval. The two arrows plotted at redshifts z = 0.37 and z = 0.55 for A370 and CL0016+16 respectively, mark the upper limits derived on the zero cluster SN Ia rates for the two clusters, as shown in Table 4.8.

As mentioned in sub-section 3.3.2, we emphasize that the SN candidate MS0451_SN2 was detected with the IRAF algorithm at a lower detection threshold defined by a SNR of < 3, whereas the rest of the clusters were searched for transients with the ISIS pipeline using a detection threshold of SNR = 5. At a detection threshold of SNR < 3, only the foreground SN candidate "MS0451_SN1" would have been detected in MS0451 with the

ISIS pipeline.

Both our results fall within the 68% confidence intervals of the results derived by Graham et al. (2008) and Sharon et al. (2010) at intermediate redshifts. Graham et al. (2008) derived a rate of SNuB$h^2 = 0.63^{+1.04}_{-0.33}h2$ at a mean redshift of $z = 0.45$ (reported by Dilday et al. 2010), which translates into $0.31^{+0.51}_{-0.16}$ SNuB, using the cosmology assumed in this thesis for the value of h. Our result for CL0303+17 of $0.21^{+0.48}_{-0.20}$ SNuB falls within the 68% confidence interval of that result, albeit derived at redshift $z = 0.42$.

In spite of the large positive error bar, the rate we have derived for MS0451-03 of $0.39^{+0.91}_{-0.39}$ SNuB is also consistent with the result by Sharon et al. (2010) of $0.35^{+0.17}_{-0.12}$ SNuB at a mean redshift of $z = 0.6$. Many of the cluster rates derived at lower redshifts, as shown in Figure 4.9, also appear to be in good agreement with the rates we have derived for the two clusters.

Small number statistics is the dominant cause of uncertainties reported in our analysis. This is something that remains a general challenge in measurements of cluster SN Ia rates at intermediate redshifts due to unavailability of more observational data within the redshift range $0.3 < z < 0.9$, just as encountered by Graham et al. (2008) and Sharon et al. (2010).

Chapter 5

Conclusion and Future Work

We searched for transient events in six galaxy clusters located in the redshift range $0.3 < z < 0.9$ in order to quantify the frequency of cluster SN Ia events in this redshift range. To do this, we performed image subtraction of the cluster images using two transient search algorithms: The IRAF Image Subtraction Algorithm and ISIS Automated Image Subtraction Algorithm. The IRAF algorithm was only utilised for one cluster, MS0451-03 and the rest of the clusters were searched for transients with the automated algorithm, which underwent a number of modifications to suit our data sample.

A number of transients were discovered in the search, including AGN candidates, asteroids and SN candidates. Out of the four SN candidates we found, only two were located within 1 Mpc of their clusters, which defined our cluster transient search area. The two clusters in which these candidates were found individually are MS0451-03 and CL0303+17.

We neither had spectroscopic nor photometric redshifts of the SN candidates, so we assumed their redshifts to be their cluster redshifts. Also, we were not in the position to type the two SN candidates. Instead we made use of the ratio of confirmed cluster SN Ia events to cluster core-collapse and unconfirmed SN Ia events from a study by Sharon et al. 2010, to convert each SN candidate into a number of SN Ia cluster events. After determining total luminosities within 1 Mpc of the two clusters and the survey detection efficiencies, we derived cluster SN Ia rates of $0.39^{+0.91}_{-0.39}$ SNuB and $0.21^{+0.48}_{-0.20}$ SNuB for MS0451-03 and CL0303+17 respectively, where SNuB is defined as SNe per 100 years per $10^{10} L_{\odot,B}$.

Our study happens to be the third study to probe the redshift interval $0.3 < z < 0.9$, in an effort to measure the rate of SN Ia events in clusters, with the other two studies being by Graham et al. (2008) and Sharon et al. (2010), which probed the ranges $0.2 < z < 0.6$ and $0.5 < z < 0.9$ respectively.

This thesis is the first attempt to make use of the WLTV Survey data to measure SN Ia rates in galaxy clusters in the redshift interval $0.3 < z < 0.9$. We therefore intend to

refine the methods employed into this first attempt in the future to improve the accuracy of our results. The following includes but not limited to, areas of future work that we have identified to improve our current methods in constraining cluster SN Ia rates:

- Combine the data from individual epochs to increase our observing depth. This has a potential of revealing more supernovae/transients candidates falling below the current detection limit of our survey.

- Derivation of photometric redshifts for the discovered SN candidates and their host galaxies, in the absence of spectroscopic data. As has been stated, we assumed the redshifts of both SN candidates to be those of their clusters. Such an approach introduces unwanted uncertainties that could be minimized with the use of photometric redshifts of the candidates or their host galaxies.

- Aperture photometry of the individual galaxies within the search area to derive the Schechter luminosity function parameters L_*, Φ_* and α specific to the data in our study sample. We have adopted in Chapter 4, the Schechter function parameters derived by Crawford et al. (2009) and Kaiser et al. (1998) to compute the total luminosity within our defined cluster search area for MS0451-03 and CL0303+17 respectively.

- Expand the exercise to include the remainder of the clusters in the WLTV sample to give a total sample of about ten galaxy clusters and also perform measurements in other pass-bands (B and I filters).

In addition to the above, we also intend to use our measured cluster SN Ia rates to constrain the star formation histories of cluster galaxies and the metal enrichment of the ICM by constraining the delay time distribution of SNe Ia. Both topics remain poorly understood (B12b, Sand et al. 2012) and are among the most focused areas of research in supernova cosmology. We also hope to contribute in the future to the quest for understanding the physics of the progenitor scenarios of SNe Ia, which to this day is also not well understood. Other future work plans include using the Southern African Large Telescope (SALT) to monitor the clusters used in this thesis to expand our data set, repeat the measurements with the expanded data set to reduce inaccuracies in the results introduced by low number statistics.

Bibliography

Abdelsalam, H. M. 1998, MNRAS, 746, 734

Alard, C. 2000, A&AS, 144, 363

Alard, C. & Lupton, R. H. 1998, ApJ, 503, 325

Amanullah, R., Lidman, C., Rubin, D., Aldering, G., Astier, P., Barbary, K., Burns, M. S., Conley, a., Dawson, K. S., Deustua, S. E., Doi, M., Fabbro, S., Faccioli, L., Fakhouri, H. K., Folatelli, G., Fruchter, a. S., Furusawa, H., Garavini, G., Goldhaber, G., Goobar, a., Groom, D. E., Hook, I., Howell, D. a., Kashikawa, N., Kim, a. G., Knop, R. a., Kowalski, M., Linder, E., Meyers, J., Morokuma, T., Nobili, S., Nordin, J., Nugent, P. E., Östman, L., Pain, R., Panagia, N., Perlmutter, S., Raux, J., Ruiz-Lapuente, P., Spadafora, a. L., Strovink, M., Suzuki, N., Wang, L., Wood-Vasey, W. M., & Yasuda, N. 2010, The Astrophysical Journal, 716, 712

Anderson, J. P., Habergham, S. M., James, P. A., & Hamuy, M. 2012, MNRAS, 424, 1372

Astier, P., Guy, J., Regnault, N., Pain, R., Aubourg, E., Balam, D., Basa, S., Carlberg, R. G., Fabbro, S., Fouchez, D., Hook, I. M., Howell, D. A., Lafoux, H., Neill, J. D., Palanque-Delabrouille, N., Perrett, K., Pritchet, C. J., Rich, J., Sullivan, M., Taillet, R., Aldering, G., Antilogus, P., Arsenijevic, V., Balland, C., Baumont, S., Bronder, J., Courtois, H., Ellis, R. S., Filiol, M., Gonçalves, A. C., Goobar, A., Guide, D., Hardin, D., Lusset, V., Lidman, C., McMahon, R., Mouchet, M., Mourao, A., Perlmutter, S., Ripoche, P., Tao, C., & Walton, N. 2006, A&A, 447, 31

Barbary, K., Aldering, G., Amanullah, R., Brodwin, M., Connolly, N., Dawson, K. S., Doi, M., Eisenhardt, P., Faccioli, L., Fadeyev, V., Fakhouri, H. K., Fruchter, A. S., Gilbank, D. G., Gladders, M. D., Goldhaber, G., Goobar, A., Hattori, T., Hsiao, E., Huang, X., Ihara, Y., Kashikawa, N., Koester, B., Konishi, K., Kowalski, M., Lidman, C., Lubin, L., Meyers, J., Morokuma, T., Oda, T., Panagia, N., Perlmutter, S., Postman, M., Ripoche, P., Rosati, P., Rubin, D., Schlegel, D. J., Spadafora, A. L., Stanford, S. A., Strovink, M., Suzuki, N., Takanashi, N., Tokita, K., Yasuda, N., & Supernova Cosmology Project. 2012, ApJ, 745, 32

Barbon, R. 1978, AJ, 83, 13

Barris, B. J. & Tonry, J. L. 2006, ApJ, 637, 427

Bernardo, J. M. 1976, Royal Statistics Society. Series C (Applied Statistics), 25, 315

Blakeslee, J. P., Holden, B. P., Franx, M., Rosati, P., Bouwens, R. J., Demarco, R., Ford, H. C., Homeier, N. L., Illingworth, G. D., Jee, M. J., Mei, S., Menanteau, F., Meurer, G. R., Postman, M., & Tran, K.-V. H. 2006, ApJ, 644, 30

Branch, D. & Tammann, G. A. 1992, ARA&A, 30, 359

Brown, P. J., Roming, P. W. a., Milne, P., Bufano, F., Ciardullo, R., Elias-Rosa, N., Filippenko, A. V., Foley, R. J., Gehrels, N., Gronwall, C., Hicken, M., Holland, S. T., Hoversten, E. a., Immler, S., Kirshner, R. P., Li, W., Mazzali, P., Phillips, M. M., Pritchard, T., Still, M., Turatto, M., & Berk, D. V. 2010, ApJ, 721, 1608

Burrows, A., Livne, E., Dessart, L., Ott, C. D., & Murphy, J. 2007, ApJ, 655, 416

Cappellaro, E., Evans, R., & Turatto, M. 1999, A&A, 466, 459

Cappellaro, E. & Turatto, M. 2001, in Astrophysics and Space Science Library, Vol. 264, The Influence of Binaries on Stellar Population Studies, ed. D. Vanbeveren, 199

Carroll, B. W. & Ostlie, D. A. 2006, An introduction to modern astrophysics, Second edn.

Chevalier, R. A. & Soderberg, A. M. 2010, ApJ, 711, L40

Colgate, S. A. & McKee, C. 1969, ApJ, 157, 623

Connolly, A. J., Szalay, A. S., Koo, D., Romer, A. K., Holden, B., Nichol, R. C., & Miyaji, T. 1996, ApJ, 473, L67

Crane, P., Tammann, G. A., & Woltjer, L. 1977, Nature, 265, 124

Crawford, S. M. 2006, PhD thesis, The University of Wisconsin - Madison, Wisconsin, USA

Crawford, S. M., Bershady, M. A., Glenn, A. D., & Hoessel, J. G. 2006, ApJ, 636, L13

Crawford, S. M., Bershady, M. a., & Hoessel, J. G. 2009, The Astrophysical Journal, 690, 1158

Crawford, S. M., Wirth, G. D., Bershady, M. a., & Hon, K. 2011, The Astrophysical Journal, 741, 98

da Silva, L. A. L. 1993, Ap&SS, 202, 215

Dilday, B., Bassett, B., Becker, A., Bender, R., Castander, F., Cinabro, D., Frieman, J. a., Galbany, L., Garnavich, P., Goobar, A., Hopp, U., Ihara, Y., Jha, S. W., Kessler, R., Lampeitl, H., Marriner, J., Miquel, R., Mollá, M., Nichol, R. C., Nordin, J., Riess, A. G., Sako, M., Schneider, D. P., Smith, M., Sollerman, J., Wheeler, J. C., Östman, L., Bizyaev, D., Brewington, H., Malanushenko, E., Malanushenko, V., Oravetz, D., Pan, K., Simmons, A., & Snedden, S. 2010, The Astrophysical Journal, 715, 1021

Donahue, M. 1996, ApJ, 468, 79

Donahue, M., Gaskin, J. A., Patel, S. K., Joy, M., Clowe, D., & Hughes, J. P. 2003, ApJ, 598, 190

Dressler, A. & Gunn, J. E. 1992, ApJS, 78, 1

Ellingson, E., Yee, H. K. C., Abraham, R. G., Morris, S. L., & Carlberg, R. G. 1998, ApJS, 116, 247

Feldmeier, J. J., Ciardullo, R., & Jacoby, G. H. 1998, ApJ, 503, 109

Filippenko, A. V. 1988, Proceedings of the Astronomical Society of Australia, 7, 540

Filippenko, A. V. 1997, ARA&A, 35, 309

Förster, F., Wolf, C., Podsiadlowski, P., & Han, Z. 2006, MNRAS, 368, 1893

Gal-Yam, A., Maoz, D., Guhathakurta, P., & Filippenko, A. V. 2003, AJ, 125, 1087

Gal-Yam, A., Maoz, D., & Sharon, K. 2002, MNRAS, 332, 37

Geach, J. E., Ellis, R. S., Smail, I., Rawle, T. D., & Moran, S. M. 2011, MNRAS, 413, 177

Gehrels, N. 1986, ApJ, 303, 336

Goobar, A. & Perlmutter, S. 1995, ApJ, 450, 14

Goto, T., Postman, M., Cross, N. J. G., Illingworth, G. D., Tran, K., Magee, D., Franx, M., Benítez, N., Bouwens, R. J., Demarco, R., Ford, H. C., Homeier, N. L., Martel, A. R., Menanteau, F., Clampin, M., Hartig, G. F., Ardila, D. R., Bartko, F., Blakeslee, J. P., Bradley, L. D., Broadhurst, T. J., Brown, R. A., Burrows, C. J., Cheng, E. S., Feldman, P. D., Golimowski, D. A., Gronwall, C., Holden, B., Infante, L., Jee, M. J., Krist, J. E., Lesser, M. P., Mei, S., Meurer, G. R., Miley, G. K., Motta, V., Overzier, R., Sirianni, M., Sparks, W. B., Tran, H. D., Tsvetanov, Z. I., White, R. L., Zheng, W., & Zirm, A. 2005, ApJ, 621, 188

Graham, M. L., Pritchet, C. J., Sullivan, M., Gwyn, S. D. J., Neill, J. D., Hsiao, E. Y., Astier, P., Balam, D., Balland, C., Basa, S., Carlberg, R. G., Conley, a., Fouchez, D., Guy, J., Hardin, D., Hook, I. M., Howell, D. a., Pain, R., Perrett, K., Regnault, N., Baumont, S., Du, J. L., Lidman, C., Perlmutter, S., Ripoche, P., Suzuki, N., Walker, E. S., & Zhang, T. 2008, The Astronomical Journal, 135, 1343

Greggio, L. 2005, A&A, 1078, 1055

Groh, J. H., Meynet, G., & Ekström, S. 2013, A&A, 550, L7

Guy, J., Astier, P., Baumont, S., Hardin, D., Pain, R., Regnault, N., Basa, S., Carlberg, R. G., Conley, A., Fabbro, S., Fouchez, D., Hook, I. M., Howell, D. A., Perrett, K., Pritchet, C. J., Rich, J., Sullivan, M., Antilogus, P., Aubourg, E., Bazin, G., Bronder, J., Filiol, M., Palanque-Delabrouille, N., Ripoche, P., & Ruhlmann-Kleider, V. 2007, A&A, 466, 11

Guy, J., Astier, P., Nobili, S., Regnault, N., & Pain, R. 2005, A&A, 443, 781

Hamuy, M., Phillips, M. M., Suntzeff, N. B., Schommer, R. A., Maza, J., Antezan, A. R., Wischnjewsky, M., Valladares, G., Muena, C., Gonzales, L. E., Aviles, R., Wells, L. A., Smith, R. C., Navarrete, M., Covarrubias, R., Williger, G. M., Walker, A. R., Layden, A. C., Elias, J. H., Baldwin, J. A., Hernandez, M., Tirado, H., Ugarte, P., Elston, R., Saavedra, N., Barrientos, F., Costa, E., Lira, P., Ruiz, M. T., Anguita, C., Gomez, X., Ortiz, P., della Valle, M., Danziger, J., Storm, J., Kim, Y.-C., Bailyn, C., Rubenstein, E. P., Tucker, D., Cersosimo, S., Mendez, R. A., Siciliano, L., Sherry, W., Chaboyer, B., Koopmann, R. A., Geisler, D., Sarajedini, A., Dey, A., Tyson, N., Rich, R. M., Gal, R., Lamontagne, R., Caldwell, N., Guhathakurta, P., Phillips, A. C., Szkody, P., Prosser, C., Ho, L. C., McMahan, R., Baggley, G., Cheng, K.-P., Havlen, R., Wakamatsu, K., Janes, K., Malkan, M., Baganoff, F., Seitzer, P., Shara, M., Sturch, C., Hesser, J., Hartig, A. N. P., Hughes, J., Welch, D., Williams, T. B., Ferguson, H., Francis, P. J., French, L., Bolte, M., Roth, J., Odewahn, S., Howell, S., & Krzeminski, W. 1996, AJ, 112, 2408

Hillebrandt, W., Kromer, M., Röpke, F. K., & Ruiter, A. J. 2013, ArXiv e-prints

Hillebrandt, W. & Niemeyer, J. C. 2000, ARA&A, 5253, 191

Hobson, M. P., Efstathiou, G. P., & Lasenby, A. N. 2006, General Relativity (Cambridge University Press, New York)

Hogg, D. W., Baldry, I. K., Blanton, M. R., & Eisenstein, D. J. 2002, ArXiv Astrophysics e-prints

Hu, E. M., Cowie, L. L., McMahon, R. G., Capak, P., Iwamuro, F., Kneib, J.-P., Maihara, T., & Motohara, K. 2002, ApJ, 568, L75

Humphreys, R. M. & Davidson, K. 1994, PASP, 106, 1025

Iben, Jr., I. & Tutukov, A. V. 1984, ApJS, 54, 335

Janka, H., Langanke, K., Marek, a., Martinezpinedo, G., & Muller, B. 2007, Physics Reports, 442, 38

Kaiser, N., Wilson, G., Luppino, G., Kofman, L., Gioia, I., Metzger, M., & Dahle, H. 1998, ArXiv Astrophysics e-prints

Kelly, P. L. & Kirshner, R. P. 2012, ApJ, 759, 107

Kessler, R., Becker, A. C., Cinabro, D., Vanderplas, J., Frieman, J. a., Marriner, J., Davis, T. M., Dilday, B., Holtzman, J., Jha, S. W., Lampeitl, H., Sako, M., Smith, M., Zheng, C., Nichol, R. C., Bassett, B., Bender, R., Depoy, D. L., Doi, M., Elson, E., Filippenko, A. V., Foley, R. J., Garnavich, P. M., Hopp, U., Ihara, Y., Ketzeback, W., Kollatschny, W., Konishi, K., Marshall, J. L., McMillan, R. J., Miknaitis, G., Morokuma, T., Mörtsell, E., Pan, K., Prieto, J. L., Richmond, M. W., Riess, A. G., Romani, R., Schneider, D. P., Sollerman, J., Takanashi, N., Tokita, K., van der Heyden, K., Wheeler, J. C., Yasuda, N., & York, D. 2009, ApJS, 185, 32

Kiewe, M., Gal-Yam, A., Arcavi, I., Leonard, D. C., Emilio Enriquez, J., Bradley Cenko, S., Fox, D. B., Moon, D.-S., Sand, D. J., & Soderberg, A. M. 2012, The Astrophysical Journal, 744, 10

Kim, A., Goobar, A., & Perlmutter, S. 1996, PASP, 108, 190

Kim, A. G. 2011, PASP, 123, 230

Komatsu, E., Smith, K. M., Dunkley, J., Bennett, C. L., Gold, B., Hinshaw, G., Jarosik, N., Larson, D., Nolta, M. R., Page, L., Spergel, D. N., Halpern, M., Hill, R. S., Kogut, A., Limon, M., Meyer, S. S., Odegard, N., Tucker, G. S., Weiland, J. L., Wollack, E., & Wright, E. L. 2011, ApJS, 192, 18

Lah, P., Pracy, M. B., Chengalur, J. N., Briggs, F. H., Colless, M., de Propris, R., Ferris, S., Schmidt, B. P., & Tucker, B. E. 2009, MNRAS, 399, 1447

Lederer, C. M., Hollander, J. M., & Perlman, I. 1967, Table of isotopes

Lewis, A. D., Ellingson, E., & Stocke, J. T. 2002, ApJ, 566, 771

Li, W., Filippenko, A. V., Chornock, R., Berger, E., Berlind, P., Calkins, M. L., Challis, P., Fassnacht, C., Jha, S., Kirshner, R. P., Matheson, T., Sargent, W. L. W., Simcoe, R. A., Smith, G. H., & Squires, G. 2003b, PASP, 115, 453

Li, W., Leaman, J., Chornock, R., Filippenko, A. V., Poznanski, D., Ganeshalingam, M., Wang, X., Modjaz, M., Jha, S., Foley, R. J., & Smith, N. 2011b, MNRAS, 412, 1441

Loewenstein, M. 2006, ApJ, 648, 230

Luppino, G. A., Gioia, I. M., Hammer, F., Le Fèvre, O., & Annis, J. A. 1999, A&AS, 136, 117

Madau, P., della Valle, M., & Panagia, N. 1998, MNRAS, 297, L17

Maguire, K., Jerkstrand, a., Smartt, S. J., Fransson, C., Pastorello, a., Benetti, S., Valenti, S., Bufano, F., & Leloudas, G. 2012, MNRAS, 420, 3451

Mannucci, F., Della Valle, M., Panagia, N., Cappellaro, E., Cresci, G., Maiolino, R., Petrosian, A., & Turatto, M. 2005, A&A, 433, 807

Mannucci, F., Maoz, D., Sharon, K., Botticella, M. T., Della Valle, M., Gal-Yam, A., & Panagia, N. 2008, MNRAS, 383, 1121

Maoz, D. & Gal-Yam, A. 2004, MNRAS, 347, 951

Maoz, D. & Mannucci, F. 2012, PASA, 29, 447

Maoz, D., Sharon, K., & Gal-Yam, A. 2010, ApJ, 722, 1879

March, M. C., Trotta, R., Berkes, P., Starkman, G. D., & Vaudrevange, P. M. 2011, Monthly Notices of the Royal Astronomical Society, 418, 2308

Massey, P., Armandroff, T., Veny, J. D., Claver, C., Harmer, C., Jacoby, G., Schoening, B., & Silva, D. 2002, Direct Imaging Manual for Kitt Peak

Mazzali, P. A., Kawabata, K. S., Maeda, K., Foley, R. J., Nomoto, K., Deng, J., Suzuki, T., Iye, M., Kashikawa, N., Ohyama, Y., Filippenko, A. V., Qiu, Y., & Wei, J. 2007, ApJ, 670, 592

Mazzali, P. A., Lucy, L. B., Danziger, I. J., Gouiffes, C., Cappellaro, E., & Turatto, M. 1993, A&A, 269, 423

Mennekens, N., Vanbeveren, D., De Greve, J. P., & De Donder, E. 2010, Astronomy and Astrophysics, 515, A89

Moran, S. M., Ellis, R. S., Treu, T., Smith, G. P., Rich, R. M., & Smail, I. 2007, ApJ, 671, 1503

Oemler, Jr., A. & Tinsley, B. M. 1979, AJ, 84, 985

Pastorello, A., Kasliwal, M. M., Crockett, R. M., Valenti, S., Arbour, R., Itagaki, K., Kaspi, S., Gal-Yam, A., Smartt, S. J., Griffith, R., Maguire, K., Ofek, E. O., Seymour, N., Stern, D., & Wiethoff, W. 2008, MNRAS, 389, 955

Pastorello, A., Turatto, M., Benetti, S., Cappellaro, E., Danziger, I. J., Mazzali, P. A., Patat, F., Filippenko, A. V., Schlegel, D. J., & Matheson, T. 2002, MNRAS, 333, 27

Perlmutter, S. 2003, Physics Today, 56, 040000

Perlmutter, S., Aldering, G., Goldhaber, G., Knop, R. A., Nugent, P., Castro, P. G., Deustua, S., Fabbro, S., Goobar, A., Groom, D. E., Hook, I. M., Kim, A. G., Kim, M. Y., Lee, J. C., Nunes, N. J., Pain, R., Pennypacker, C. R., Quimby, R., Lidman, C., Ellis, R. S., Irwin, M., McMahon, R. G., Ruiz-Lapuente, P., Walton, N., Schaefer, B., Boyle, B. J., Filippenko, A. V., Matheson, T., Fruchter, A. S., Panagia, N., Newberg, H. J. M., Couch, W. J., & Supernova Cosmology Project. 1999, ApJ, 517, 565

Perrett, K., Balam, D., Sullivan, M., Pritchet, C., Conley, a., Carlberg, R., Astier, P., Balland, C., Basa, S., Fouchez, D., Guy, J., Hardin, D., Hook, I. M., Howell, D. a., Pain, R., & Regnault, N. 2010, The Astronomical Journal, 140, 518

Phillips, M. M. 1993, ApJ, 413, L105

Phillips, M. M., Lira, P., Suntzeff, N. B., Schommer, R. a., Hamuy, M., & Maza, J. 1999, The Astronomical Journal, 118, 1766

Postman, M., Lubin, L. M., & Oke, J. B. 2001, The Astronomical Journal, 122, 1125

Poznanski, D., Maoz, D., Yasuda, N., Foley, R. J., Doi, M., Filippenko, A. V., Fukugita, M., Gal-Yam, A., Jannuzi, B. T., Morokuma, T., Oda, T., Schweiker, H., Sharon, K., Silverman, J. M., & Totani, T. 2007, MNRAS, 382, 1169

Richard, J., Kneib, J.-P., Limousin, M., Edge, a., & Jullo, E. 2010, Monthly Notices of the Royal Astronomical Society: Letters, 402, L44

Riess, A. G., Filippenko, A. V., Challis, P., Clocchiatti, A., Diercks, A., Garnavich, P. M., Gilliland, R. L., Hogan, C. J., Jha, S., Kirshner, R. P., Leibundgut, B., Phillips, M. M., Reiss, D., Schmidt, B. P., Schommer, R. A., Smith, R. C., Spyromilio, J., Stubbs, C., Suntzeff, N. B., & Tonry, J. 1998, AJ, 116, 1009

Ruiter, A. J., Belczynski, K., & Fryer, C. 2009, The Astrophysical Journal, 699, 2026

Salpeter, E. E. 1955, ApJ, 121, 161

Sand, D. J., Graham, M. L., Bildfell, C., Zaritsky, D., Pritchet, C., Hoekstra, H., Just, D. W., Herbert-Fort, S., Sivanandam, S., Foley, R. J., & Mahdavi, A. 2012, The Astrophysical Journal, 746, 163

Sand, D. J., Zaritsky, D., Herbert-Fort, S., Sivanandam, S., & Clowe, D. 2008, ApJ, 135, 1917

Scannapieco, E. & Bildsten, L. 2005, ApJ, 629, L85

Schlegel, E. M. 1990, MNRAS, 244, 269

Schneider, P. 2006, Extragalactic Astronomy and Cosmology (Springer Berlin Heidelberg New York)

Schutz, B. 2009, A First Course in General Relativity (Cambridge University Press)

Sharon, K., Gal-Yam, A., Maoz, D., Filippenko, A. V., Foley, R. J., Silverman, J. M., Ebeling, H., Ma, C.-J., Ofek, E. O., Kneib, J.-P., Donahue, M., Ellis, R. S., Freedman, W. L., Kirshner, R. P., Mulchaey, J. S., Sarajedini, V. L., & Voit, G. M. 2010, The Astrophysical Journal, 718, 876

Sharon, K., Maoz, D., Filippenko, A. V., & Al, S. E. T. 2007, ApJ, 660, 1165

Smail, I. A. N., Dressler, A., Couch, W. J., Ellis, R. S., Oemler, A., Butcher, H., & Sharples, R. A. Y. M. 1997, ApJS, 110, 213

Smartt, S. J., Eldridge, J. J., Crockett, R. M., & Maund, J. R. 2009, MNRAS, 395, 1409

Smith, N., Chornock, R., Li, W., Ganeshalingam, M., Silverman, J. M., Foley, R. J., Filippenko, A. V., & Barth, A. J. 2008, The Astrophysical Journal, 686, 467

Sparke, L. S. & Gallagher, III, J. S. 2007, Galaxies in the Universe: An Introduction (Cambridge University Press)

Sullivan, M., Le Borgne, D., Pritchet, C. J., Hodsman, A., Neill, J. D., Howell, D. A., Carlberg, R. G., Astier, P., Aubourg, E., Balam, D., Basa, S., Conley, A., Fabbro, S., Fouchez, D., Guy, J., Hook, I., Pain, R., Palanque-Delabrouille, N., Perrett, K., Regnault, N., Rich, J., Taillet, R., Baumont, S., Bronder, J., Ellis, R. S., Filiol, M., Lusset, V., Perlmutter, S., Ripoche, P., & Tao, C. 2006b, ApJ, 648, 868

Suzuki, N., Rubin, D., Lidman, C., Aldering, G., Amanullah, R., Barbary, K., Barrientos, L. F., Botyanszki, J., Brodwin, M., Connolly, N., Dawson, K. S., Dey, A., Doi, M., Donahue, M., Deustua, S., Eisenhardt, P., Ellingson, E., Faccioli, L., Fadeyev, V., Fakhouri, H. K., Fruchter, A. S., Gilbank, D. G., Gladders, M. D., Goldhaber, G., Gonzalez, A. H., Goobar, A., Gude, A., Hattori, T., Hoekstra, H., Hsiao, E., Huang, X., Ihara, Y., Jee, M. J., Johnston, D., Kashikawa, N., Koester, B., Konishi, K., Kowalski, M., Linder, E. V., Lubin, L., Melbourne, J., Meyers, J., Morokuma, T., Munshi, F., Mullis, C., Oda, T., Panagia, N., Perlmutter, S., Postman, M., Pritchard, T., Rhodes, J., Ripoche, P., Rosati, P., Schlegel, D. J., Spadafora, A., Stanford, S. A., Stanishev, V., Stern, D., Strovink, M., Takanashi, N., Tokita, K., Wagner, M., Wang, L., Yasuda, N., Yee, H. K. C., & Supernova Cosmology Project, T. 2012, ApJ, 746, 85

van Dokkum, P. G., Franx, M., Fabricant, D., Illingworth, G. D., & Kelson, D. D. 2000, ApJ, 541, 95

van Dokkum, P. G., Franx, M., Fabricant, D., Kelson, D. D., & Illingworth, G. D. 1999, ApJ, 520, L95

Vaughan, T. E., Branch, D., Miller, D. L., & Perlmutter, S. 1995, ApJ, 439, 558

Worrall, D. M. & Birkinshaw, M. 2003, MNRAS, 340, 1261

Yungelson, L. R. & Livio, M. 2000, ApJ, 528, 108

Appendix A

Statistical Error Analysis

We discuss in this section the equations used to derive the upper and lower limits (error bars) of quantities that enter the equation for determining the SN Ia rates for our cluster sample.

A.1 Error on SNu, δSNu

From (4.3), The error on SNu is given by

$$\delta SNu = SNu\sqrt{\left(\frac{\delta N}{N}\right)^2 + \left(\frac{\delta L_{tot}}{L_{tot}}\right)^2}. \tag{A.1}$$

We have neglected inclusion of the error on the survey's detection efficiency ϵ and its duration in years δT, as their contribution to the overall error is very minimal and therefore negligible. We discuss the derivation of δN and δL_{tot} .

A.1.1 Derivation of the error on N

We use the guidelines by Gehrels (1986) (hereafter GH86) to derive the confidence limits on our value for N. As described in Chapter four, the number of supernovae N discovered for both MS0451 and CL0303 are given as $N = 1 \times 5/14$ and for the rest of the clusters, $N = 0$. We derive confidence limits on the two factors for $N = 1 \times 5/14$, i.e. $N_1 = 1$ and $N_2 = 5/14$. Determining confidence limits for small number counts make use of Poisson and Binomial statistics, with the latter being more suitable for counts that involve ratios of indistinguishable random events, including supernova type ratios (GH86). We thus perform Poisson statistics on N_1 and Binomial statistics on N_2 to derive confidence limits on the two factors, and then compute their combined uncertainty.

A.1.1.1 Derivation of confidence limits for N_1

Following the same approach as GH86, (A.2) and (A.3)

$$\sum_{x=0}^{N_1} \frac{\lambda_u^x e^{-\lambda_u}}{x!} = 1 - CL, \tag{A.2}$$

$$\sum_{x=0}^{N_1-1} \frac{\lambda_l^x e^{-\lambda_l}}{x!} = CL, \tag{A.3}$$

define the Poissonian upper and lower limits λ_u and λ_l respectively, of confidence level (single-sided) CL. As there are no analytical solutions to (A.1) and (A.2), λ_u and λ_l are approximated to desired accuracies from the given values of N_1 and CL, using numerical techniques such as "Newton's Method". Skipping the algebraic derivational steps presented in GH86, the approximate relations for upper limits λ_u on N_1 derived from (A.2) and (A.3) are given in (A.4), (A.5) and (A.6) as

$$\lambda_u \approx N_1 + S\sqrt{N_1 + \frac{3}{4} + \frac{S^2+3}{4}}, \tag{A.4}$$

$$\lambda_u \approx (N_1+1)\left[1 - \frac{1}{9(N_1+1)} + \frac{S}{3\sqrt{N_1+1}}\right], \tag{A.5}$$

$$\lambda_u \approx N_1 + S\sqrt{N_1+1} + \frac{S^2+2}{3}, \tag{A.6}$$

where S is the number of Gaussian σ corresponding to a chosen CL. Similarly, (A.7) - (A.10) provide approximate relations for the lower limits on N_1:

$$\lambda_l \approx N_1 - S\sqrt{N_1 - \frac{1}{4}} + \frac{S^2-1}{4}, \tag{A.7}$$

$$\lambda_l \approx N_1\left(1 - \frac{1}{9N_1} - \frac{S}{3\sqrt{N_1}}\right)^3, \tag{A.8}$$

$$\lambda_l \approx N_1 - S\sqrt{N_1} + \frac{S^2-1}{3}, \tag{A.9}$$

$$\lambda_l \approx N_1\left(1 - \frac{1}{9N_1} - \frac{S}{3\sqrt{N_1}} + \beta N_1^{\gamma}\right)^3, \tag{A.10}$$

where S is as defined before and β and γ are free parameters defined as $0.0 \leq \beta \leq 0.278$ and $-4.00 \leq \gamma \leq -1.80$ and are adjusted for each confidence level (see Table 3 of GH86).

For the special case of $S = 1$ which yields 1σ errors that we are interested in at confidence level $CL = 0.8413$, GH86 recommends the use of (A.5) and (A.10) with $\beta = 0$ (which reduces to (A.8)), to determine λ_u and λ_l. For our case of $N_1 = 1$, we find that both (A.5) and (A.10) indeed yield the closest approximations for λ_u and λ_l to the exact values given in GH86's Tables 1 and 2, than the other approximate relations. We thus make use of these two equations to approximate the confidence limits on $N_1 = 1$.

A.1.1.2 Derivation of confidence limits for N_2

As stated above, we use Binomial statistics to determine confidence limits for $N_2 = 5/14$. To make the derivational steps easier to follow, we denote the number of SNe Ia and non-SN Ia events by N_{ia} and N_{nia} respectively, i.e. $N_2 = N_{ia}/(N_{ia} + N_{nia})$. The counting of N_{ia} and N_{nia} events both obey Poisson statistics and following GH86's explanation for obtaining confidence limits on the ratio, if observations of N_{ia} and N_{nia} events are distributed with true rates of λ_{ia} and λ_{nia} respectively, the joint probability $f(N_{ia}, N_{nia})$ of observing both events is

$$\begin{aligned} f(N_{ia}, N_{nia}) &= \frac{\lambda_{ia}^{N_{ia}} e^{-\lambda_{ia}}}{N_{ia}!} \frac{\lambda_{ia}^{N_{nia}} e^{-\lambda_{nia}}}{N_{nia}!} \\ &= \frac{(\lambda_{ia} + \lambda_{nia})^{N_{ia}+N_{nia}} e^{-(\lambda_{ia}+\lambda_{nia})}}{N_{ia} + N_{nia}} \binom{N_{ia} + N_{nia}}{N_{ia}} N_{ia} P_{ia}^{N_{ia}} (1 - p_{ia})^{N_{nia}}, \end{aligned} \tag{A.11}$$

where $p_{ia} = \lambda_{ia}/(\lambda_{ia}+\lambda_{nia})$ and $\binom{N_{ia}+N_{nia}}{N_{ia}} N_{ia}$ is the binomial coefficient $(N_{ia}+N_{nia})!/N_{ia}!N_{nia}!$. The joint probability (A.11) is the product of Poisson probability for the combined rates and the Binomial probability for obtaining N_{ia} and N_{nia} provided that $N_{ia} + N_{nia}$ represent the combined number of observed events.

Our objective is to determine confidence limits for p_{ia} in (A.11) using Binomial statistics, which defines the upper limit p_{iau} and lower limit p_{ial} by

$$\sum_{x}^{N_{ia}} \binom{N_2}{x} p_{iau}^{x} (1 - p_{iau})^{n-x} = 1 - CL, \qquad (N_{ia} \neq N_{nia}) \tag{A.12}$$

$$\sum_{x}^{N_{ia-1}} \binom{N_2}{x} p_{iau}^{x} (1 - p_{ial})^{n-x} = CL, \qquad (N_{ia} \neq 0) \tag{A.13}$$

where N_2 and CL are as defined above. For the special cases $N_{nia} = 0$ ($N_{ia} = N_2$), $p_{iau} = 1.0$ and for $N_{ia} = 0$, $p_{iau} = 0.0$.

Analytical expressions for p_{iau} and p_{ial} in (A.12) and (A.13) do not exist in general, as was the case with Poisson limits, except for a few special cases for which general approximate expressions are derived (GH86). Again skipping the intermediate algebraic steps outlined in GH86 as was done with Poisson limits, we obtain from (A.12) and (A.13) a general approximate expression for p_{iau},

$$p_{iau} = \frac{(N_{ia} + 1)e^{2w} + \epsilon N_{nia}}{(N_{ia} + 1)e^{2w} + N_{nia}}, \tag{A.14}$$

where

$$w = \frac{S(h+\lambda)^{1/2}}{h} + \left(\frac{1}{2N_{nia}-1} - \frac{1}{2N_{ia}+1}\right)(\lambda + \tfrac{5}{6} - \tfrac{2}{3h}),$$

$$h = 2\left(\frac{1}{2N_{nia}-1} + \frac{1}{2N_{ia}+1}\right)^{-1},$$

$$\lambda = \frac{S^2-3}{6},$$

with S as defined for Poisson limits and

$$\epsilon = 0.64(1-S)e^{-N_{nia}}.$$

p_{iau} and p_{ial} are related via,

$$p_{ial} = 1 - p_{niau}, \tag{A.15}$$

derived from (A.12) and (A.13), where p_{niau} represent the upper limit for the ratio of non-SN Ia events N_{nia} to the total events, which can be determined from (A.14) by switching the positions of N_{ia} and N_{nia}. We have derived the confidence limits for p_{ia}, shown in Table A.1, for the case $S = 1$, using (A.14) and (A.15).

Table A.1. also shows our derived confidence limits $N_1 = 1$ and $N_2 = 5/14$, using equations (A.5) and (A.10) for Poissonian, and (A.14) and (A.15) for Binomial confidence limits.

Table A.1: Confidence limits derived for the values of N_1 and N_2, using Poissonian and Binomial statistics respectively for our cluster sample.

		Derived Poisson confidence limits		Derived Binomial confidence limits	
Cluster	N_1/N_2	λ_u	λ_l	p_{iau}	p_{ial}
MS0451	1	3.287	0.171	-	-
CL0303	1	3.287	0.171	-	-
MS0451	5/14	-	- 1	0.526	0.193
CL0303	5/14	-	- 1	0.526	0.193

The determined Poisson and Binomial confidence limits for MS0451 and CL0303 are combined using

$$\delta N = N\sqrt{\left(\frac{\delta N_1}{N_1}\right)^2 + \left(\frac{\delta N_2}{N_2}\right)^2}, \tag{A.16}$$

to obtain the error bars shown in Table 4.4 on the combined value of $N = N_1 \times N_2 = 0.36$ for each cluster.

A.1.1.3 Derivation of confidence limits for $N = 0$

Derivation of the confidence limits for $N = 0$ is similar to that for N (or N_1) $= 1$. Substituting N_1 for $N = 0$ in (A.7) - (A.10) again for the case of $S = 1$, we get a lower limit of $\lambda_l = 0.0$. For the upper limit, we still make use of (A.5) than the other two approximations, for the same reason given for the case of $N = N_1 = 1$ and obtain $\lambda_u = 1.826$ for all of our clusters with $N = 0$.

A.1.2 Derivation of the error on L_{tot}

From (4.5), the uncertainty on total luminosity L_{tot} within the cluster search area is, from propagation of uncertainties, given by

$$\delta L_{tot} = L_{tot}\sqrt{\left(\frac{\delta\phi_*}{\phi_*}\right)^2 + \left(\frac{\delta L_*}{L_*}\right)^2 + \left(\frac{\delta\Gamma(\alpha+2)}{\Gamma(\alpha+2)}\right)^2}. \tag{A.17}$$

We derive the formulae used in determining the error bars given in Table 4.4 for ϕ_*, L_* and $\Gamma(\alpha+2)$ using the methods of propagation of uncertainties.

A.1.2.1 Derivation of $\delta\phi_*$

From (4.8), $\phi_* = V_{\delta r} \times \phi_{\phi,old}/V_{1Mpc}$ which from propagation of uncertainties, yields

$$\delta\phi_* = \phi_*\sqrt{\left(\frac{\delta V_{\Delta r}}{V_{\Delta r}}\right)^2 + \left(\frac{\delta\phi_{*,old}}{\phi_{*,old}}\right)^2} = \phi_*\frac{\delta\phi_{*,old}}{\phi_{*,old}}, \tag{A.18}$$

since $V_{\Delta r}$ is error-free.

A.1.2.2 Derivation of δL_*

From (4.6), we have

$$L_{*,B} = 10^{\left(\frac{M_{\odot,B}-M_{*,B}}{2.5}\right)}L_{\odot,B}. \tag{A.19}$$

Taking the natural logarithm and derivative with respect to (w.r.t.) $M_{*,B}$ of each side and applying the chain rule on the LHS, we have $dL_{*,B}/dM_{*,B} = -(\ln 10/2.5)L_{*,B}$. From propagation of uncertainties, we get

$$\delta L_* = \left|\frac{dL_{*,B}}{dM_{*,B}}\right|\delta M_{*,B} = \left|-\frac{\ln 10}{2.5}10^{\left(\frac{M_{\odot,B}-M_{*,B}}{2.5}\right)}\right|\delta L_{*,B}. \tag{A.20}$$

A.1.2.3 Derivation of $\delta\Gamma(\alpha+2)$

From propagation of uncertainties, the uncertainty on the gamma function $\Gamma(\alpha+2)$, a function of α is given by

$$\delta\Gamma(\alpha+2) = \left|\frac{\delta\Gamma(\alpha+2)}{d\alpha}\right|\delta\alpha. \tag{A.21}$$

The derivative of $\Gamma(\alpha+2)$ w.r.t α is

$$\begin{aligned}\frac{\delta\Gamma(\alpha+2)}{d\alpha} &= (\alpha+2)\psi^0(\alpha+2)\\ &= \Gamma(\alpha+2)\psi((\alpha+1)+1)\\ &= \Gamma(\alpha+2)\psi(x+1)\end{aligned} \tag{A.22}$$

where $x = \alpha+1$,

and ψ is the digamma function defined as $\psi(x) = \psi^0 = \Gamma'(x)/\Gamma(x)$, with

$$\psi(1+x) = \psi(x) + \tfrac{1}{x},$$

and $\psi(x)$ can be approximated by

$$\psi(x) = \ln x - \tfrac{1}{2x} - \tfrac{1}{2x^2} + \tfrac{1}{120x^4} + O(\tfrac{1}{x^8}) \qquad (x \to \infty)$$

(see Bernardo 1976). Substitution into (A.21) gives

$$\delta\Gamma(\alpha+2) = \left|\Gamma(\alpha+2)\left(\psi(x) + \frac{1}{x}\right)\right| \delta\alpha. \tag{A.23}$$

The determined uncertainties for ϕ_*, $L_{*,B}$ and $\Gamma(\alpha+2)$ from (A.18), (A.20) and (A.23) respectively are substituted into (A.17) along with the values of ϕ_*, $L_{*,B}$ and $\Gamma(\alpha+2)$ given in Table 4.4 to obtain the error bars for L_{tot} shown in Table 4.4 for each cluster.

Finally, substitution of δN and δL_{tot} determined for each cluster into (A.1) with their respective values for N and L_{tot} (which in this case will be for clusters with $N \neq 0$) yields the quoted error bars on the determined SN Ia rates given in Table 4.8 for MS0451-03 and CL0303+17.

The upper limits shown on the zero SN Ia rates for CL0016 and A370 were obtained by substituting for N in (4.3) the product of the upper limit on $N = 0$ and the ratio of SNe Ia to non SNe Ia, i.e. $1.83 \times 5/14$, with the values for L_{tot}, ϵ and T given in Table 4.8 for each cluster.